

# **SANDIA REPORT**

SAND2003-8124

Unlimited Release

Printed March 2003

## **Control Strategies for Homogeneous Charge Compression Ignition Engines: LDRD Final Report**

Jacqueline H. Chen, John C. Hewson, Alan R. Kerstein,  
Christopher A. Kennedy, Tarek Echehki, and Joseph C. Oefelein

Prepared by  
Sandia National Laboratories  
Albuquerque, New Mexico 87185 and Livermore, California 94550

Sandia is a multiprogram laboratory operated by Sandia Corporation,  
a Lockheed Martin Company, for the United States Department of Energy's  
National Nuclear Security Administration under Contract DE-AC04-94AL85000.

Approved for public release; further dissemination unlimited.



**Sandia National Laboratories**

Issued by Sandia National Laboratories, operated for the United States Department of Energy by Sandia Corporation.

**NOTICE:** This report was prepared as an account of work sponsored by an agency of the United States Government. Neither the United States Government, nor any agency thereof, nor any of their employees, nor any of their contractors, subcontractors, or their employees, make any warranty, express or implied, or assume any legal liability or responsibility for the accuracy, completeness, or usefulness of any information, apparatus, product, or process disclosed, or represent that its use would not infringe privately owned rights. Reference herein to any specific commercial product, process, or service by trade name, trademark, manufacturer, or otherwise, does not necessarily constitute or imply its endorsement, recommendation, or favoring by the United States Government, any agency thereof, or any of their contractors or subcontractors. The views and opinions expressed herein do not necessarily state or reflect those of the United States Government, any agency thereof, or any of their contractors.

Printed in the United States of America. This report has been reproduced directly from the best available copy.

Available to DOE and DOE contractors from  
U.S. Department of Energy  
Office of Scientific and Technical Information  
P.O. Box 62  
Oak Ridge, TN 37831

Telephone: (865)576-8401  
Facsimile: (865)576-5728  
E-Mail: [reports@adonis.osti.gov](mailto:reports@adonis.osti.gov)  
Online ordering: <http://www.doe.gov/bridge>

Available to the public from  
U.S. Department of Commerce  
National Technical Information Service  
5285 Port Royal Rd  
Springfield, VA 22161

Telephone: (800)553-6847  
Facsimile: (703)605-6900  
E-Mail: [orders@ntis.fedworld.gov](mailto:orders@ntis.fedworld.gov)  
Online order: <http://www.ntis.gov/help/ordermethods.asp?loc=7-4-0#online>





SAND-8124  
Unlimited Release  
Printed March 2003

## **Control Strategies for Homogeneous Charge Compression Ignition Engines: LDRD Final Report**

Jacqueline H. Chen, John C. Hewson, Alan R. Kerstein,  
Christopher A. Kennedy, Tarek Echekki, and Joseph C. Oefelein  
Combustion Research Facility  
Reacting Flow Research Department  
Sandia National Laboratories  
Livermore, California 94551-0969

### **Abstract**

Homogeneous charge compression ignition engines (HCCI) operate on the principle of compressing a dilute premixed charge until it autoignites and burns volumetrically. However, achieving appropriate combustion across the load-speed map of the engine and slowing the combustion to achieve a smooth heat release time history – so as to prevent engine damage – remains a formidable challenge. Recent zero-dimensional computational studies have shown that it is difficult to achieve a smooth heat release history with a fully homogeneous mixture. A key technical challenge, then, is how to actively control the in-cylinder fuel/air/exhaust gas residual mixture composition and temperature space/time history to obtain the desired heat release time profile across the operating conditions of the engine. This LDRD final report documents the development of an integrated computational capability for HCCI combustion. The capability is comprised of a novel one-dimensional turbulence modeling (ODT) approach extended to include detailed chemistry during an engine cycle, direct numerical simulation to examine the different modes of autoignitive propagation and the influence of turbulent mixing on ignition delay, and an LES effort to relate the ignition timing and burn rate parameterizations to actual mixture preparation strategies for engine geometries. These capabilities are used to study the effect of mixture inhomogeneities for HCCI conditions on ignition timing and the rate of heat release.

**Intentionally Left Blank**

## Contents

Abstract .....	3
Contents.....	5
Introduction .....	7
1. Towards Control of HCCI Combustion: Neglecting Inhomogeneities.....	8
1.1 Control of the Ignition Timing.....	8
1.2 Ignition Timing as a Function of Operating Condition.....	9
1.3 Ignitability of Mixtures .....	13
1.4 An Engine Control Algorithm.....	16
1.5 Summary .....	16
2. An Integrated Computational Method to Study the Effect of Inhomogeneities in HCCI Combustion.....	18
2.1 One-Dimensional Turbulence Model for Engines .....	21
2.1.1 One-dimensional Turbulence Model.....	21
2.1.2 Evolution of the Mixture Composition .....	23
2.1.3 Mixing Effects on Ignition Behavior .....	24
2.1.4 Relating Ignition Times to Ignitability.....	26
2.1.5 Inhomogeneities and the Rate of Heat Release.....	28
2.1.6 On the Merits of the ODT-based Model for Studying HCCI Combustion .....	29
2.1.7 Summary .....	30
2.2 Direct Numerical Simulation of Autoignitive Propagation Modes.....	34
2.2.1 Introduction .....	34
2.2.2 Computational Method and Configuration .....	34
2.2.3 Results and Discussion.....	35
2.2.4 Analysis.....	39
2.2.5 Conclusions .....	42
2.3 Large-Eddy Simulation .....	44
2.3.1 Introduction .....	44
2.3.2 Theoretical--Numerical Framework.....	45
2.3.3 Computational Domain .....	49
2.3.4 Results and Discussion.....	51
2.3.5 Summary .....	58
Appendix: Additive Runge-Kutta Method for Stiff Chemistry Integration.....	62
A.1 Introduction .....	62
A.2 N-Additive Runge-Kutta Methods .....	65
A.3 Implicit-Explicit ARK <sub>2</sub> Methods.....	70
A.4 Implementation.....	74
A.5 Conclusions .....	76



**Intentionally Left Blank**

## Introduction

Homogeneous charge compression ignition engines (HCCI) operate on the principle of compressing a dilute premixed charge until it autoignites and burns volumetrically. This is a relatively new realm of combustion, wherein the mixture is sufficiently dilute so as to prevent flame propagation – hence, combustion occurs volumetrically. By operating under overall fuel-lean conditions, and therefore at lower temperatures, HCCI can attain high engine efficiencies comparable to diesel engines without producing  $\text{NO}_x$  and soot. For appropriate mixture and fuel type, engines have been successfully operated in a HCCI mode. However, achieving appropriate combustion across the load-speed map of the engine and slowing the combustion to achieve a smooth heat release time history – so as to prevent engine damage – remains a formidable challenge. Recent zero-dimensional computational studies have shown that it is difficult to achieve a smooth heat release history with a fully homogeneous mixture. A key technical challenge, then, is how to actively control the in-cylinder fuel/air/exhaust gas residual mixture composition and temperature space/time history to obtain the desired heat release time profile across the operating conditions of the engine.

The primary objective of this LDRD project is to develop a complementary simulation and modeling capability to the Sandia HCCI Engine experiment to: 1) elucidate the role of turbulent mixing coupled with various strategies for mixture preparation on inhomogeneous autoignition; and 2) parameterize ignition delay and burn rate in terms of the thermochemistry and turbulent mixing rates; and 3) from the fundamental knowledge and parameterization, construct mixture preparation control strategies to control the ignition timing, the heat release time history, and unburnt hydrocarbons emissions across the load-speed map of an engine. The present effort at Sandia involves the development of a novel one-dimensional turbulence modeling (ODT) approach extended to include detailed chemistry during an engine cycle, direct numerical simulation to examine the different modes of autoignitive propagation and to study the effects of turbulent mixing on ignition delay, and an LES effort to relate the ignition timing and burn rate parameterizations to actual mixture preparation strategies for engine geometries.

In the first chapter a relationship between various engine operating variables and possible control variables for a homogeneous system is presented, followed by an empirical model developed to predict ignition delays for compression ignition of single-stage fuels. In the second chapter the role of inhomogeneities in temperature and concentration for HCCI conditions is explored using an integrated simulation and modeling approach that couples large-scale and small-scale mixing and ignition kinetics. This integrated approach couples state-of-the-art simulation tools, large-eddy simulation and direct numerical simulation with a novel one-dimensional turbulence model adapted for engine conditions. Finally, a new time-accurate integration method for advancing stiff chemistry associated with ignition of hydrocarbon fuels is presented in the Appendix.

## **1. Towards Control of HCCI Combustion: Neglecting Inhomogeneities**

Homogeneous-charge compression-ignition (HCCI) engines operate by creating a nearly homogeneous mixture of fuel and air within an engine cylinder that is then compression ignited. Compression ignition allows the engine to operate at higher compression ratios than is typical of, for example, spark-ignited engines, and this leads to greater efficiencies. Possible gains in thermodynamic efficiency alone may be on the order of 10-15% for HCCI relative to spark-ignited engines, depending on operating conditions. Furthermore, the ability to combust very dilute mixtures allows the engines to revert to throttle-less operation resulting in efficiency improvement on the order of 20-40% at low loads. Typically, the mixture is lean or diluted in which case the peak combustion temperatures are moderated. One significant source of pollutant emissions is oxides of nitrogen, and reducing the peak combustion temperatures significantly reduces these emissions relative to, for example, diesel engines. By creating a high degree of premixedness of the mixture and keeping it lean, stoichiometric and rich mixtures may be avoided. Avoidance of such mixtures reduces another significant source of oxides of nitrogen and virtually eliminates soot production. The pollutant emissions that are not greatly reduced, unburned hydrocarbons (UHC) and carbon monoxide (CO), can be cleaned up relatively easily using an oxidative catalyst in the (lean) exhaust stream.

It is evident that HCCI, by providing increased efficiency and greatly reduced emissions of hard-to-mitigate pollutants, holds a great deal of promise [1,2]. However, challenges in the control of the ignition timing, the control of the rate of heat release and the control of pollutant emissions have limited the commercialization of this technology. In this and the following sections means of overcoming these obstacles will be investigated.

### **1.1 Control of the Ignition Timing**

One of the challenges that arises with HCCI is the control of the ignition timing. With spark-ignited engines, the spark controls the ignition timing. With diesel engines, the fuel ignites soon after the fuel is injected and the fuel injection timing is used to control the ignition timing. HCCI combustion lacks both of these means of control. For HCCI, the fuel will be injected well before the desired ignition time so that it may mix to a great degree of homogeneity prior to ignition. As the piston compresses the mixture, it is heated and chemical reactions occur, leading towards ignition. Ignition timing is a function of the rate of these chemical reactions and the rate of piston motion. The rate of chemical reactions depend on the thermochemical state with hotter and less-lean mixtures tending to ignite more rapidly. Maximum efficiency is obtained for ignition at the point of greatest compression, referred to as top-dead center or TDC. If the chemical rates are fast relative to the compression rates, then ignition occurs before the mixture is fully compressed, resulting in extra work being required to compress the burned mixture—a loss of efficiency. If the chemical rates are slow relative to compression and the subsequent expansion, then ignition occurs late, or not at all, resulting in lost pressure work. This is illustrated in Fig. 1.1 where temperature-time curves indicate the effect of perturbations in the engine speed, fuel equivalence ratio and uncompressed mixture



temperature. In Fig. 1.1, the dashed red lines indicate an approximately optimal operating condition with the area within the pressure-volume curves maximized. Attainment of a single optimal operating condition within a laboratory setting, while not trivial, is not a great challenge. However, for a practical system, it is necessary for the engine to respond to changes in both prescribed operating conditions and its environment. Examples shown in Fig. 1.1 include (a) the result of an increase in engine speed that leads to later ignition because the ignition kinetics have not responded to change in available time for ignition imposed by the piston motion, (b) the result of a decrease in the fuel load at a fixed speed, the equivalent of letting up on the gas pedal, that reduces the chemical rates leading to later ignition and (c) the result of an increased inlet temperature, which may result from changes in engine or outdoor temperatures, leading to faster chemical rates and earlier ignition. It is clear that one of the great challenges in ignition timing control is the ability to adapt dynamically to changing operating conditions.

For present purposes, it is assumed that the engine needs to respond to changes in speed and/or load (equivalently the mass of fuel injected into the cylinder). As indicated above, changes in engine speed alter the available time for ignition chemistry to occur while changes in the load change the chemical rates. There are a variety of means available to control the ignition timing in HCCI engines, though several of them act by affecting the compressed gas temperature. This technique works because the chemical rates are strongly temperature dependent. One means of affecting the compressed gas temperature is to use cooled exhaust-gas recirculation (EGR). This changes the degree of compression heating because the exhaust gases generally have a smaller ratio of specific heats than unreacted mixture [2]. It might also be possible to mix hot exhaust-gas with fresh charge to exert greater control of the intake charge temperature. However, the transport times involved in flow through intake manifolds is such that the engine takes many cycles to respond to changes in EGR. One other means of affecting the compressed gas temperature is to use variable-valve timing to change the effective compression ratio [3]. In this technique, the valves are left open during a portion of the compression cycle to reduce the degree of compression heating. This technique has potential for acting on cycle-to-cycle time scales. In the present work, the precise means of affecting the compressed gas temperature is left open, though a combination of the above means is assumed. Rather, the compressed gas temperature itself is specified as the control variable. In subsequent sections discussing inhomogeneities, the degree of unmixedness will also be presented as an additional control parameter.

## 1.2 Ignition Timing as a Function of Operating Conditions

Focusing on the combined influence of the engine speed and load with the compressed gas temperature as the control variable, the behavior of the ignition timing is examined in greater detail here. Figures 1.2, 1.3 and 1.4 show contour plots of the ignition timing as a function of these three variables for three different fuels: diluted hydrogen, n-heptane and iso-octane. These three fuels are selected to exhibit the range of ignition behavior that might be found with different engine fuels.

Figures 1.2, 1.3 and 1.4 show the full speed-load-temperature space in three-dimension contour plots along with slices from that space at a fixed speed and a fixed load. If a single variable changes, for example the speed or load, it is evident that an

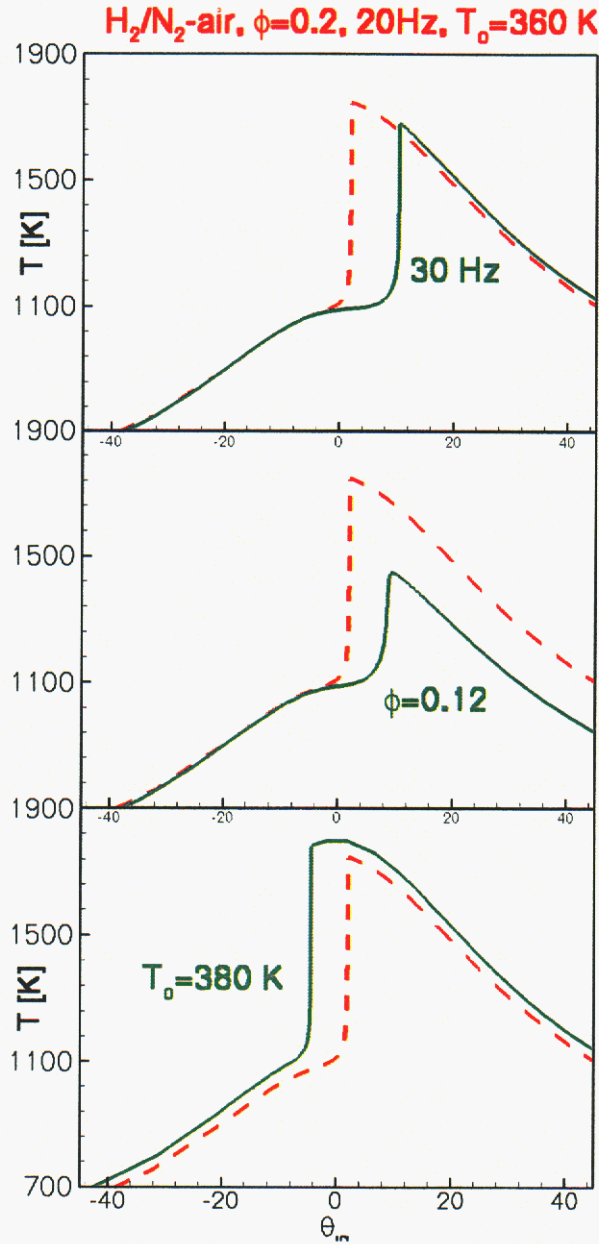


Figure 1.1. Temperature-time histories are shown for an optimal operating condition (red dashed lines) as well as for perturbations to that optimal condition (green solid lines). The insets show the corresponding pressure-specific volume curves indicating the loss of efficiency that occurs when ignition timing is not optimal. All curves are for lean diluted hydrogen mixtures and calculations are performed assuming complete homogeneity and adiabaticity.

HCCI engine with previously timely ignition will change to operating with either early or late ignition, both undesirable. However, it is evidently possible to simultaneously change the compressed mixture temperature and maintain optimal ignition timing over a certain range of loads and speeds. On these figures, white regions indicate conditions

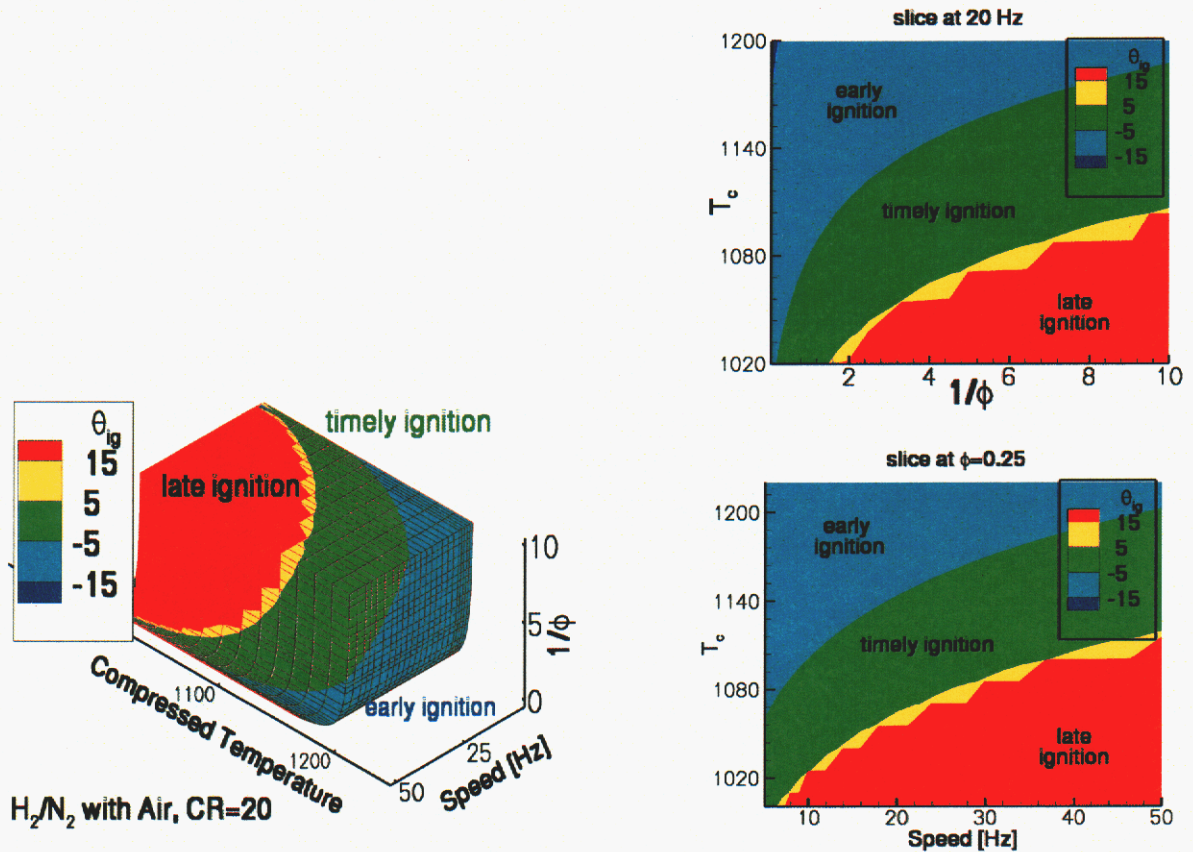


Figure 1.2. Contour plots showing the ignition angle relative to TDC for  $H_2/N_2$  mixtures (50% each by volume in the fuel stream) at a compression ratio of 20. Ignition times are shown as a function of engine speed, fuel-air equivalence ratio ( $\phi$ ) and the compressed gas temperature ( $T_c$ ). Engine speed refers to rev/s.

over which ignition times were not simulated because they corresponded to particularly low or high inlet air temperatures. The fuel-air equivalence ratio ( $\phi$ ) ranges between 0.1 and 10 in the simulations.

Hydrogen, shown in Fig. 1.2, is chemically among the simplest of fuels (see later sections). Ignition times with hydrogen mixtures have a relatively simple Arrhenius temperature dependence and a relatively simple dependence on the mixture composition. Furthermore, as a diatomic gas, hydrogen is not subject to the differential compressive heating effects typically present for hydrocarbons. Differences in the ratio of specific heats between the fuel and air for hydrocarbon fuels can lead to large differences in compressive heating for different stoichiometries. In addition it appears to have the widest possible power range, with reasonable changes in the compressed gas temperature



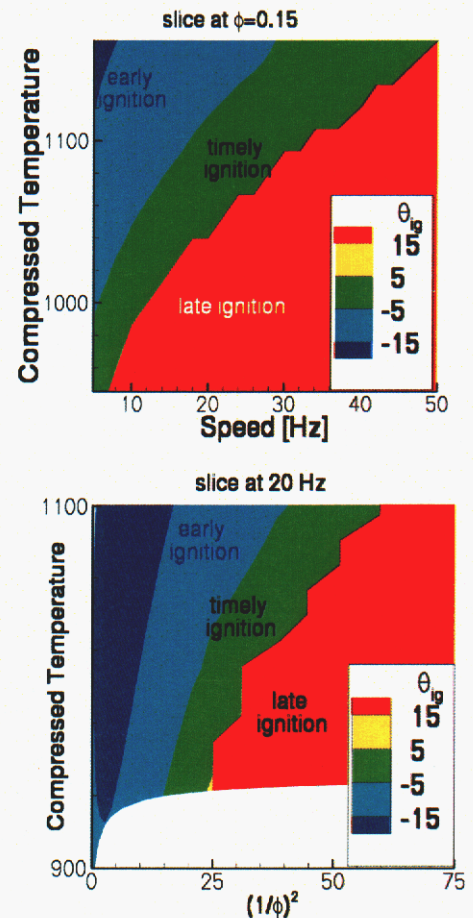
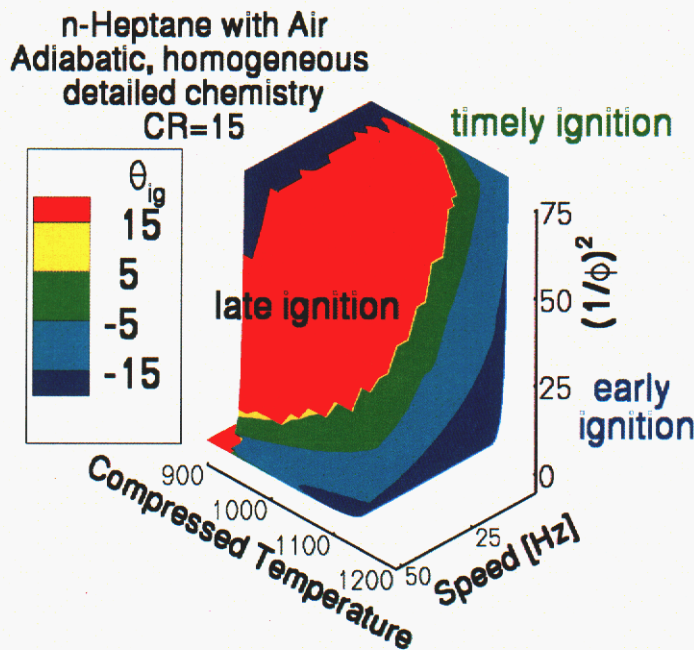


Figure 1.3. Contour plots showing the ignition angle relative to TDC for n-heptane mixtures at a compression ratio of 15. Ignition times are shown as a function of engine speed, the square of the inverse of the fuel-air equivalence ratio ( $\phi$ ) and the compressed gas temperature. Engine speed refers to rev/s.

being able to adapt to changes in both the speed and load of roughly a factor of five, potentially a twenty-five fold change in power.

N-heptane, shown in Fig. 1.3, is a surrogate diesel fuel with significant low-temperature kinetic effects during typical compression ignition. These effects result in ignition at lower temperatures and thus lower compression ratios. The consequence is that n-heptane and diesel type fuels cause the engine to operate at lower efficiency. However, the prevalence of the present diesel fueling infrastructure and other potential advantages require consideration of these fuels, especially since the efficiency penalty is only a few percent. As will be discussed later, because of the low-temperature chemistry a significant fraction of the heptane is consumed during the compression stroke, well before TDC. One consequence of this is a more limited range of operating speeds evident in Fig. 3 when compared with Fig. 1.2. Also of interest is the effect of the fuel-air equivalence ratio ( $\phi$ ) on the compression heating. For less lean mixtures (smaller

( $1/\phi$ ), the degree of compression heating is significantly reduced because the ratio of specific heats for large hydrocarbons approaches unity.

Iso-octane, shown in Fig. 1.4, is a prototypical gasoline fuel, a large hydrocarbon with less low-temperature kinetics over the time scales of interest. However, it was found over the course of this study that the low-temperature kinetics were not negligible and result in the significant changes in ignition timing observed in Fig. 1.4. Specifically, for less lean mixtures (smaller  $1/\phi$ ) where the low-temperature chemistry is faster, the low-temperature kinetics do indeed become significant and result in ignition that is premature for the given compressed gas temperatures. This behavior occurs, however, under conditions that are generally avoided in HCCI combustion because the peak combustion temperatures for  $1/\phi < 2$  would result in excess oxides of nitrogen, one pollutant of concern. The same behavior occurs if the engine speed is reduced sufficiently, so that more time is available for the low-temperature kinetics. This implies that the combination of low speeds and high loads may need to be avoided for HCCI with iso-octane and similar fuels.

Figures 1.2, 1.3 and 1.4 indicate that a control variable like the compressed gas temperature can be used to control the ignition timing over a significant range of operating conditions, responding to changes in both the engine speed and load. The challenge to be addressed in the following section is how an engine controller would determine how the control variable should be changed in response to changes in the engine speed and/or load.

### 1.3 Ignitability of Mixtures

It is desirable to obtain a relationship between the various engine operating variables and the possible control variables. In HCCI, ignition is controlled by the relationship between two rates or two time scales. These two rates are the chemical rates and the rate of compression, and their ratio will be termed the ignitability,  $I$ . Ignition depends on this ratio because it represents the balance between the time available for ignition, given by the time that the mixture is near its most compressed state, and the time required for ignition at that most compressed state. The time required to ignite depends on the thermochemical state—primarily the temperature and the fuel mass fraction.

In order to develop a more explicit expression for the ignitability, a simplified energy equation is considered, with chemistry assumed to be representable by a single effective Arrhenius rate and transport assumed to be negligible

$$\rho c_p \frac{DT}{dt} = \frac{dP}{dt} + \rho q A Y_F^n Y_O^m e^{-E/RT} \quad (1.1)$$

Here  $T$  is the temperature,  $\rho$  the density,  $c_p$  the specific heat at constant pressure,  $P$  the pressure,  $q$  the heat released per mass of fuel burned,  $A$  the frequency factor,  $Y_F$  the fuel mass fraction,  $Y_O$  the oxidizer mass fraction,  $E$  the effective activation energy and  $R$  the ideal gas constant. The derivative on the left hand side of Eq. 1.1 is the substantial derivative, indicating the temperature change of a fluid element that may be convected. The energy equation indicates that changes to a fluid element temperature



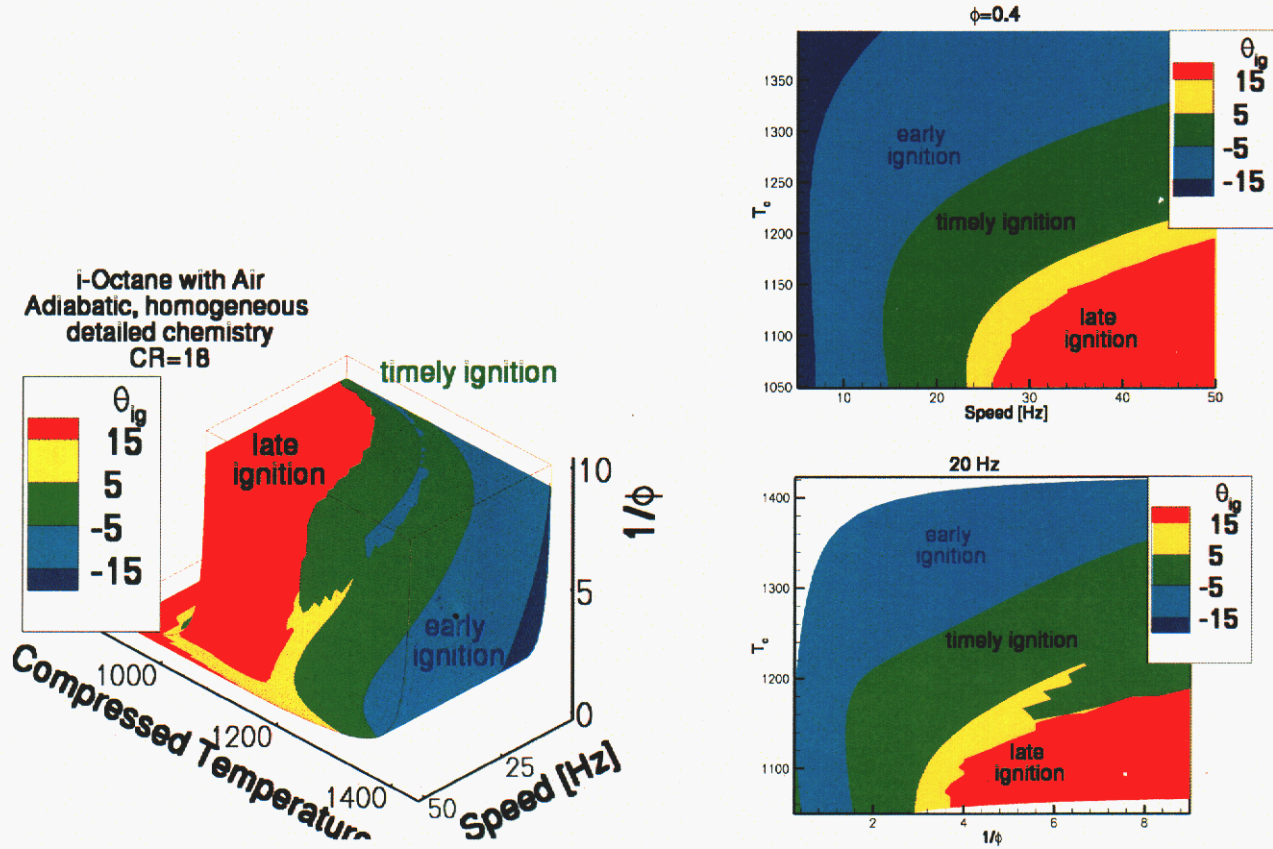


Figure 1.4. Contour plots showing the ignition angle relative to TDC for iso-octane at a compression ratio of 16. Ignition times are shown as a function of engine speed, the fuel-air equivalence ratio ( $\phi$ ) and the compressed gas temperature. Engine speed refers to rev/s.

can result from either compressive heating or chemical reactions. The heating due to compression tends to increase the chemical rates through the Arrhenius temperature dependence of the last terms leading to ignition for the appropriate initial conditions and time scales.

In order to analyze compression ignition, it is useful to work in an entropy-like variable [4]

$$S = T / P^{(\gamma-1)/\gamma}$$

which is the logarithm of the entropy divided by  $c_p$ . To determine ignition times, the large effective activation energy of ignition is utilized to define the small parameter  $\varepsilon = RT_{TDC} / E$ ; here  $T_{TDC}$  is the characteristic temperature at TDC. In the large activation energy limit where  $\varepsilon$  is small, chemical evolution is only significant for a short time period of order  $\tau = (t - t_{TDC}) \omega_{cy} / \varepsilon$  where non-dimensionalized temperature and pressure changes around TDC are of order  $\varepsilon$ . Here,  $t - t_{TDC}$  is the time relative to the time at top-



dead center and  $\omega_{cyl}$  is the engine speed (frequency) used to non-dimensionalize time. Using  $\varepsilon$ , stretched variables are introduced and written with lower case letters so that the stretched entropy-like variable is  $s = (S - S_c) / \varepsilon S_c$  where  $S_c$  is the characteristic value of  $S$  at TDC composed using the  $T_{TDC}$  and the corresponding pressure. Using  $s$  the non-dimensionalized energy equation can be rewritten [4] as

$$\frac{Ds}{d\tau} = I_0 \exp[-(\gamma-1)(\tau^2 - s_v)] \exp[-s] \quad (1.2)$$

where  $\gamma$  is the ratio of the specific heats,  $\tau$  is the normalized and stretched time variable, and  $s_v$  is the volume average of  $s$ . The evolution of the energy equation is proportional to the ignitability, which is defined as

$$I_0 = \frac{qAe^{(-E/RT_{TDC})} Y_0^r}{\omega_{cyl} c_p T_{TDC} \sqrt{\varepsilon}} \quad (1.3)$$

where  $Y_0^r$  is the characteristic value of the combined reactant mass fractions,  $Y_F^n Y_O^m$ , appearing in Eq. 1.1. Written in this manner the energy/entropy equation can be solved analytically (see Ref. [4] for complete details on the present analysis) to yield

$$(t_{ig} - t_{TDC}) \omega_{cyl} = \sqrt{\varepsilon} \operatorname{erf}^{-1} \left[ \frac{2\sqrt{(\gamma-1)/\pi}}{I_0} - 1 \right] \quad (1.4)$$

which is an explicit expression for the ignition time relative to the time at TDC as a function of the ignitability, the engine speed and the parameters  $\gamma$  and  $\varepsilon$ . It is evident that for a given fuel mixture, optimal ignition occurs for a fixed ignitability,  $I_0$ , and this represents a relationship between the compressed gas temperature, the mixture composition, the engine speed and the ignition time.

This simple relationship has the best chance of performing well for fuels whose ignition time has a simple Arrhenius temperature dependence and a simple dependence on the mixture composition, because they are most likely to approximate the simple kinetic behavior assumed in the analysis. As evidenced in Fig. 1.5 where ignition delays for constant volume systems are simulated, hydrogen is one such fuel. In Fig. 1.5 the ignition delays for lean mixtures are shown to correlate well with the inverse of the mixture fraction, a conserved scalar that describes the mixture stoichiometry. Using readily available data such as this, ignition times are predicted in Fig. 1.6 for a subset of the data presented in Fig. 1.2. The ignition time data shows the inverse error function behavior that is expected from Eq. 1.4 and the predicted ignition times are well correlated with the simulated ignition times.

## 1.4 An Engine Control Algorithm

More significant than the prediction of the ignition times is the fact that a relationship between the control variables and the engine operating conditions has been obtained. Taking the differential of the ignitability and setting it equal to zero

$$\frac{d\omega_{cyl}}{\omega_{cyl}} - r \frac{dY_F}{Y_F} - \left( \frac{T_{act}}{T_{TDC}} - \frac{1}{2} \right) \frac{dT_{TDC}}{T_{TDC}} = 0 \quad (1.5)$$

provides a relationship between the fractional changes in temperature that are needed to maintain a fixed ignition time as the engine speed and fuel load change. While the coefficients in front of these fractional changes,  $r$  and some function of the activation energy, are generally unknown for practical fuels, they are of a sufficiently simple form that an engine controller could tune itself “on the fly.”

## 1.5 Summary

In order to commercialize HCCI engines, a means will be required for adapting to changing operating conditions while maintaining optimum ignition timing. Using a simplified energy equation, it is possible to develop a model that, once empirically tuned, can predict ignition delays for compression ignition of simple fuels. Furthermore, a relationship between engine operating conditions and a control variable has been developed.

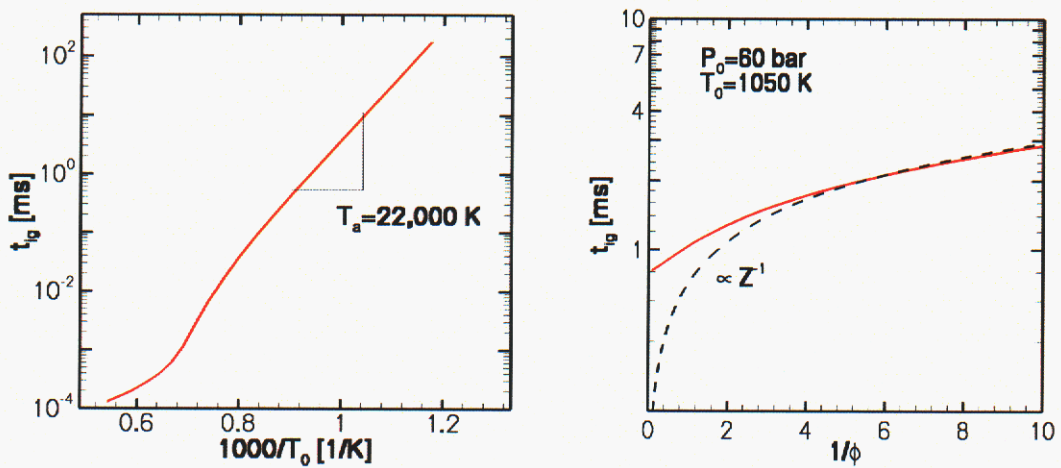


Figure 1.5. Ignition delays for hydrogen mixtures in constant volume systems at 60 bar pressure as a function of temperature for  $\phi=1$  (left) and stoichiometry with initial temperatures being 1050 K (right).

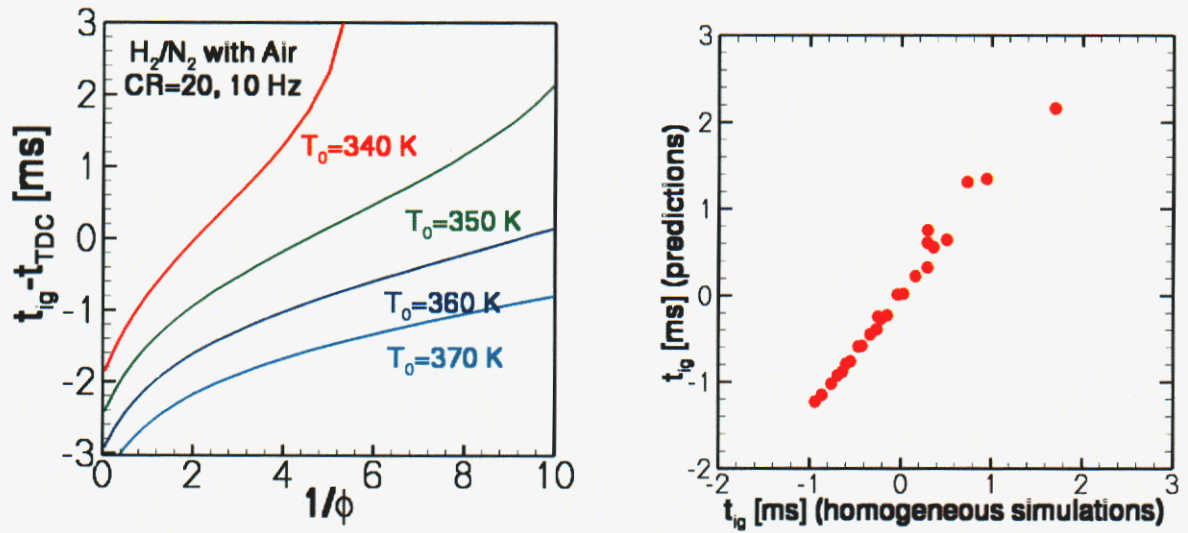


Figure 1.6. Ignition delays relative to TDC are shown for a subset of the data presented in Fig. 1.2 along with predictions based on Eq. 1.4.

### References

1. Christensen, M., Johansson, B. and Einewall, P., *SAE Paper No. 972874* (1997).  
Also Christensen, M., Hultqvist, A. and Johansson, B., *SAE Paper No. 1999-01-3679* (1999).
2. Kelly-Zion, P. L. and Dec, J. E., *Proceed. Comb. Instit.*, 28 (2001).
3. Kaahaaina, N., Simon, A., Caton, P., and Edwards, C., *SAE Paper No. 2001-01-0549* (2001).
4. Linan, A., and Williams, F. A., *Combust. Sci. Tech.*, 105:245-263 (1995).



## **2. An Integrated Computational Method to Study the Effect of Inhomogeneities in HCCI Combustion**

### **Role of Inhomogeneities**

The benefits of homogeneous-charge compression-ignition (HCCI) engines are well known [1,2]. HCCI engines promise high efficiency and low emissions. Unfortunately, HCCI engines also present several challenges. Significant challenges include the control of the ignition timing over a reasonable load-speed map, the control of the heat-release rate, and the control of certain emissions, mainly unburned hydrocarbons and CO. Inhomogeneities are believed to affect each of these three challenging areas as will be described in subsequent sections. In certain situations, inhomogeneities may be beneficial, while in others they are probably detrimental. The present work includes the development of a model uniquely suited to studying the effect of inhomogeneities on ignition timing, the rate of heat release and emissions. The inhomogeneities in the cylinder are characterized from LES of an HCCI engine during the intake and compression strokes. Finally, the existence of inhomogeneities in the mixture may give rise to a range of ignition delays in the mixture, and hence, the possible coexistence of ignition front propagation. Ignition front propagation is observed both in ODT and DNS simulations following the homogeneous ignition of the most ignitable region. The character of the front propagation is explored in greater detail with DNS of isolated hot spots.

Finite-rate mixing within an HCCI engine cylinder leads to small and large-scale inhomogeneities whose distinct effects should be represented in a model accounting for inhomogeneities in HCCI combustion. Examples of mixing processes of relevance include fuel-air mixing, reactant-residual gas mixing and thermal mixing in boundary layers. Each of these may lead to small and large scale inhomogeneities in the temperature and reactant concentrations. These inhomogeneities create a distribution of thermochemical states in which certain fluid elements are more ignitable than others. This can be viewed as a distribution of ignitabilities, defined in Section 1, with the most ignitable element determining the start of combustion. Compression heating resulting from the first ignited element leads to the subsequent ignition of slightly less ignitable mixtures until all of the chamber has ignited or the expansive cooling associated with the piston motion prevents further ignition.

Inhomogeneities have previously been recognized as affecting heat release and emissions in HCCI combustion. However, previous modeling approaches have focused on mean temperature gradients, neglecting the small-scale temperature fluctuations and neglecting equivalence ratio fluctuations entirely [11,14]. The present approach seems to be unique in accounting for these fluctuations, which are demonstrated to be significant in this work.

### **One-dimensional Turbulence (ODT) Model for HCCI**

This novel turbulence modeling approach captures key mechanisms of multidimensional turbulent flow within a one-dimensional description. This method has



recently been extended to turbulent reacting flows by coupling the model to Sandia's CHEMKIN chemical kinetics package. The resulting formulation is fully resolved in time and in space – in one dimension – and captures relevant fine-scale processes that govern turbulence-chemistry interactions like inhomogeneous autoignition. For engine simulations, the model was further extended to account for compression heating and expansion cooling. The ODT model captures the key physics of both large and small scale inhomogeneities. ODT is used here in conjunction with LES and DNS that each provide higher fidelity for large and small phenomenon, respectively, but do not span the range of large and small scale inhomogeneities. The ODT model is being used to evaluate the significance of mixture composition and temperature inhomogeneities on the ignition and heat release behavior for relevant conditions corresponding to a range of engine speeds, loads and degrees of unmixedness. This evaluation is used to suggest suitable control models that may take advantage of inhomogeneities.

### **Direct Numerical Simulation (DNS) of Ignition Front Propagation**

The autoignition of spatially heterogeneous fuel/air/exhaust gas residual mixtures in a turbulence field is being studied using a high-fidelity numerical approach known as direct numerical simulation (DNS). All of the relevant length and time scales are fully resolved numerically on a computational grid, and coupled with detailed chemical kinetics and transport, this approach provides detailed temporal and spatial information regarding the interaction between relevant ignition chemistry and turbulence. The DNS is used to track the evolution of two initial hot spots representing temperature inhomogeneities which could arise due to imperfect mixing in the bulk gases or due to a temperature gradient between the bulk gases and the wall. The spatial structure and speed of the ignition fronts that develop from homogeneous ignition of the hottest location is analyzed and different modes of ignition front propagation—ranging from premixed flame propagation to developing detonation—are documented.

### **Large-eddy Simulation (LES) of Mixture State in HCCI Combustion**

Local instantaneous mixture states in HCCI engines are dominated by the geometric features of the port, valve and cylinder arrangement. These features, coupled with other effects such as wall cooling and the periodic motion of the piston, impose 1) a broadband vortical character on the flowfield and 2) unsteady inhomogeneities over a wide range of time and length scales. The induced swirling, recirculating and inhomogeneous flow features play a major role in the ignitability characteristics and the resultant combustion processes after ignition occurs.

With the advent of massively parallel computer hardware, LES now provides a means to study the coupled combustion and turbulent mixing processes described above in realistic geometric domains and in parameter spaces that are unattainable using DNS techniques. LES is a technique that provides a time-accurate multiple-time multiple-length scale closure by resolving the large energetic scales of a flow and modeling the small or "subgrid" scales.

LES is being used as part of the current project to characterize the large-scale dynamics that occur within an actual HCCI engine. Initial efforts are focused on an

idealized port, valve and cylinder configuration which will be used to characterize the global effects of geometric and operating conditions on local instantaneous mixture states. Simulations will ultimately focus on the Sandia experimental HCCI research engine.

### Integrated Approach to HCCI

A synergistic approach has been developed that combines the small-scale simulation capabilities of DNS and ODT model development with the large-scale mixing dynamics capabilities of LES as shown in Figure 2.1. Turbulence statistics obtained from the LES to characterize the mixture state will help to initialize relevant DNS and ODT simulations at smaller length scales. The large-scale features of the mixture composition will be examined as a function of various operating and boundary conditions in the full domain. In turn, DNS and ODT will provide key physical insight into HCCI combustion that will be used to guide subgrid combustion model development for LES of HCCI. The combined effort will be anchored to the companion Sandia CRF experiment to obtain a clear understanding of dynamic mixture preparation strategies which give optimal ignition, burn-rate and emissions characteristics.

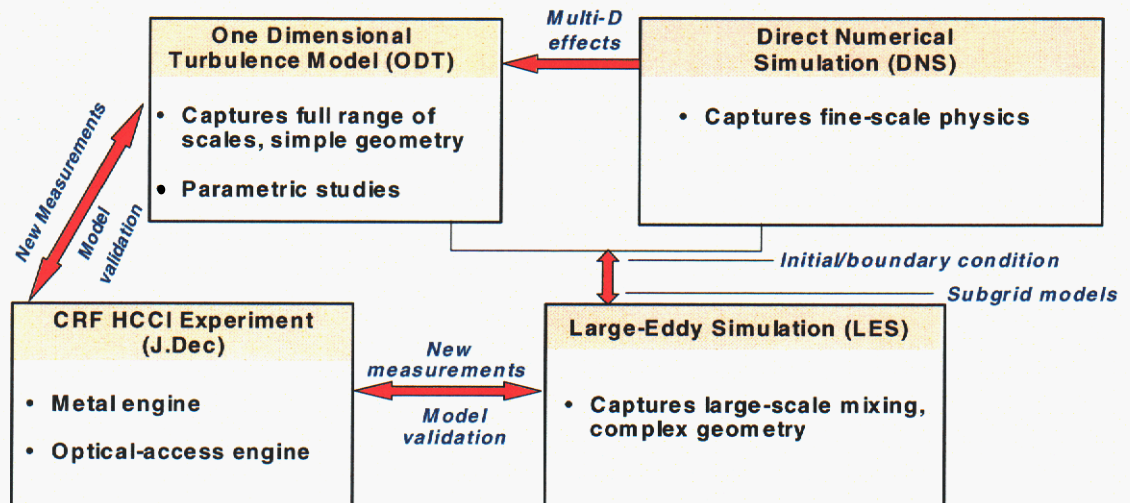


Figure 2.1. Integrated Computational Capability for Understanding and Controlling HCCI Combustion.

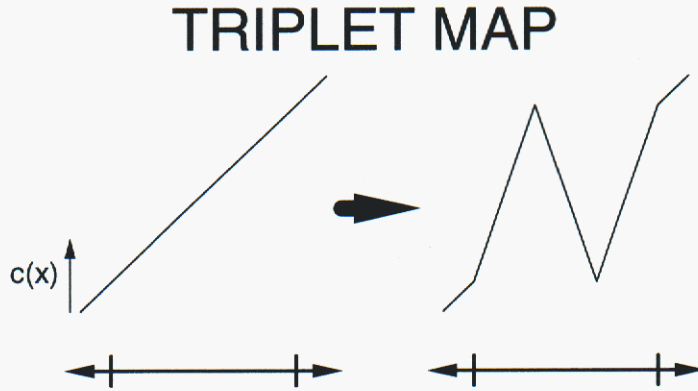


Figure 2.1.1. The triplet map increases scalar and velocity gradients and transfers fluctuations to next smallest scale.

The following section describes the ODT model developed to study the inhomogeneities for HCCI conditions. Subsequent sections describe the observed results in terms of conserved scalar mixing, ignition times and the rate of heat release.

## 2.1 The One-Dimensional Turbulence Model for Engines

### 2.1.1 The One-Dimensional Turbulence Model

To study the effects of incomplete mixing, the present work takes advantage of a stochastic mixing model, the one-dimensional turbulence (ODT) model [3,4,5,6] that is used to simulate an evolving mixture distribution. The ODT model includes two simultaneously evolving processes: the evolution of a reaction-diffusion equation and a turbulent advection model. These processes occur on a one-dimension domain along which the full instantaneous thermochemical state is carried along with the velocity field. The turbulent advection model uses the so-called triplet maps [7] shown in Fig. 2.1.1, which represent eddies. The occurrence of triplet maps are based on a measure of the local instantaneous shear energy obtained from the instantaneous velocity field that is carried on the domain along with all thermochemical scalars. The triplet maps compress property profiles, thereby increasing the local molecular mixing rate. The occurrence of triplet maps is a stochastic process, so each realization is different.

The ODT model simulates the mixing between the initially unmixed fuel and air as well as heat transfer to the walls, resulting in a distribution of mixture composition and enthalpy, with moderate inhomogeneity. This distribution is used to study the effects of inhomogeneities on ignition time. In the present formulation the rate of mixing is governed by the shear kinetic energy associated with the fuel injection and wall boundary layers. The ODT model domain is a 1-D material line of fluid in the cylinder, bounded at either end by isothermal walls, as shown in Fig. 2.1.2; the walls are maintained at 400 K here. Though shown vertical in Fig. 2.1.2, the domain is best considered oriented in the direction of the most significant gradients. Along that domain the full range of length



scales is resolved, including molecular mixing scales and the wall boundary layers. Molecular mixing occurs through the usual diffusional processes using a detailed trans-

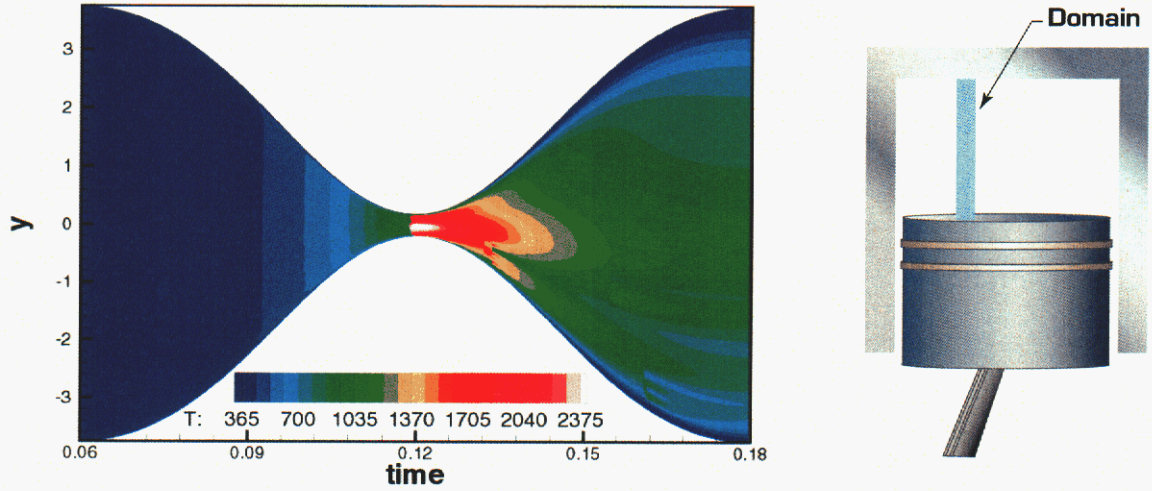


Figure 2.1.2. The ODT domain represents a material line within the cylinder that changes volume in conjunction with the piston motion. The left contour plot shows the domain temperature evolution during a representative cycle with compressive heating, ignition and inhomogeneities associated with imperfect fuel air mixing and wall heat transfer.

port description [15], while turbulent advection is modeled using the ODT model [3,4,5,6].

The particular characteristic that it resolves the full range of scales makes the ODT model useful for the present study of inhomogeneity effects on ignition. While other approaches [2,11,14] consider only the mean scalar quantities, including perhaps mean temperature gradients near the walls, the present study includes scalar field fluctuations about the mean. It is the points of scalar extrema, like fluid elements with the maximum temperature or the richest mixture, that lead to the first ignition points in a mixture with inhomogeneities. These are found here to be significant in determining the ignition timing and the heat release rate.

The domain is initialized with a fuel jet in the center between quiescent slabs of air. The initial velocity of the fuel relative to the air,  $U_F$ , and the length scale of the fuel jet,  $d_F$ , control the kinetic energy available for mixing; the rate of ODT mixing is related to the local shear time scale, which is initially of order  $d_F/U_F$  in the vicinity of the jet. The domain walls move parallel to each other at a constant rate to create continuous shear, resulting in mixing that is analogous to the swirl and tumble motions in an engine cylinder. The rate of wall motion in this direction is set such that a swirl number of unity is maintained. In order to emulate compression, the computational domain shrinks in proportion to the cylinder volume as indicated in Fig. 2.1.2. Figure 2.1.2 also shows the typical time evolution of the temperature on the 1-D domain during a half cycle, with compression heating of the reactants, ignition near TDC and expansion cooling. The mixture doesn't burn to the walls because the walls are kept at 400 K and because the wall layer tends to be leaner.

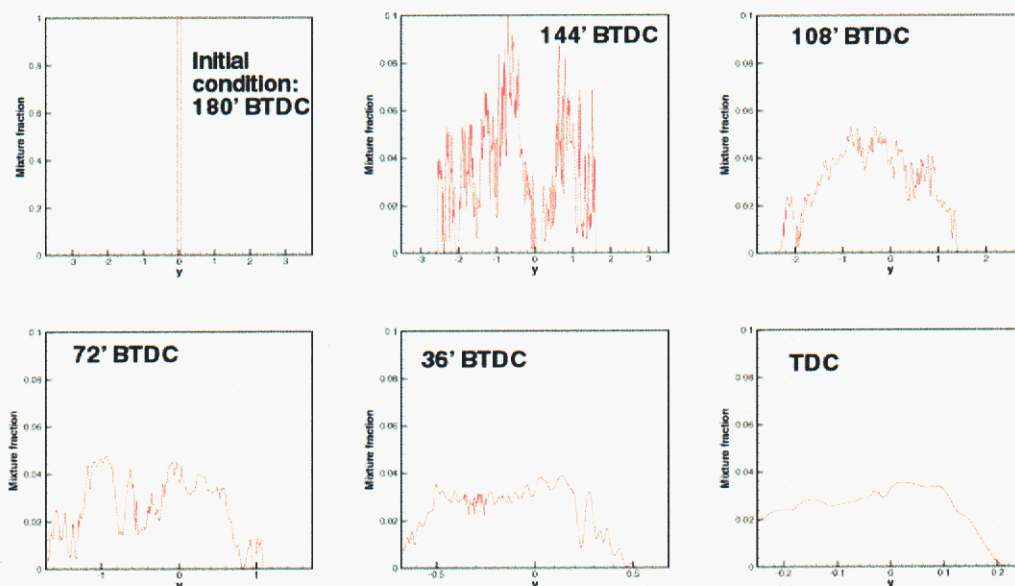


Figure 2.1.3. The evolution of a conserved scalar on the ODT domain is shown during a representative cycle. The mean mixture fraction is approximately 0.02.

## 2.1.2 Evolution of the Mixture Composition

To illustrate the evolution of scalars in this model, Fig. 2.1.3 shows snapshots of the mixture-fraction field, computed from elemental mass fractions of species carried on the domain, during the compression stroke. The mixture fraction is zero in air and unity in the initial heptane-air fuel jet. Note that the "fuel jet" starts out partially mixed. With this mixture the stoichiometric mixture fraction is 0.1 and the cylinder averaged mixture fraction is about 0.02, giving an overall equivalence ratio of about 0.2. The current initial conditions are unmixed fuel and air at 180 BTDC, and the initial distribution of the mixture fraction is a double delta function. The particular velocity field that initializes this calculation is a low-mixing-rate case leading to relatively large inhomogeneities. Fig. 2.1.3 shows a series of snapshots, starting with the initial condition, a top-hat profile. Turbulent mixing, described through triplet maps, leads first to large fluctuations and then molecular mixing reduces those fluctuations. Note that the domain width is changing here. In this particular realization, there is some pure air that survives to TDC on the right side of the domain, and the mixture is richer than the overall equivalence ratio in the center of the domain. The mixture fraction distribution evolves during the compression stroke from bimodal to a single mode as the variance decreases and the mixture becomes increasingly uniform. However, the results indicate that the PDF develops a negative skewness that indicates a tendency for very lean pockets to remain, as is evident in the particular realization in Fig. 2.1.3.

If mixture fraction is viewed as a measure of the ignitability, then it appears that the further the mixing progresses the narrower the range of ignitabilities will become. However, wall heat losses, which may increase with better mixing due to increased heat transfer to the walls, introduce a tendency of the ignitability distribution to broaden as mixing improves.



### 2.1.3 Mixing Effects on Ignition Behavior

To analyze the effect of mixture inhomogeneities on the ignition time, two series of numerical experiments, each at a different overall stoichiometry for hydrogen-air mixtures, were carried out as indicated in Table 2.1.1. For each series, simulations were conducted at three different fuel-air mixing rates. The resulting degree of unmixedness or inhomogeneity in the mixture fraction at TDC is expressed as

$$\psi_0 = \frac{1}{nL_0} \sum_{i=1}^n \left\{ \int_{-L_0/2}^{L_0/2} [Z_i(y) - \bar{Z}_i]^2 dy \right\} \quad (2.1.3.1)$$

where  $Z_i(y)$  is the mixture-fraction spatial profile for realization  $i$ ,  $\bar{Z}_i$  is the average of  $Z_i(y)$  over  $y$ , and  $L_0$  is the domain length at TDC. The summation represents an ensemble average over the  $n=24$  realizations for each set of conditions. The unmixedness is thus the average of the cycle-resolved mixture-fraction variances. The unmixedness can also be represented using the mixture fraction PDF; these are shown in Fig. 2.1.4 where the negative skewness described before is evident.

As described above, the fuel and air are initially unmixed when the simulation begins at one half revolution before TDC, also known as bottom dead center. During the ODT simulation of the compression stroke, the fuel and air mix and their distribution throughout the cylinder becomes increasingly uniform. The three different degrees of unmixedness were obtained by varying the initial kinetic energy of the fuel relative to the air, determining the energy available for mixing.

Mixing tends to bring the fuel-air composition towards the mean value, reducing the richest and leanest deviations from that value. If the mixture fraction is viewed as a measure of the ignitability, as is suggested in Eq. 1.4 and Fig. 1.5, then greater mixing rates reducing the maximum mixture fraction will result in later ignition. This effect is amplified by the fact that greater mixing energy also increases the wall heat transfer,

Table 2.1.1. Mixture mean composition, fuel-stream initial conditions, and unmixedness for simulations with  $H_2/N_2$  mixing with air. For all simulations the initial temperature is 350 K, the revolution frequency is 20 Hz and the initial domain length is 10 cm subject to compression by a factor of twenty at TDC. The observed probability of ignition,  $P_{ign}$ , is also indicated, as is the average ignition time, both defined in the text.

	$\bar{Z}$	$\phi$	$U_F$ [m/s]	$d_F$ [cm]	$\psi_0$	$P_{ign}$	$t_{ig}$ [ms]
A	0.093	0.24	15.6	1.5	$0.6 \cdot 10^{-3}$	0.33	1.3
B	0.093	0.24	10.4	1.5	$1.2 \cdot 10^{-3}$	0.58	1.0
C	0.093	0.24	5.2	1.5	$2.4 \cdot 10^{-3}$	1.00	0.4
D	0.13	0.36	18.6	2.1	$0.6 \cdot 10^{-3}$	0.79	0.6
E	0.13	0.36	11.2	2.1	$1.2 \cdot 10^{-3}$	1.00	0.4
F	0.13	0.36	7.6	2.1	$2.4 \cdot 10^{-3}$	1.00	0.2



thereby removing more heat from the mixture. This temperature reduction, though only on the order of tens of degrees away from the walls, significantly influences the ignitability because of its strong temperature dependence.

Pressure-time traces for the full set of simulations described in Table 2.1.1 are shown in Fig. 2.1.5 where upper plots correspond to greater homogeneity. The particular sets of initial temperatures,  $T_{BDC}$ , and overall mixture composition were selected to represent marginal ignition cases. For  $T_{BDC}=350$  K, an adiabatic homogeneous mixture at  $\phi=0.36$  will ignite at a speed of 20 Hz, but one at  $\phi=0.24$  will not ignite.

The effect of finite-rate fuel-air mixing on the ignition and its timing is considered first. With fluctuations in the mixture fraction resulting from incomplete mixing, a fraction of the  $\phi=0.24$  cases ignite, with that fraction increasing to 100% for the least mixed case, as indicated in Table 2.1.1. The timing of the ignition also moves forward as the degree of inhomogeneity increases as seen in Fig. 2.1.5. This is particularly evident for the mixtures at  $\phi=0.36$ . The advance in the ignition timing is explained by the fact that less mixing leads to richer fluid elements that ignite earlier (cf Fig. 1.5).

The effects of heat losses are required to explain the remainder of the results. Despite the fact that the mixture at  $\phi=0.36$  should ignite when completely homogenized, some of the realizations at the highest mixing rate do not ignite. It is evident that these fail to ignite because there is sufficient heat transfer to reduce the temperature throughout the domain enough to prevent ignition. At  $\phi=0.36$  it is only necessary to reduce the temperature by  $O(10)$  degrees to prevent ignition. This indicates that high mixing rates can have an additional negative impact on cases where ignition is marginal since the rate of heat loss to the cylinder walls will be greater. Naturally, high mixing rates are

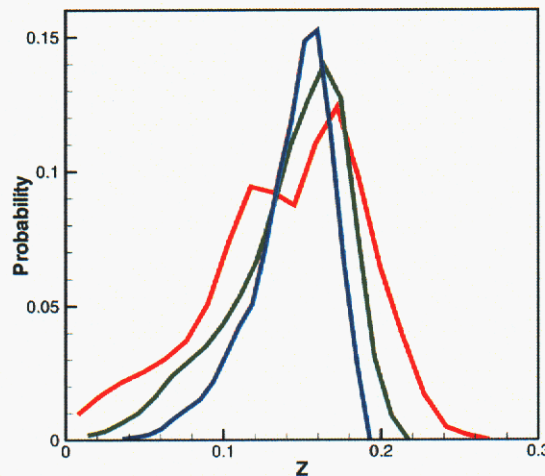


Figure 2.1.4. The PDF of the mixture fraction at TDC is shown for series D, E and F with the narrowest PDF corresponding to D and the widest to F.

desirable for overall equivalence ratios that would lead to earlier-than-desired ignition in the absence of heat losses.

A series of simulations using n-heptane was also conducted as shown in Fig. 2.1.6. To facilitate appropriate mixing rates without excessive computational costs, the initial fuel

jet is composed of a mixture of 30% heptane and 70% air by volume. Due to partial premixing, less subsequent mixing is required to achieve a given degree of homogenization, so the initial jet velocity is reduced accordingly. Simulations are conducted for three equivalence ratios with  $\phi = 0.2, 0.3$  and  $0.4$ , each at two mixing rates, with four realizations conducted for each of the six conditions. Results similar to those found for  $H_2/N_2$  mixtures are found for heptane. Higher mixing rates tend to reduce the ignitability. For compositions that ignite easily, like that for  $\phi=0.4$ , the higher mixing rates lead to more desirable ignition timing. For leaner mixtures, greater mixing rates led to somewhat late ignition for  $\phi=0.3$  and failed ignition for  $\phi=0.2$ .

#### 2.1.4 Relating Ignition Times to Ignitability

Fuel-air inhomogeneities and heat losses both affect the distribution of local ignitabilities in Eq. 1.3.  $I_0$  can be used with Eq. 1.4 to determine the ignition time if the joint distribution of  $Z$  and  $T$  at TDC is known. In the present case  $I_0$  is evaluated using the joint distribution of  $Z$  and the total enthalpy, both of which are unaffected by chemical reactions (except for the effect of compression heating on the enthalpy), at TDC. Using scalars unaffected by chemical reactions is often desirable for CFD applications where chemical-kinetic scales are not resolved, though this is not an issue here. The enthalpy is converted to temperature assuming a linear relationship between  $c_p$  and  $Z$  that is appropriate before ignition. This approach also avoids the relatively small changes in temperature due to pre-ignition heat release; however, it does not account for the increase in enthalpy due to compression heating. Using values at TDC, the ignition times for the 144 realizations described in Table 2.1.1 are compared with those predicted by Eq. 1.4 Fig. 2.1.7 (realizations that did not ignite do not appear). Despite the many approximations involved in developing Eq. 1.4, the predicted ignition times are well-correlated with those simulated; Fig. 2.1.7 shows that Eq. 1.4 predicts a somewhat stronger dependence of ignition time on ignitability than is observed with detailed chemistry and mixing. It is likely that much of this stronger dependence is related to compression work done on the mixture by heat release; this increases the enthalpy leading to earlier predicted ignition, especially true when ignition is near or before TDC.

A certain fraction of the mixtures do not ignite for the conditions chosen here, particularly for sets A and B. For each set, the fraction that did ignite in a timely manner is indicated in Table 2.1.1. Here, igniting in a timely manner is determined to be 50% of total heat release having occurred before 2 ms after TDC. Equation 1.4 has no solution for ignitabilities that are too small, and this lack of solution predicts the extinction observed in sets A and B, but not that observed in D. The failure to predict extinction for set D seems to arise from the simplified linear correlation between the ignition kinetics and  $Z$  used in Eq. 1.4 and taken from Fig. 1.5 of the previous chapter. This yields slightly greater ignitability for richer mixtures than would be obtained using a better description of the reaction rate dependence on mixture composition. The maximum ignitabilities for these realizations in question are all within 20% of being too low for ignition according to Eq. 1.4. The mean ignition times for each of the six sets are shown in Table 2.1.1. These are calculated from only the realizations in which ignition occurred. Comparing these mean ignition times for sets D, E and F with the ignition time for a homogeneous

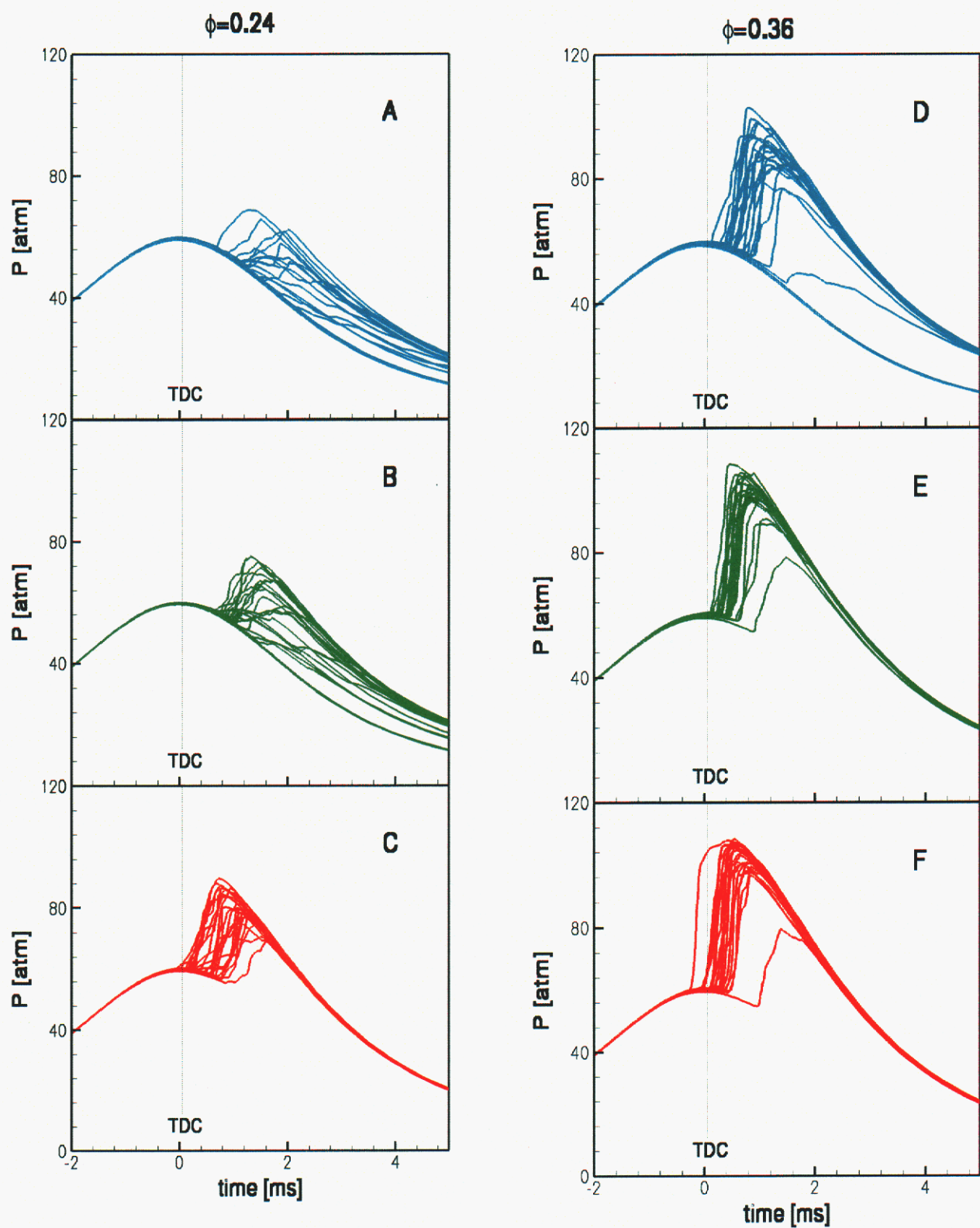


Figure 2.1.5. Pressure-time traces for simulations described in Table 2.1.1. Each panel contains 24 realizations for one of the six initial conditions.



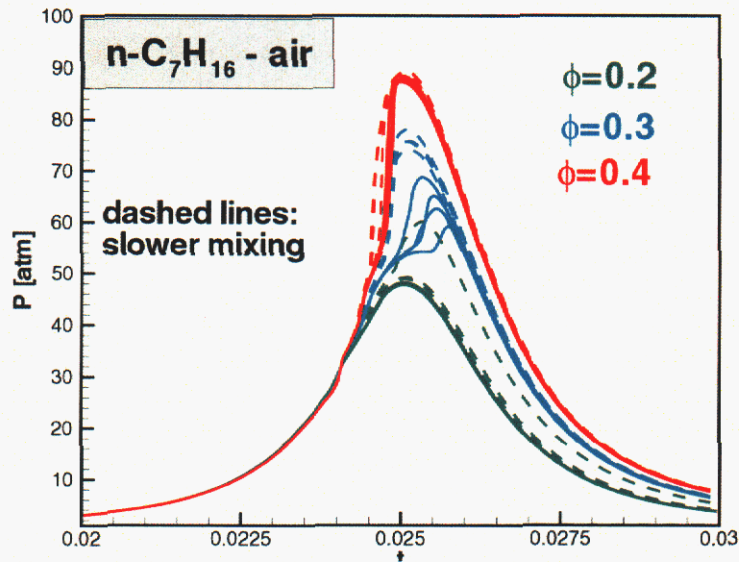


Figure 2.1.6. Pressure-time plots for n-heptane air mixtures at two different mixing rates and three different equivalence ratios.

mixture,  $t_{ig}=0.49$  ms, it is evident that ignition for the less homogeneous cases is earlier. Similarly, for sets A, B and C, ignition would not occur at all for the homogeneous case, but does occur reliably for set C, the most poorly mixed of the three. Models that account for variations in the mean temperature near walls, but not for local fluctuations in mixture composition and temperature, like [11,14], are not likely to predict this shift in the ignition timing.

### 2.1.5 Inhomogeneities and the Rate of Heat Release

One additional challenge associated with HCCI combustion is the possibility of overly rapid heat release. For a truly homogeneous system, the pressure rise associated with heat release takes on the order of ten microseconds; this is less than typical acoustic time scales in the cylinder resulting in the possibility that compression waves may result in noisy operation and possible engine damage. This behavior would be analogous to engine knock, though the waves produced will be of lesser strength than typical of stoichiometric spark-ignited engine conditions. For a less homogeneous system, the heat release and pressure rise can be spread out over hundreds of microseconds. This occurs because fluid elements with different thermochemical properties ignite at slightly different times during the compression process. The effect of inhomogeneities is illustrated by the rate of pressure rise. Figure 2.1.8 shows two pressure-time traces, one corresponding to a completely homogeneous case and the other corresponding to incomplete mixing; in the latter case the entire mixture is lean with a mean equivalence ratio of 0.4 and a standard deviation of 0.1 in equivalence ratio units.

The degree of inhomogeneity can affect the rate of heat release, and this is particularly true when ignition occurs after TDC. Figure 2.1.9 shows contour plots for  $H_2/N_2$  ignition for greater and lesser degrees of mixing. In order to obtain results where both realizations ignite, the more homogeneous mixture on the left of Fig. 2.1.9 is richer than that on the right. With greater homogeneity, the heat release occurs over roughly three crank-angle degrees; with greater inhomogeneity, the heat release occurs over twelve degrees. The latter results are more significant in that a fraction of the heat release occurs through premixed flame propagation. This can be observed in Fig. 2.1.10 where the edges of the high temperature regions correspond to high rates of heat release characteristic of premixed flame propagation. Initially, a single ignition kernel is visible which grows due to propagation. A short time later a second ignition kernel appears, and some time later the heating resulting from these initial ignition kernels ignites most of the rest of the domain, with ignition occurring at multiple points. At later times spontaneous autoignition is inhibited in this case because the domain is already expanding, and undergoing expansion cooling, when the ignition first occurs.

### **2.1.6 On the Merits of the ODT-based Model for Studying HCCI combustion**

To conclude the discussion of this model for studying HCCI combustion, the limitations and strengths of the ODT-based model are summarized. The ODT-based model is able to capture certain key physics that other models, short of DNS, cannot capture. These include the extrema in the ignitability, composed from the joint PDF of the composition and enthalpy, that determines the first ignition time while simultaneously resolving molecular processes like flame propagation. The ODT-based model alone is probably insufficient to use as a design tool, because it retains limited information about multidimensional geometries. That is, if squish introduces rapid mixing near TDC, then this effect must be artificially introduced into the model. However, the ODT model could be used in conjunction with CFD codes that solve the large scale mixing. In this case it is a kind of subgrid scale model; the CFD code would provide the ODT subroutine with information on global mixing rates or energy dissipation rates. In this sense it could be implemented in a manner similar to the representative interacting flamelet (RIF) model or to unsteady Lagrangian flamelets [9]. For example, Chakravarthy and Menon have used the similar LEM model as a subgrid scale model for LES [10].

The ODT based model has certain potential advantages over mixture-fraction-based models like [9]. First, it is not restricted to two stream mixing problems. For example, it can accommodate enthalpy not correlated with mixture fraction due to wall heat transfer or due to EGR and residual gases with different stoichiometries and enthalpies. Furthermore, wall heat transfer is specifically present in the model, affecting a limited physical region of the fluid. While it is possible to consider a distribution of Lagrangian flamelets with differing enthalpies, a continuous distribution of enthalpies occurs within the ODT model.

Another model for HCCI combustion is the multi-zone model of Aceves et al [11]. In this model the mean mixture distribution is calculated using a RANS code like Kiva and a number of homogeneous zones are created to model regions of the charge. The ODT-based model can be thought of as having a more continuous distribution of zones, but the key advantages of the ODT-based model is that it includes the fluctuations of the mixture

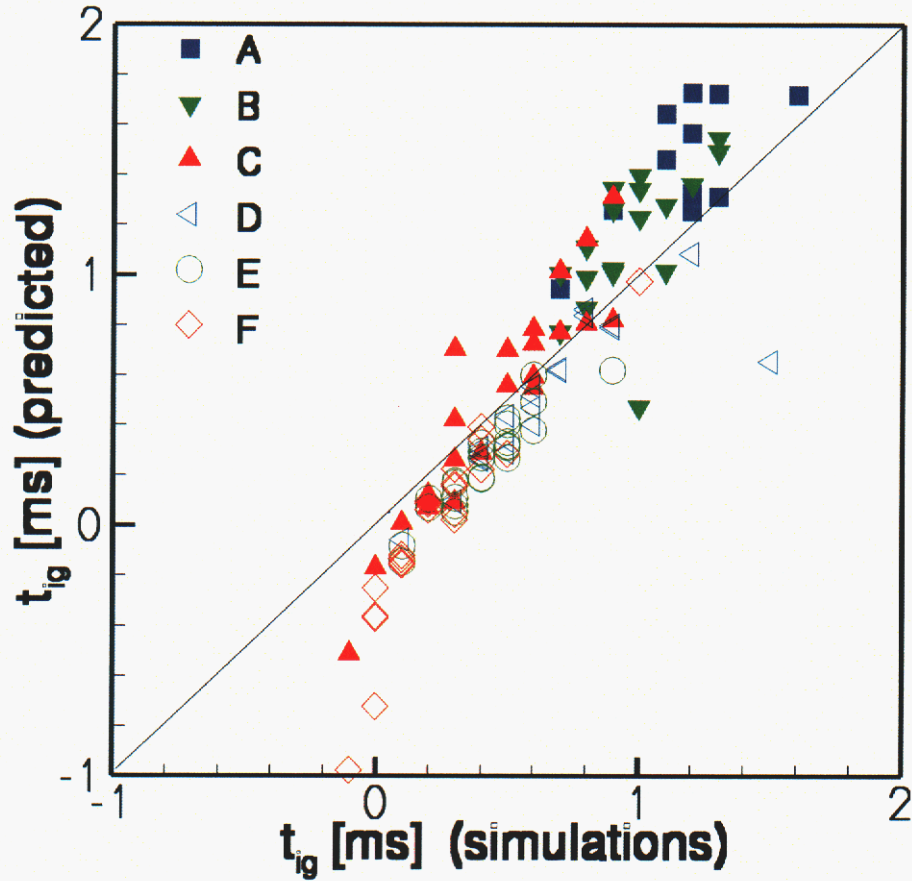


Figure 2.1.7. A comparison of ignition times from individual simulations with ignition times predicted by Eq. 1.4 evaluated at TDC.

inhomogeneities that result from finite rate mixing. These small-scale inhomogeneities lead to the extrema in thermochemical properties that govern the first ignition.

Because it can resolve the full range of length scales in a boundary layer, the ODT model is particularly useful for studying wall heat transfer and the associated local changes in enthalpy. The advantage of this is that wall gradients that may affect combustion of near-wall regions might be better modeled. This is an ongoing research focus [12].

### 2.1.7 Summary

To summarize, a one-dimensional model has been developed that resolves the full range of length scales. The model incorporates compression and wall effects. Turbulent mixing occurs through the triplet-map procedure. The model has been used here to investigate the effects of inhomogeneities on the ignition and burn rate in HCCI



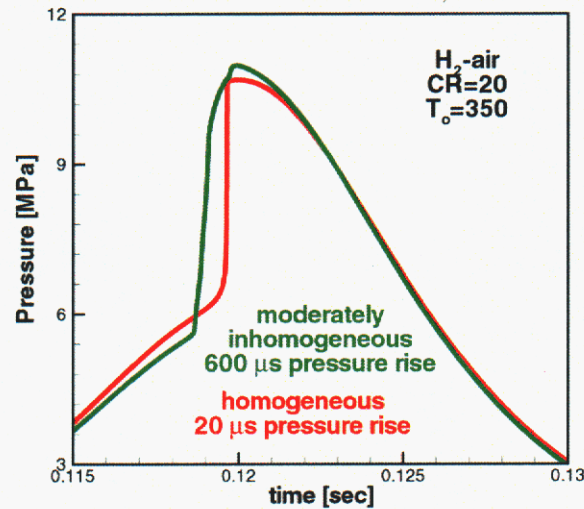


Figure 2.1.8. The rate of pressure rise is modulated by inhomogeneities. The mean equivalence ratio is 0.4; the standard deviation for the moderately inhomogeneous case is 0.1.

combustion. Inhomogeneities are observed to affect the ignitability and burn rate; in general greater inhomogeneities are correlated with earlier ignition and moderated rates of heat release. Multiple ignition kernels and flame propagation are observed in certain situations.

The effects of inhomogeneities on ignition timing in a nearly homogeneous mixture subject to compression heating have been investigated. Simulations of mixing and compression heating leading up to ignition were conducted using a new ODT-based model. For the conditions examined, even relatively small degrees of inhomogeneity are observed to have a significant effect on the ignition timing and even on the ability of the mixture to ignite. This effect can be correlated with the ignitability, which is related to the Damköhler number for ignition.

The ignitability metric used here is potentially applicable to any fuel whose ignition delay is of Arrhenius form over the relevant temperature range. This criterion excludes fuels such as n-heptane and diesel mixtures that undergo multistage ignition over the time frames of interest, but should include other fuels of interest such as natural gas, iso-octane and gasoline-type fuels. For such fuels, ignition data plotted as in Figs. 2 and 3 will allow the determination of the effective activation temperature and the ignitability prefactor  $qB/c_p$ . No additional chemical-kinetic information is needed, a point particularly useful if the fuel is a mixture of unknown composition. If successful, this new single-parameter characterization of compression ignition will greatly simplify data analysis and interpretation.

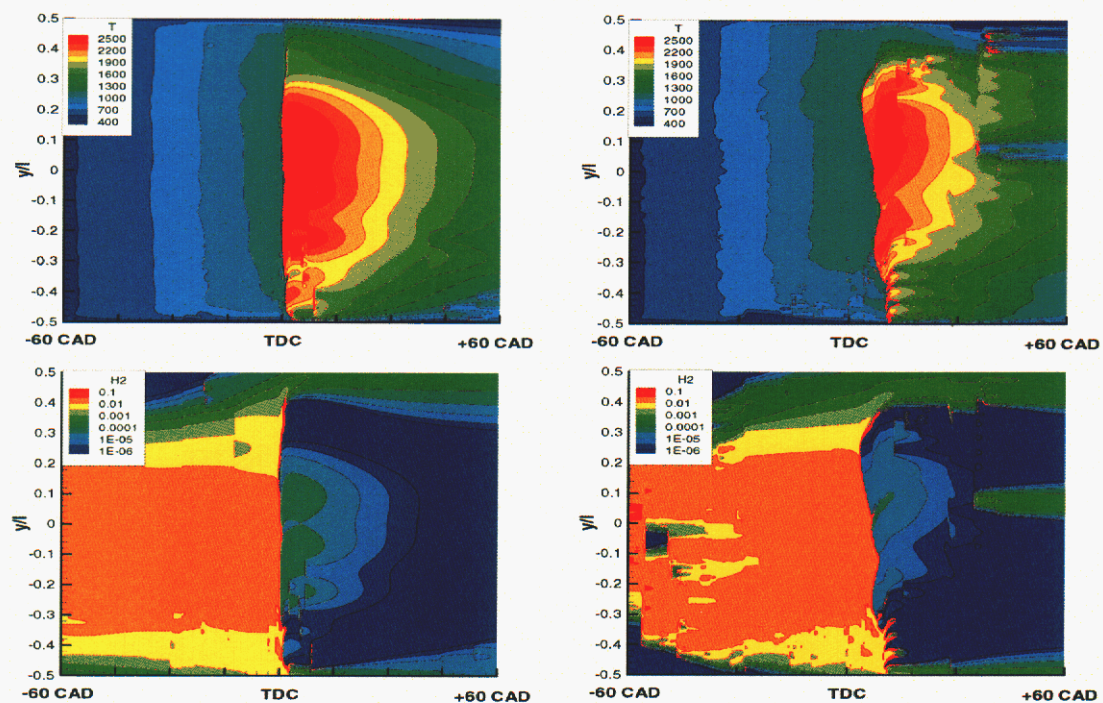


Figure 2.1.9. Temperature (top) and hydrogen (bottom) contour plots are shown for well-mixed (left) and less well-mixed (right) realizations.

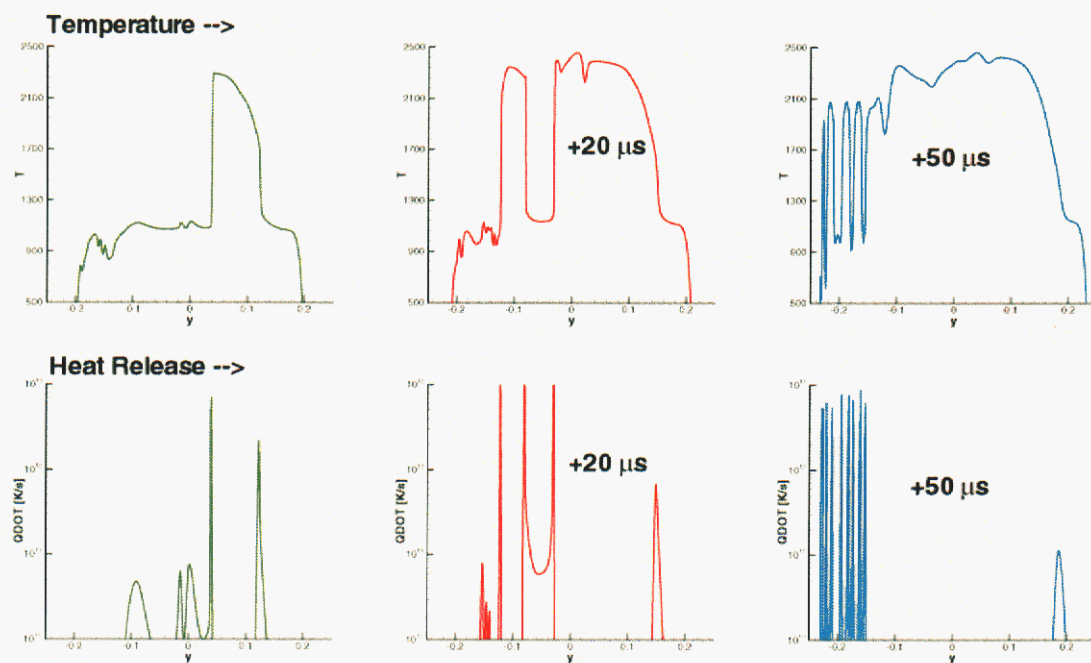


Figure 2.1.10. Temperature and heat release profiles at individual time instants in for the simulation shown in the right half of Fig. 2.1.9.

## References

1. Christensen, M., Johansson, B. and Einewall, P., *SAE Paper No. 972874* (1997).  
Also Christensen, M., Hultqvist, A. and Johansson, B., *SAE Paper No. 1999-01-3679* (1999).
2. Kelly-Zion, P. L. and Dec, J. E., *Proceed. Comb. Instit.*, 28 (2001).
3. Kerstein, A. R., *J. Fluid Mech.*, 392:277-334 (1999).
4. Kerstein, A. R. and Dreeben, T. R., *Phys. Fluids*, 12:418-424 (2000).
5. Echehki, T., Kerstein, A. R., Chen, J.-Y. and Dreeben, T. R., *Comb. Flame*, 125:1083-1105 (2001).
6. Hewson, J. C. and Kerstein, A. R., *Comb. Theory Modeling*, 5:669-697 (2001).
7. Kerstein, A. R., *J. Fluid Mech.*, 231:361-394 (1991).
8. Echehki, T. and Chen, J. H., *The 2nd Joint Meeting of The U.S. Sections of The Combustion Institute*, Paper No. 184, March 25-28, 2001, Oakland, CA.
9. Pitsch, H., Barths, H. and Peters, N., *SAE Paper 962057* (1996).
10. Chakravarthy, V. K. and Menon, S., *Combust. Sci. Tech.*, (to appear 2001).
11. Aceves, S. M., Flowers, D. L., Westbrook, C. K., Smith, J. R., Pitz, W., Dibble, R. W., Christensen, M. and Johansson, B., *SAE Paper 2000-01-0327* (2000).
12. Kerstein, A. R., Schmidt, R. C., Wunsch, S., Ashurst, W. T., Nilsen, V. and Dreeben, T. R., Technical Report SAND2001-8108, Sandia National Laboratories (2001).
13. Linan, A., and Williams, F. A., *Combust. Sci. Tech.*, 105:245-263 (1995).
14. Kraft, M., Maigaard, P., Mauss, F., Christensen, M., and Johansson, B., *Proc. Combust. Inst.*, 28:1195--1201 (2000).
15. Kee, R. J., Dixon-Lewis, G., Warnatz, J., Coltrin, M. E., and Miller, J. A., Technical Report SAND86-8246, Sandia National Laboratories, (1986).



## **2.2 Direct Numerical Simulation: A Method to Study the Modes of Autoignitive Propagation**

### **2.2.1 Introduction**

Lean premixed autoignition of fuel-lean hydrocarbon premixtures at high pressure in the presence of spatial inhomogeneities in temperature or mixture composition has received a lot of attention recently. Understanding inhomogeneous autoignition may lead to the development of control strategies for a mode of combustion being considered for compression ignition automotive engines known as homogeneous charge compression ignition combustion (HCCI). By operating under overall fuel-lean conditions, and hence, at lower temperatures, HCCI can potentially achieve high engine efficiencies comparable to diesel combustion without producing  $\text{NO}_x$  and soot. Because the fuel is sufficiently lean that the normal deflagrative flame propagation found in spark ignition engines may not be possible, the primary mode of combustion in this regime is thought to occur by volumetric autoignition. Therefore, HCCI combustion is primarily kinetically driven. A major challenge posed by this method of combustion is controlling the rate of heat release, and in particular, developing a strategy to spread it out over several crank angle degrees to minimize the generation of damaging engine knock. One possible control strategy is to introduce inhomogeneities in the temperature or mixture composition, tailored to produce the desired heat release rate [1]. In practice, incomplete turbulent mixing and temperature stratification between the bulk gases and the cylinder wall leads to spatial inhomogeneities that also contribute to a range of autoignitive combustion modes distinct from homogeneous autoignition.

The objective of the present numerical study is to understand the evolution of the various modes of autoignitive combustion and their relation to one another — homogeneous explosion, flame propagation, auto-ignition front propagation and developing detonation waves— for a simple model problem of two symmetric hot spots in a uniform premixture field at constant volume. This parametric study will be conducted using one-dimensional direct numerical simulations (DNS) where the initial temperature gradient and the equivalence ratio of the fuel/air premixture are varied. Due to the computational expense of resolving extraordinarily thin ignition fronts at high pressure and tracking their temporal evolution, the chemical kinetics considered are necessarily over simplified, corresponding to detailed hydrogen/air systems. Hydrocarbon fuels, which build on hydrogen as an important subset of the mechanism, will be considered in future studies. A further assumption is that the problem is one-dimensional, since spatial gradients in the scalar fields make it necessary to consider diffusion and convection, in addition to reaction, in at least one spatial direction. Theoretical results will also be presented that capture the qualitative propagation behavior of the ignition fronts.

### **2.2.2 Computational Method and Physical Configuration**

The model problem considered here is a constant volume, one-dimensional domain with two identical hot spots represented by a pair of initial Gaussian temperature profiles.

The initial mixture is uniform and the flow field is quiescent. The parameters varied include the temperature gradient across the hot spot obtained by changing the minimum and maximum temperature,  $T_{min}$  and  $T_{max}$ , and the equivalence ratio,  $\phi$ . Bradley, *et al.* [2] have recently considered a similar problem for a single hot spot and a 50% $H_2$ /50% CO mixture.

The initial pressure is assumed to be 31 atmospheres, corresponding to an adiabatic compression from ambient to a compression ratio of approximately 13:1. The selection of the width of the hot spots is based on inspection of fuel tracer planar laser induced fluorescence (PLIF) sequences of kernels autoigniting in an HCCI engine [3]. These images show ignition kernels of several millimeters in size. Here, we assume the width of each hot spot is 10 mm wide, and their separation distance is 5 mm. The domain size is 3 cm. 24000 grid points are required to resolve the steep gradients in the ignition front structure, giving a grid spacing of 1.25 microns.

The initial conditions for the cases are summarized in Table 2.2.1.

Case	$\phi$	$T_{min}$ , K	$T_{max}$ , K
A	0.3	1050	1100
B	0.3	877	1100
C	0.2	877	1100

Table 2.2.1 Hot spot initial mixture parameters.

In the DNS the conservation equations (continuity, momentum, energy and species including  $H_2$ ,  $O_2$ , O, OH,  $H_2O$ , H,  $HO_2$  and  $H_2O_2$ ) for a compressible flow are solved using an explicit eighth-order accurate finite differencing scheme [4] for approximating spatial derivatives, and a fourth-order accurate Runge-Kutta scheme for time advancement [5]. A modified version of the Navier-Stokes Characteristic Boundary Condition (NSCBC) procedure originally developed by Poinso and Lele [6] is used to account for variable transport and thermodynamic properties. The boundary conditions are periodic. The mixture averaged thermal conductivity is modeled through the approximation suggested by Smooke [7]. The individual species specific heats are obtained as polynomial functions of temperature using the Chemkin thermodynamic database [7]. The diffusion coefficients are obtained by prescription of Lewis numbers for individual species where the Lewis number data is obtained from Smooke [7]. The hydrogen-air chemistry at the various pressures is based on the chemical mechanism of Yetter *et al.* [8] with 9 species and 19 reversible reactions.

### 2.2.3 Results and Discussion

Three cases were simulated for different initial temperature gradients and equivalence ratios described in Table 2.2.1. The evolution of the temperature profile for case A is shown in Fig. 2.2.1 and is representative of all three cases considered except for the manner in which the latter reactants are consumed. It is clear from the evolution that the locations with maximum initial temperature autoignite first, and that subsequent ignition fronts form and propagate into cooler adjacent mixtures. As described by Zel'dovich [9], there are at least three modes of ignition front propagation and this classification is used



to describe the current results. The smallest rates of front propagation would correspond to deflagrations where front propagation is at the laminar burning velocity. For deflagrations, diffusional heat and mass transfer occur at a rate that is fast relative to other time scales. At the other end of the spectrum is propagation by detonation where shock heating of the mixture leads to ignition before it would otherwise autoignite. In between these is the regime of ignition propagation.

The autoignition of the mixture at the location of the initial peak temperature occurs at nearly constant pressure, with a gradual increase in temperature accompanied by exponential growth of a radical pool. The ignition delay is comparable to the corresponding homogeneous ignition delay. In Fig. 2.2.1 thermal expansion associated with the ignition of the first fluid elements compresses the remaining unburned mixture. This occurs at a finite rate limited by the speed of the compression waves as shown in Fig. 2.2.2. Once the compression waves traverse half the domain (since there is perfect symmetry between the pair of hot spots), the original ignited mixture is subsequently compressed while the pressure equilibrates. The compression waves travel at sonic speeds, and hence, may traverse the domain multiple times before all of the fuel is consumed. These waves, under certain conditions, may also coalesce with the ignition waves, steepen immensely, and develop into a detonation wave [2].

The temperature gradients studied here are such that ignition front propagation consumes most of the fuel in the domain after the initial homogeneous autoignition of the hottest mixture. As shown in Fig. 2.2.1 the gas in the center of the domain is partially autoignited at the final time of 0.789 ms, assisted by compression heating from neighboring burned gases. This approach to homogeneous ignition results in an acceleration of the ignition propagation. The rate at which the fuel is consumed by ignition front propagation depends on the gradient in homogeneous ignition delay times associated with the given initial temperature gradient and mixture thermo-chemistry. For shallower initial temperature gradients ignition front propagation is more rapid. The evolution of the heat release, used to determine the propagation velocity, is shown in Fig. 2.2.3. It shows evidence of accelerating heat release as the domain is compression heated by early igniting fluid elements.

When the ignition front velocity approaches the sound speed, as it does in the final microseconds of case A, the compression waves coalesce into a shock wave as observed in Fig. 2.2.2. This development is rapid, occurring between times 0.786 and 0.789 ms when the peak pressure changes from just over 50 atmospheres to over 230 atmospheres. The conditions across the front at 0.789 ms satisfy the normal shock relations and result in peak pressures, temperatures and heat release rates in the domain that are much greater than found with low Mach number flow as seen in Figs. 2.2.1 to 2.2.3. The spike in temperature observed at the final time is due to the strong interactions between combustion and gas dynamics.

In the ignited gases there also exists a temperature gradient that decreases from the mixture ignited first (at  $x$  of 0.75, 2.25 cm) to the mixture ignited last ( $x$  of 1.5 cm). This is characteristic of ignition front propagation at constant volume. The gradient exists due to excess enthalpy beyond the chemical enthalpy of the original mixture at the location of maximum temperature. This is a result of the compression of this gas by combustion of the rest of the mixture in the volume at a higher pressure than the expansion work of the earlier ignited mixture performed at a lower pressure [10]. Given a larger temperature



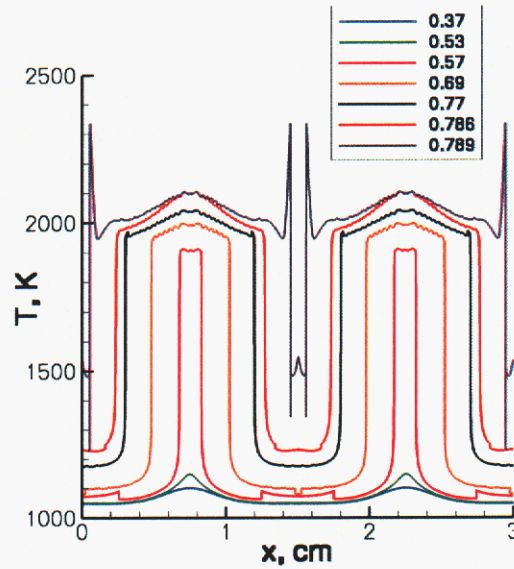


Figure 2.2.1. Evolution of temperature profiles for case A. Time is presented in milliseconds. Hot spots first ignite at 0.55 ms (at 0.75 and 2.25 cm).

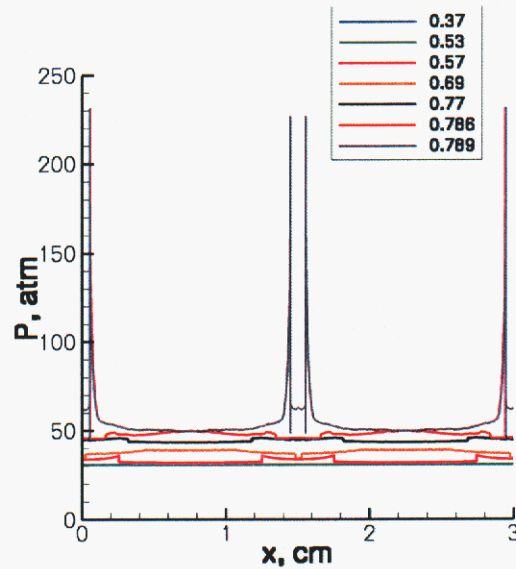


Figure 2.2.2. Evolution of pressure profiles for case A.

gradient, case B shows a similar trend, velocity and less of a propensity to shock than case A. Case C has the same initial temperature gradient as case B but is a less reactive mixture ( $\phi$  of 0.2), and therefore, consumes the fuel at a much slower rate with no evidence of shock formation. For the same temperature gradient, equivalence ratios as lean as 0.1 also show similar behavior. For the leaner equivalence ratios the mixtures are less energetic, and therefore, are not able to produce high enough ignition propagation rates to compress the gases sufficiently to form a shock.

To shed light on the different modes of ignition propagation, the ignition front structure is analyzed in greater detail for the three cases in terms of its instantaneous thermal energy and radical species balances. Since OH is a key radical species involved in chemical chain branching for homogeneous explosion kinetics we monitor its ignition front structure. Figure 2.2.4 shows a comparison of the OH and energy budgets for the least (case C) and most (case A) energetic mixture prior to the formation of a detonation wave. The fronts are propagating from left to right in this figure. The front structure for case C corresponds approximately to a laminar burning deflagration wave with a clear reaction-diffusion balance accounting primarily for changes in OH mass fraction and temperature. This indicates that the ignition propagation itself is not fast relative to premixed deflagration propagation for the less reactive case C. On the other hand, for the most reactive mixture represented by case A (and also for case B though not shown), diffusion is found to play an insignificant role in the balance. Rather, changes in OH mass fraction are due primarily to the production or destruction of OH locally balanced by convective transport. Temperature changes primarily due to the balance between heat release, pressure work, and convection. Depending upon whether an expansion or compression wave is moving past the front at a given instant, convection may be additive or subtractive with reaction locally. This corresponds to a subsonic mode of autoignition deflagration [2,9,11].

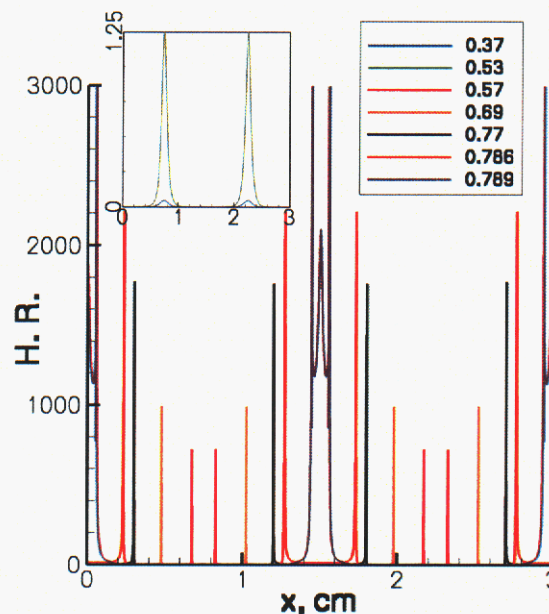


Figure 2.2.3. Profiles of nondimensional heat release rate per unit mass for case A. Time is in ms. The heat release at 0.37 and 0.53 ms (prior to ignition of highest temperature location) is shown in the inset.

Finally, though not shown here, inspection of the energy balance at the point of shock formation for case A reveals that the temperature spikes are a result of additive convective and pressure work contributions.

The temporal evolution of the propagation velocity of the ignition fronts along with the local pressure increase is presented in Fig. 2.2.5 for the three cases. The velocity is computed by monitoring the position of the front in time, where the front is defined as the location of maximum heat release rate (Fig. 2.2.3). Note that the rate of pressure rise

and front acceleration differs considerably for the range of temperature gradients and equivalence ratios considered. Case A has the most dramatic pressure increase (7.4 times) and propagation velocity, in excess of 900 m/s at the end of the ignition process (not shown in the figure), whereas case C has a nearly constant front velocity of approximately 3 m/s (not far from the estimated laminar burning velocity) and the smallest pressure increase (less than 1.4 times). It is noted that laminar burning velocities are not well defined in autoigniting mixtures since they change with the degree of reaction in the preheat zone. For cases A and B the large accelerations in front velocity and pressure jump are observed during the autoignition of the gas between the two hot spots; this is the region where the temperature gradient is smallest. Similar curves of wave speed for a single hot spot were obtained in [2]. The range of front speeds obtained for cases A and B are consistent with those estimated by Hultqvist *et al.* [3], and are much larger than can be supported by normal flame propagation. It is of interest to note that their experimental observations also indicate the formation of sharp boundaries between burned and unburned gases only in the late stages of HCCI combustion, suggestive of the existence of ignition front propagation.

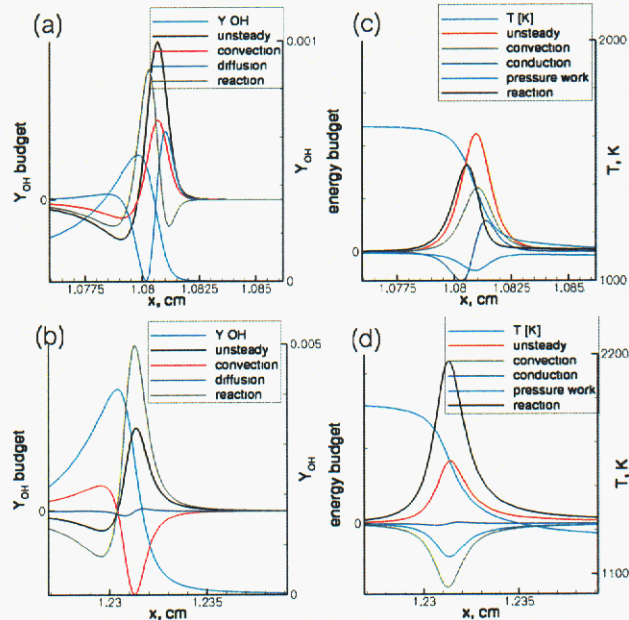


Figure 2.2.4. Terms in the instantaneous OH species bud-get for (a) case C (1.2 ms), (b) case A (0.77 ms), and thermal energy budget for (c) case C, (d) case A.

## 2.2.4 Analysis

It is possible to obtain relatively simple estimates of the rate of heat release, or equivalently the rate of reaction front propagation. As described by Zel'dovich [9], there are at least three modes of propagation: a deflagration, ignition front propagation and detonation. The analysis in the present section will consider only the ignition propagation mode. For cases where ignition propagation is found to be slow relative to deflagration or fast relative to the sound speed, it is presumed that other ignition modes will predominate. To determine the rate of ignition propagation, this analysis was conducted for constant-volume vessels with single-step chemistry. Space limitations prevent the full



exposition of this analysis here, although this will be given elsewhere [12]; this analysis is analogous to that provided by Linan and Williams [13]. It is noted here that the analysis ignores any laminar flame propagation, makes the low-Mach number assumption of rapid pressure equalization throughout the domain as well as other typical assumptions like constant properties.

The key results of the analysis are that the ignition of a given reactant fluid element can be determined by the progress of a variable that couples time advance with compression heating. This provides the necessary feedback from whence cooler or less-reactive mixtures are compression heated to ignition sooner than they would otherwise have ignited in a constant pressure environment. This progress variable, denoted  $\sigma$  is defined as

$$\sigma = \int_0^t \delta \exp[(\gamma-1)\bar{s}] dt$$

where  $\delta$  is a suitably defined Damköhler number,  $\gamma$  is the ratio of specific heats and  $\bar{s}$  is the volume average of  $s$ ,

$$s = [S(x) - S_c] T_c / S_c T_{act}$$

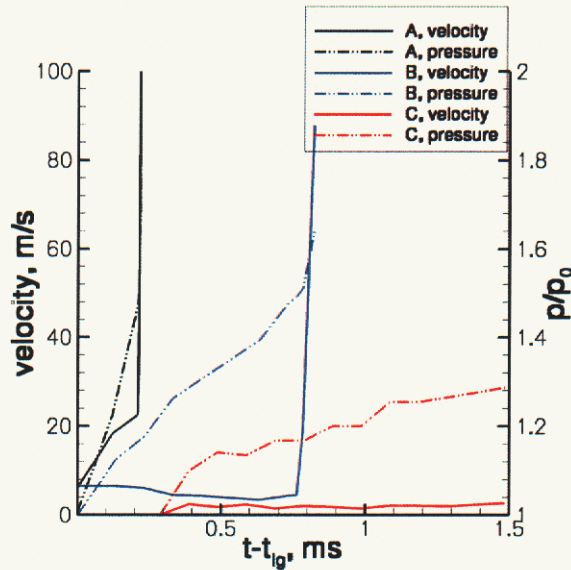


Figure 2.2.5. Ignition front velocity and pressure increase. Pressure is normalized by its initial pressure (31 atm). The ignition delay time,  $t_{ig}$ , corresponds to the location of maximum initial temperature.

$$s = [S(x) - S_c] T_c / S_c T_{act}$$

where  $S = T/P^{(\gamma-1)/\gamma}$  is an entropy-like variable that describes the reaction progress. Here the characteristic values for  $S$  and  $T$  before ignition are  $S_c$  and  $T_c$ , and  $T_{act}$  is the effective activation energy of the system. It is  $\bar{s}$  that accounts for the effect of compression in making mixtures ignite earlier. It can be shown that ignition occurs for a fixed value of  $\sigma Y(x) \exp(s(x))$ , where  $Y(x)$  and  $s(x)$  represent the variation of reactant mass fraction and

temperature throughout the domain; that fixed value is unity for a suitably defined Damköhler number.

This system can be evolved forward in time (or in  $\sigma$ ) to give the ignition time for each fluid element in a mixture. Ignition propagation is dependent on the gradient in  $Y(x)\exp(s(x))$ , which determines how far  $\sigma$  must progress before ignition of that element occurs, and the change in  $\bar{s}$  (the heat released per total volume) per unit reactant consumption that determines the rate of progress of  $\sigma$  in time. In the following paragraphs the effects of temperature gradient (or  $Y(x)\exp(s(x))$  gradient) magnitude on ignition propagation are shown followed by the effects of heat release per unit reactant consumption on ignition propagation. These serve to demonstrate the key physics present in the simplified analysis that are also observed in the DNS. Figure 2.2.6 shows the ignition evolution for conditions that correspond to cases A and B in Table 1. In Figs. 2.2.6 and 2.2.7 time is normalized by initial ignition time and velocity by initial ignition time and temperature peak half spacing (or one-quarter of the DNS domain). At the initial instant there is a sharp pressure rise and a rapid propagation of the ignition front across the very

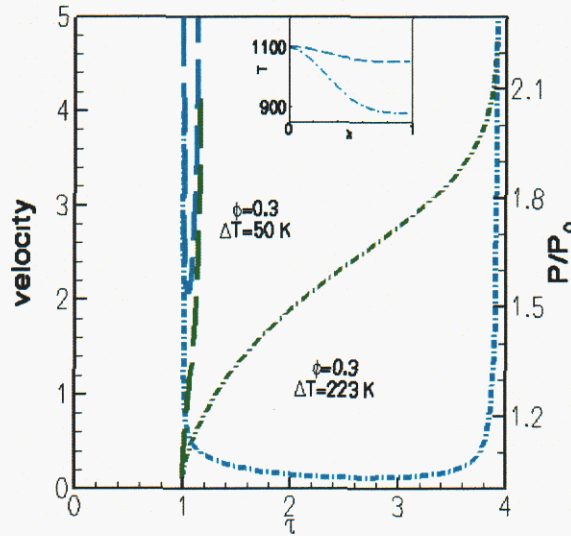


Figure 2.2.6. Ignition front evolution is indicated by the pressure evolution and the propagation velocity of the ignition front for two temperature differences over the same length scale corresponding to cases A and B.

top of the Gaussian profiles. This does not appear in the DNS results in Fig. 2.2.5 because those results show the evolution after the initial ignition. Following the initial ignition event, the rate of propagation and pressure rise are reduced while ignition propagates across the region of significant temperature gradient. During this period, the rate of propagation is proportional to the gradient of  $Y(x)\exp(s(x))$ . Larger temperature gradients in case B ( $\Delta T=223$ ) relative to case A ( $\Delta T=50$ ) result in significantly slower ignition propagation evident in Figs. 2.2.5 and 2.2.6. The temperature gradient effect on ignition propagation is magnified at the end of the evolution when the temperature gradient approaches zero and extremely high velocities are observed in both the DNS and

the analytic results. The results indicate that smaller temperature gradients lead to more rapid heat release and are more likely to lead to extremely rapid front propagation and potential development of shock waves. The dash-dot line has a greater corresponding gradient than the dashed line as indicated by the initial temperature profile in the inset.

In Fig. 2.2.7 the ignition evolution is shown for two different equivalence ratios corresponding to cases B and C in Table 2.2.1. Varying the equivalence ratio effectively varies the heat release per unit volume and thereby the degree of compression heating per unit of ignition progress; this affects the progress of  $\sigma$  through  $\bar{s}$ . Greater compression heating accelerates the ignition process for nonignited fluid elements leading to the faster ignition propagation observed at higher equivalence ratios. If this ignition propagation approaches sonic speeds, then compression waves may form into shock waves. The dependence of the ignition propagation rate on the equivalence ratio may explain the observed propensity for noisier HCCI operation at higher equivalence ratios [2].

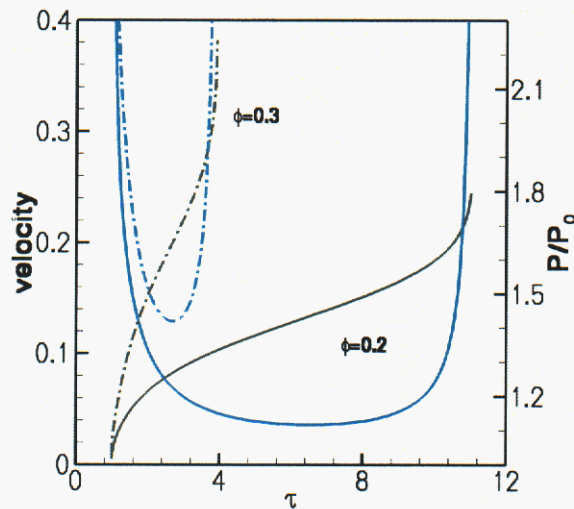


Figure 2.2.7. Ignition evolution is shown for two different equivalence ratios corresponding to cases B and C.

### 2.2.5 Conclusions

This study considers the autoignition of a premixed lean hydrogen/air mixture at elevated pressures in the presence of temperature inhomogeneities. The model problem studied by one-dimensional DNS and theoretical analysis corresponds to the autoignition of two hot spots in a closed domain and subsequent ignition front propagation. Several modes of ignition front propagation were identified. For larger temperature gradients and less reactive mixtures, laminar deflagration dominates the front propagation. For smaller temperature gradients (or more precisely the gradient of reactants and the exponential of the temperature divided by the effective activation energy) and for greater heat release per unit volume, ignition fronts propagate more rapidly. Depending upon how energetic the mixture is and the initial temperature gradient across the hot spot, combustion heat release-pressure feedback can result in the coalescence of the ignition waves with compression waves as the ignition front propagation approaches sonic velocities, resulting, in some instances, in the formation of developing shock waves from a subsonic ignition propagation.



## References

1. Epping, K., Aceves, S., Bechtold, R., and Dec, J., *SAE Technical Paper* 2002-01-1923.
2. Bradley, D., Morley, C., Gu, X. J., and Emerson, D. R., *SAE Technical Paper* 2002-01-2868.
3. Hultqvist, A., Christenson, M., Johansson, B., Richter, M., Nygren, J., Hult, J., and Alden, M., *SAE Technical Paper* 2002-01-0424.
4. Kennedy, and C.K., Carpenter, M.H., *Applied Numerical Mathematics* **14**: 397-433 (1994).
5. Kennedy, C.K., Carpenter, M.H., and Lewis, R.M., *Applied Numerical Mathematics* **35**: 177-219 (2000).
6. Poinso, T., and Lele, S. *J. Comput. Phys.* **101**: 1 (1991).
7. Smooke, M. D. and Giovangigli, V. (M. D. Smooke, Ed.), *Lecture Notes in Physics* **384**, p. 1-28, Springer-Verlag, New York, 1991.
8. Yetter, R.A., Dryer, F.L., and Rabitz, H., *Combust. Sci. Tech.* **79**: 97-128 (1991).
9. Zel'dovich, Y. B., *Combust. Flame* **39**: 211-214 (1980).
10. Lewis, B., von Elbe, G., *Combustion, Flames and Explosions of Gases*, Academic Press, New York (1987).
11. Makhviladze, G. M. and Rogatykh, D. I., *Combust. Flame* **87**: 347-356 (1991).
12. Hewson, J. C., Chen, J. H., Mason, S. D., in preparation, 2003.
13. Liñán, A., Williams, F. A., *Comb. Sci. Tech.*, **105**:245-263 (1995).

## 2.3 Large Eddy Simulation

### 2.3.1 Introduction

Local instantaneous flow-conditions and mixture-states in HCCI engines can be dominated by the geometric features of the port, valve and cylinder arrangement. These features, coupled with wall cooling and the periodic motion of the piston, can induce highly turbulent, three-dimensional, recirculating flow and scalar-mixing. The resultant cascade of strongly coupled processes can impose significant inhomogeneities over a wide range of time and length scales. Such inhomogeneities can play a major role with respect to in-cylinder ignition characteristics, the resultant combustion processes, and subsequent control strategies.

From the numerical perspective, studying the effects of in-cylinder processes in more general terms requires a fully-coupled three-dimensional treatment of the key thermo-physical processes and cylinder geometry over full engine cycles. There are currently three basic choices with regard to the simulation approach. The widely used Reynolds-Averaged Navier-Stokes (RANS) approximation, Large Eddy Simulation (LES), and Direct Numerical Simulation (DNS). The least numerically intensive is RANS. For this approach, all turbulent motions are modeled, the closure is empirical, and predictions are highly sensitive to models and model constants. LES is a much more numerically intensive methodology, but offers a higher degree of accuracy in return. For this approach, the large energetic scales are resolved and the subgrid-scales are modeled. In contrast to RANS, LES closures are time-accurate, the models tend to be more universal, and it is not necessary to adjust constants for every flow. With the appropriate grid constraints in place, the use of dynamic modeling eliminates the need for any model constants. The enhanced accuracy, however, comes with a much stricter set of algorithmic and computational requirements. DNS is the most numerically intensive. For this approach, all scales are resolved, and no modeling is required, but the method is severely CPU limited. Thus, it cannot be used to simulate the full range of relevant scales and is confined only to analysis of the smallest scales in a flow.

The selection of RANS versus LES versus DNS as a solution method revolves around: 1) the time required to get a solution, 2) the accuracy of a solution, and 3) the feasibility of obtaining a solution. DNS of full engine geometries is clearly not feasible at this point in time. Improvements in computational speed and capacity over the past several years, however, has made the application of LES feasible for increasingly complex flows. This method has now been used successfully as both a complementary tool for understanding turbulence and for modeling the effects of turbulence in a variety of engineering applications. With the advent of massively parallel computer hardware, LES now provides a means to study coupled combustion, transport and multiphase processes in parameter spaces that are unattainable using DNS, with a degree of fidelity that is far more accurate than RANS calculations. It is important to point out, however, that the LES calculations are still “grand-challenge” in nature and require significant labor and computational resources.

Here a preliminary effort in the area of LES (added midway through the project) was undertaken to develop a unique interdisciplinary approach that compliments the existing DNS, ODT and experimental efforts at CRF. The objectives were twofold. The first was

to establish a baseline capability directly linked to the ongoing experimental effort. The second was to provide some initial insights regarding the phenomenological conditions inside HCCI engines. Calculations were focused on the CRF HCCI Experimental Research Engine [1, 2] using an idealized port, valve and cylinder configuration with the same bore, stroke, piston contours and operating conditions. The calculations were performed using an existing massively parallel software framework and described below. This framework handles a fully coupled implementation of the governing conservation equations with a general treatment of the equation of state, thermodynamics, transport processes and finite-rate chemical kinetics. It has been validated for a wide variety of flows and includes a time dependent mesh movement capability that is used to simulate the moving piston.

## 2.3.2 Theoretical–Numerical Framework

### Baseline Formulation

The results shown in subsequent sections were obtained using the theoretical-numerical framework developed by Oefelein [3, 4]. The numerical framework solves the fully coupled conservation equations of mass, momentum, total-energy and species. These equations can be expressed in conservative form as follows:

- Mass:

$$\frac{\partial \rho}{\partial t} + \nabla \cdot (\rho \mathbf{u}) = 0. \quad (2.3.1)$$

- Momentum:

$$\frac{\partial}{\partial t}(\rho \mathbf{u}) + \nabla \cdot \left[ \rho \mathbf{u} \otimes \mathbf{u} + \frac{p}{M^2} \mathbf{I} \right] = \nabla \cdot \boldsymbol{\tau}, \quad (2.3.2)$$

where

$$\boldsymbol{\tau} = \frac{\mu}{Re} \left[ -\frac{2}{3}(\nabla \cdot \mathbf{u})\mathbf{I} + (\nabla \mathbf{u} + \nabla \mathbf{u}^T) \right]$$

represents the viscous stress tensor.

- Total Energy:

$$\frac{\partial}{\partial t}(\rho e_t) + \nabla \cdot [(\rho e_t + p)\mathbf{u}] = \nabla \cdot [\mathbf{q}_e + M^2(\boldsymbol{\tau} \cdot \mathbf{u})], \quad (2.3.3)$$

where

$$\begin{aligned} e_t &= e + \frac{M^2}{2} \mathbf{u} \cdot \mathbf{u} \\ e &= \sum_{i=1}^N h_i Y_i - \frac{p}{\rho} \\ h_i &= h_{f,i}^\circ + \int_{p^\circ}^p \int_{T^\circ}^T C_{p,i}(T, p) dT dp \end{aligned}$$

represents the total internal energy, internal energy and enthalpy of the  $i^{th}$  species, respectively, and  $\mathbf{q}_e$  the energy diffusion flux.



- Species:

$$\frac{\partial}{\partial t}(\rho Y_i) + \nabla \cdot (\rho Y_i \mathbf{u}) = \nabla \cdot \mathbf{q}_i + \dot{\omega}_i \quad i = 1, \dots, N-1, \quad (2.3.4)$$

where  $\mathbf{q}_i$  and  $\dot{\omega}_i$  represent the mass diffusion fluxes and the rate of production of the  $i^{th}$  species, respectively.

Equations (2.3.1) through (2.3.4), coupled with 1) an appropriate equation of state, 2) appropriate treatments of thermodynamic and transport properties, and 3) validated mixing and combining rules for the mixtures of interest accommodate the most general system of interest including cases when multicomponent and/or preferential diffusion processes are present. The viscous stress tensor is assumed to follow Stokes' hypothesis, and the heat release due to chemical reaction in Eq. (2.3.3) is accounted for in the description of the specific enthalpies,  $h_i$ , as given by the enthalpy of formation,  $h_{f,i}^\circ$ . The heat release rate can be represented equivalently, as a source term on the right hand side of Eq. (2.3.3), as the product of the enthalpy of formation and the local rate of production of all the species considered in the system. Using this representation, the source term and specific enthalpies are given as:

$$\dot{Q}_e = - \sum_{i=1}^N \dot{\omega}_i h_{f,i}^\circ, \text{ and} \quad (2.3.5)$$

$$h_i = \int_{p^\circ}^p \int_{T^\circ}^T C_{p,i}(T, p) dT dp. \quad (2.3.6)$$

The theoretical formulation handles a generalized treatment of the equation of state, thermodynamics, transport processes, and chemical kinetics for the full multicomponent system. The numerical formulation treats the fully compressible conservation equations, but can be evaluated in the incompressible limit. Thus, incompressibility is treated as a limiting extreme of the more general compressible equation set given above. A unique dual-time multistage scheme is employed with a generalized preconditioning methodology that optimally treats convective, diffusive, geometric, and source term anomalies in a unified manner. The spatial scheme employs a staggered methodology in generalized curvilinear coordinates. The algorithm has been optimized to provide excellent parallel scalability attributes using a multi-block domain decomposition with distributed-memory message-passing.

### Filtered Conservation Equations

For LES applications, the filtered version of Eqs. (2.3.1)–(2.3.4) are solved. These equations are given, respectively, as:

$$\frac{\partial \bar{\rho}}{\partial t} + \nabla \cdot (\bar{\rho} \tilde{\mathbf{u}}) = 0, \quad (2.3.7)$$

$$\frac{\partial}{\partial t}(\bar{\rho} \tilde{\mathbf{u}}) + \nabla \cdot \left[ \left( \bar{\rho} \tilde{\mathbf{u}} \otimes \tilde{\mathbf{u}} + \frac{\mathcal{P}}{M^2} \mathbf{I} \right) \right] = \nabla \cdot \vec{\mathcal{T}}, \quad (2.3.8)$$

$$\begin{aligned} \frac{\partial}{\partial t}(\bar{\rho} \tilde{e}_t) + \nabla \cdot [(\bar{\rho} \tilde{e}_t + \mathcal{P}) \tilde{\mathbf{u}}] \\ = \nabla \cdot \left[ \left( \vec{\mathcal{Q}}_e + M^2 (\vec{\mathcal{T}} \cdot \tilde{\mathbf{u}}) \right) \right] + \bar{\mathcal{Q}}_e, \end{aligned} \quad (2.3.9)$$

$$\frac{\partial}{\partial t}(\bar{\rho} \tilde{Y}_i) + \nabla \cdot (\bar{\rho} \tilde{Y}_i \tilde{\mathbf{u}}) = \nabla \cdot \vec{\mathcal{S}}_i + \bar{\omega}_i. \quad (2.3.10)$$

The terms  $\mathcal{P}$ ,  $\vec{\mathcal{T}}$ ,  $\vec{\mathcal{Q}}_e$  and  $\vec{\mathcal{S}}_i$  represent respective composite (i.e., molecular plus *sgs*) stresses and fluxes. The terms  $\bar{\mathcal{Q}}_e$  and  $\bar{\omega}_i$  represent the filtered energy and species source terms.

### Subgrid-Scale Closure

The subgrid-scale closure is obtained using the “mixed” dynamic Smagorinsky model by combining the models proposed by Erlebacher, Hussaini, Speziale and Zang [5] and Speziale [6] with the dynamic modeling procedure [7–11]. The composite stresses and fluxes in Eqs. (2.3.7)–(2.3.10) are given as

$$\vec{\mathcal{T}} = (\mu_t + \mu) \frac{1}{Re} \left[ -\frac{2}{3} (\nabla \cdot \tilde{\mathbf{u}}) \mathbf{I} + (\nabla \tilde{\mathbf{u}} + \nabla \tilde{\mathbf{u}}^T) \right] - \bar{\rho} (\tilde{\mathbf{u}} \otimes \tilde{\mathbf{u}} - \tilde{\mathbf{u}} \otimes \tilde{\mathbf{u}}), \quad (2.3.11)$$

$$\vec{\mathcal{Q}}_e = \left( \frac{\mu_t}{Pr_t} + \frac{\mu}{Pr} \right) \frac{1}{Re} \nabla \tilde{h} + \sum_{i=1}^N \tilde{h}_i \vec{\mathcal{S}}_i - \bar{\rho} (\tilde{h} \tilde{\mathbf{u}} - \tilde{\tilde{h}} \tilde{\tilde{\mathbf{u}}}), \text{ and} \quad (2.3.12)$$

$$\vec{\mathcal{S}}_i = \left( \frac{\mu_t}{Sc_{t_i}} + \frac{\mu}{Sc_i} \right) \frac{1}{Re} \nabla \tilde{Y}_i - \bar{\rho} (\tilde{Y}_i \tilde{\mathbf{u}} - \tilde{\tilde{Y}}_i \tilde{\tilde{\mathbf{u}}}). \quad (2.3.13)$$

The term  $\mu_t$  represents the *sgs* eddy viscosity, given by

$$\mu_t = \bar{\rho} C_R \Delta^2 \Pi_{\tilde{\mathbf{S}}}^{\frac{1}{2}}, \quad (2.3.14)$$

where

$$\Pi_{\tilde{\mathbf{S}}} = \tilde{\mathbf{S}} : \tilde{\mathbf{S}}, \text{ and } \tilde{\mathbf{S}} = \frac{1}{2} (\nabla \tilde{\mathbf{u}} + \nabla \tilde{\mathbf{u}}^T). \quad (2.3.15)$$

The terms  $C_R$ ,  $Pr_t$ , and  $Sc_{t_i}$  represent the Smagorinsky, *sgs*-Prandtl and *sgs*-Schmidt numbers and are evaluated dynamically as functions of space and time. The overall model

includes the Leonard and cross-term stresses and provides a Favre averaged generalization of the Smagorinsky eddy viscosity model [12] coupled with gradient diffusion models that simulate subgrid-scale mass and energy transport processes.

### **Thermodynamic and Transport Properties**

The property evaluation scheme is designed to account for thermodynamic nonidealities and transport anomalies over a wide range of pressures and temperatures. The scheme is comprehensive and intricate, thus only a skeletal description can be given here. The extended corresponding states model [13, 14] is employed with a cubic equation of state. In past studies [15, 16] modified versions of both the Benedict-Webb-Rubin (*BWR*) equation of state and cubic equations of state have been used to evaluate the  $p$ - $v$ - $T$  behavior of dense multicomponent mixtures. Use of modified *BWR* equations of state in conjunction with the extended corresponding states principle has been shown to provide consistently accurate results over the widest range of pressures, temperatures and mixture states, especially at near-critical conditions. A major disadvantage of *BWR* equations, however, is that they are not computationally efficient.

Cubic equations of state can be less accurate, especially for mixtures at near-critical or saturated conditions, but are computationally efficient. Experience has shown that both the Soave-Redlich-Kwong (*SRK*) and Peng-Robinson (*PR*) equations, when used in conjunction with the corresponding states principle, can give accurate results over the range of pressures, temperatures and mixture states of interest in this study. The *SRK* coefficients are fit to vapor pressure data and are thus more suitable for conditions when the reduced temperature is less than one. The *PR* coefficients, on the other hand, are more suitable for conditions when the reduced temperature is greater than one. A summary of the cubic equations of state and recommended constants is given by Reid et al. [17, Chapter 3].

Having established an analytical representation for real mixture  $p$ - $v$ - $T$  behavior, the thermodynamic properties are obtained in two steps. First, respective component properties are combined at a fixed temperature using the extended corresponding states methodology outlined above to obtain the mixture state at a given reference pressure. A pressure correction is then applied using departure functions of the form given by Reid et al. [17, Chapter 5]. These functions are exact relations derived using the Maxwell relations (see VanWylen and Sonntag [18, Chapter 10], for example) and make full use of the real mixture  $p$ - $v$ - $T$  path dependencies dictated by the equation of state. Standard state properties are obtained using the databases developed by Gordon and McBride [19] and Kee et al. [20]. Chemical potentials and fugacity coefficients are obtained in a manner similar to that outlined above.

Molecular transport properties are evaluated in a manner analogous to the thermodynamic properties. Viscosity and thermal conductivity are obtained using the extended corresponding states methodologies developed by Ely and Hanley [21, 22]. The mass diffusion coefficients and thermal diffusion coefficients are obtained using the methodologies outlined by Bird et al. [23] and Hirschfelder et al. [24] in conjunction with the corresponding states methodology proposed by Takahashi [25].



## Chemical Kinetics and Source Term Closure

To synchronize the LES framework with the DNS, finite-rate hydrogen-oxygen kinetics are considered using the nine species ( $H_2$ ,  $O_2$ ,  $OH$ ,  $H_2O$ ,  $H$ ,  $O$ ,  $HO_2$ ,  $H_2O_2$ ,  $N_2$ ), 19-step mechanism developed by Westbrook and Dryer [26] and Yetter et al. [27]. Combustion processes were assumed to be distributed in the current calculations. Detailed combustion models are currently being evaluated under other projects and can be incorporated transparently as the current HCCI effort evolves.

### 2.3.3 Computational Domain

#### CRF Experimental HCCI Engine

The computational domain is designed to generically match the CRF experimental HCCI engine configuration [1, 2]. This engine is derived from a Cummins B-series (medium-duty) production diesel engine. The research engine is equipped with both a GDI fuel injector and a fully premixed fueling system.

The calculations performed as part of the current project were conducted using a simplified geometry. A piston and cylinder configuration with the same bore, stroke, piston contours and operating conditions, as specified for the experimental engine, was employed. The actual port and valve configuration, however, has been replaced with an idealized port and valve centered axisymmetrically on the top of the cylinder.

The baseline grid topology is given in Fig. 2.3.1. Here only half of the grid is shown to highlight the inner structure at the mid-plane of the cylinder. Generalized curvilinear coordinates are employed with a general distributed multi-block domain decomposition. The current grid consists of 192 blocks, with  $16^3$  cells per block. The computational domain has been nondimensionalized using a reference length scale of  $\delta = 32 \text{ mm}$ , which is the physical diameter of the valve head.

Key geometric specifications are given in Table 2.3.1. The engine has a bore of  $102 \text{ mm}$ , a stroke of  $120 \text{ mm}$  and a connecting rod length of  $192 \text{ mm}$ . A custom HCCI piston is employed with a swepted spherical bowl and a head clearance of  $6 \text{ mm}$ . The overall configuration produces a geometric compression ratio of 18:1. The valve stem diameter is  $8 \text{ mm}$  and the valve seat angle is  $60^\circ$ .

The valve in the current configuration is fixed and a small annular gap is used to allow flow past the valve during the intake stroke. The annular gap is sealed during the compression stroke. This gap has been sized to provide approximately the same flow area across the valve as is present in the actual research engine. Effects associated with the piston crevice are not considered at this time.

#### Time-Varying Grid Configuration

The piston in the research engine is externally motored and fitted with an over-sized flywheel to minimize rotational speed variations during single-cylinder operation. This situation is handled numerically by using time dependent curvilinear metrics in the base LES flow solver. With this infrastructure in place, the three-dimensional multi-block mesh

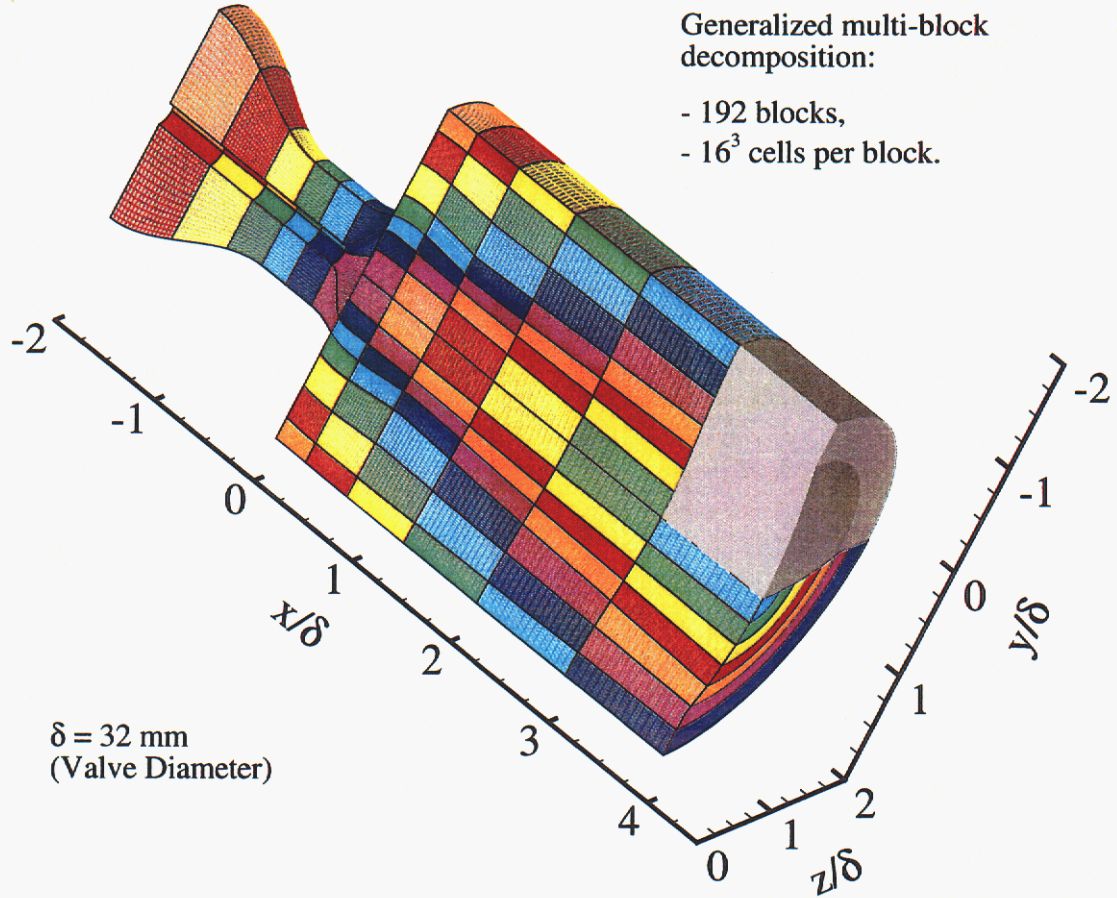


Figure 2.3.1: Baseline curvilinear grid configuration.

Table 2.3.1: Engine geometric specifications.

Bore, $B$ .....	102 mm
Stroke, $L$ .....	120 mm
Connecting Rod Length, $l$ .....	192 mm
Crank Shaft Radius, $a$ .....	60 mm
Head Clearance, $c$ .....	6 mm
Geometric Compression Ratio, $r_c$	18:1
Piston Bowl Sweep Radius, $R_b$ ..	194 mm
Piston Bowl Depth, $d$ .....	3.78 mm
Valve Head Diameter, $d_v$ .....	32 mm
Valve Stem Diameter, $d_s$ .....	8 mm
Valve Seat Angle, $\alpha$ .....	60°



associated with the cylinder is compressed and expanded according to the relations given by Heywood [28]. The position of the piston crown is governed by the expression:

$$s = c \left\{ 1 + \frac{1}{2}(r_c - 1)[1 - \cos \theta + R - (R^2 - \sin^2 \theta)^{\frac{1}{2}}] \right\}, \quad (2.3.16)$$

where (as per the nomenclature given in Table 2.3.1)  $c$  is the head clearance,  $r_c$  the compression ratio,  $\theta$  the crank angle, and  $R = l/a$  the ratio of the connecting rod length to crank radius. The corresponding instantaneous piston velocity is given by:

$$\frac{ds}{dt} = c \left\{ \frac{1}{2}(r_c - 1) \sin \theta \frac{d\theta}{dt} \left[ 1 + \frac{\cos \theta}{(R^2 - \sin^2 \theta)^{\frac{1}{2}}} \right] \right\}. \quad (2.3.17)$$

The piston velocity is zero at the beginning of each stroke, reaches a maximum near the middle of each stroke, and decreases to zero at the end of the stroke. Note that piston speeds are usually limited within the range of 8 to 15  $m/s$  due to gas flow resistance and stresses associated with the inertia of the moving parts.

The mesh associated with respective blocks is moved dynamically in a time accurate manner as a function of Eqs. (2.3.16) and (2.3.17). The time dependent grid coordinates and metrics are evolved proportionately in the axial direction to produce fully synchronized linear harmonic compression and expansion of the grid. Respective numerical fluxes are corrected accordingly in a manner consistent with the curvilinear transformation. A schematic diagram of the time-varying computational domain is given in Fig. 2.3.2. The piston is at top-dead-center (TDC) when  $\theta = 0^\circ$  on the compression stroke.

### 2.3.4 Results and Discussion

A series of canonical case studies were performed with three primary goals. The first was to synchronize the distinctly different numerical algorithms and model packages used in the LES and DNS frameworks to insure consistency between results. The second was to investigate the accuracy and sensitivity of various thermodynamic and transport processes relative to Senkin [29, 30] and the DNS code (S3D). The third was to begin to characterize the full multidimensional turbulence and scalar mixing processes that occur inside the idealized port-valve-cylinder configuration over full engine cycles. At this stage, the primary objective was to establish a foundational capability to perform high-fidelity simulations in full engine geometries.

The baseline operating conditions and reference state for the cases considered are given in Table 2.3.2. For each case considered, an intake pressure of 120  $kPa$  and intake temperature of 423  $K$  is specified. The crankshaft speed is 1200  $rpm$ , which yields a peak piston velocity of 7.54  $m/s$ . The reference state used for nondimensionalization of the governing equations is based on the intake pressure and temperature, which yields a reference density of 0.956  $kg/m^3$ , a reference viscosity of  $23.5 \times 10^{-6} Pa \cdot s$  and a reference specific heat of 1050  $J/kg \cdot K$ .



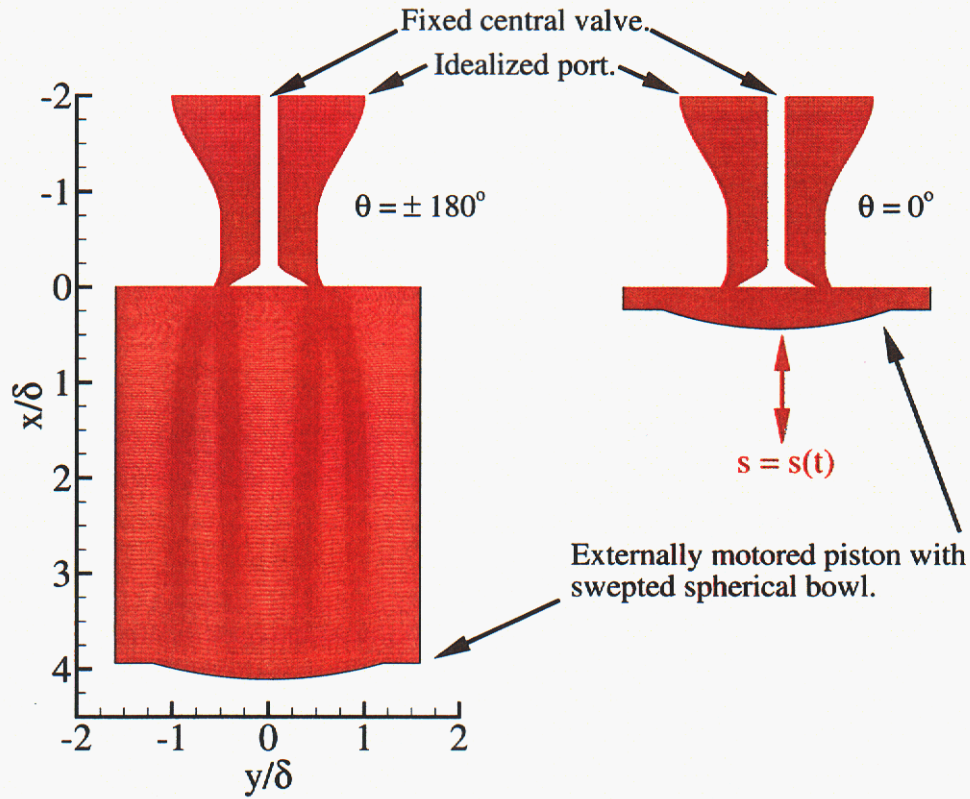


Figure 2.3.2: Schematic diagram of time-varying computational domain ( $\theta = 0^\circ$  is taken to be TDC on the compression stroke).

Table 2.3.2: Operating conditions and reference state.

**Operating Conditions:**

Intake Pressure .....	120 kPa
Intake Temperature .....	423 K
Cylinder Wall Temperature ....	373 K
Crankshaft Speed .....	1200 rpm
Reference (Peak) Velocity .....	7.54 m/s

**Reference State (Air):**

Pressure .....	120 kPa
Temperature .....	423 K
Density .....	0.956 kg/m <sup>3</sup>
Dynamic Viscosity .....	$23.5 \times 10^{-6} \text{ Pa} \cdot \text{s}$
Constant Pressure Specific Heat	1050 J/kg · K

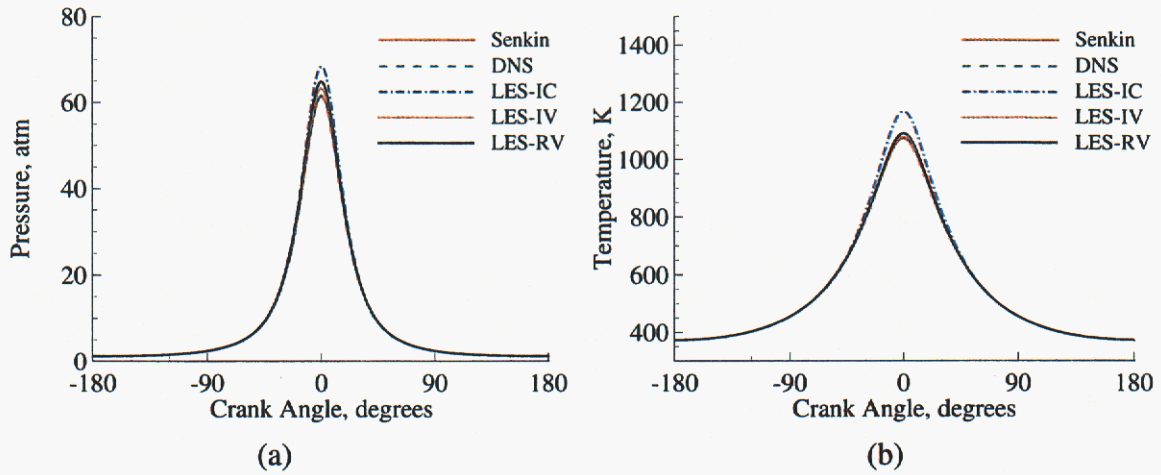


Figure 2.3.3: Isentropic compression-heating of air using modified versions of Senkin and the DNS (S3D) code; and the LES solver with a time-varying grid. The initial conditions correspond to those given in Table 2.3.2,  $r_c = 18:1$  (IC = Ideal Gas, Constant Properties, IV = Ideal Gas, Variable Properties, RV = Real Gas, Variable Properties).

### Compression Heating

A series of compression-heating studies were performed to insure that the numerical algorithms and models used to evaluate the thermo-physical properties performed accurately and consistently between respective codes. The one-dimensional Senkin program [29, 30] was used to provide an independent baseline. Both the Senkin and the DNS S3D codes were modified by adding source terms to the governing conservation equations to simulate the effects of compression (i.e., compression heating was induced analytically, not numerically by compressing the computational domain). The LES code employed the moving mesh framework described in the previous section. Respective cases were run over one compression and expansion stroke, starting at  $\theta = -180^\circ$  with a quiescent charge, compressed to TDC, then expanded back to  $\theta = 180^\circ$ .

Representative results for a compression ratio of 18:1 are shown in Fig. 2.3.3. Here the pressure (Fig. 2.3.3a) and temperature (Fig. 2.3.3b) are given as a function of crank angle over the range from  $-180^\circ$  to  $180^\circ$ . The LES was run with three different assumptions: ideal gas with constant properties, ideal gas with variable properties, and real gas with variable properties using the property evaluation scheme described above. The Senkin and DNS S3D code were run assuming an ideal gas with variable properties only. For the conditions cited, the assumption of an ideal gas with constant properties matched predictions given by the analytic isentropic relations by less than 1 percent. The assumption of an ideal gas with variable properties resulted in under predictions of approximately 4 percent, with all three codes in agreement to within 1 percent. Accounting for real gas effects produced no noticeable change, as expected. The introduction of non-isentropic loss mechanisms, however, produced deviations on the order of 10 percent between predictions based on real and ideal gases.

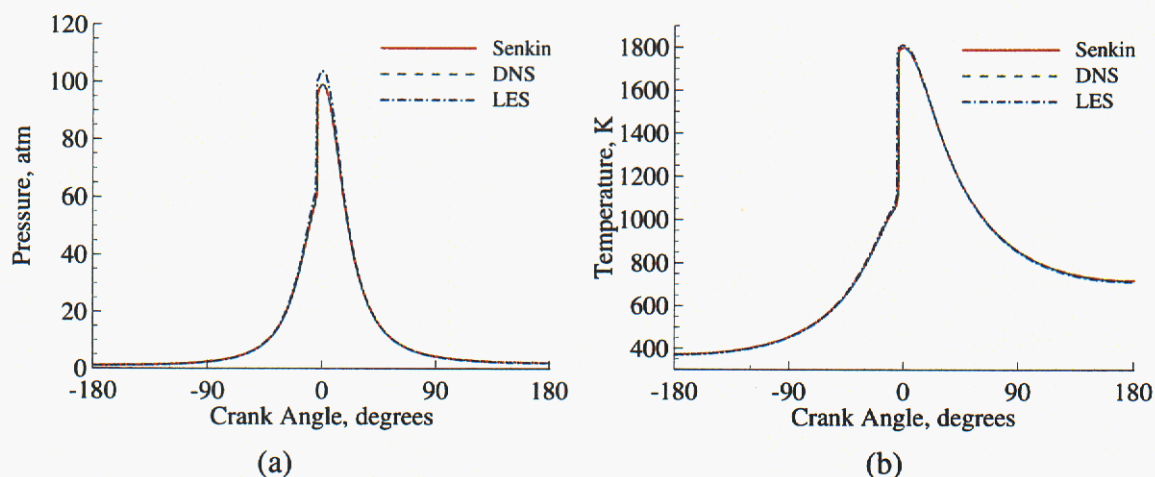


Figure 2.3.4: Compression-ignition of a homogeneous charge of hydrogen and air at an equivalence ratio of 0.2 using modified versions of Senkin and the DNS (S3D) code; and the LES solver with a time-varying grid. The initial conditions correspond to those given in Table 2.3.2.

### Compression Ignition

To further synchronize the numerical frameworks and models, a series of compression-ignition studies were conducted using the same hydrogen-oxygen kinetics mechanism [26, 27] in all three codes. The studies were conducted in a manner identical to the compression-heating study using a homogeneous charge of hydrogen and air with an equivalence ratio of 0.2. Here, the mixture was assumed to be an ideal gas with variable properties.

Representative results for a compression ratio of 18:1 are shown in Fig. 2.3.4. As in Fig. 2.3.3, plots of pressure and temperature are given as a function of crank angle over one compression and expansion stroke. In all cases considered the Senkin, DNS, and LES results associated with 1) the onset of ignition, 2) peak pressures and temperatures, and 3) expansion pressures and temperatures agreed to well within a few percent.

The collective results of these studies have provided a validated benchmark for implementation of the unique interdisciplinary approach described in the introduction of this report, where respective LES, DNS and ODT capabilities are used in a complimentary manner to study HCCI mixing and combustion processes over the full range of relevant time and length scales.

### Preliminary Cold-Flow Engine Cycle Analysis

After the initial synchronization and validation exercise was complete, attention was focused on the unique complimentary capabilities of each tool. The LES was employed to begin analyzing the larger resolved-scale multi-dimensional processes inherently missing from the DNS and ODT analysis. The long-term goal is to characterize the full multidimensional turbulence and scalar mixing processes that occur inside HCCI engines over full engine cycles. Here, a preliminary effort was undertaken using the geometric configuration



and conditions depicted by Figs. 2.3.1 and 2.3.2 and Tables 2.3.1 and 2.3.2. Only cold flow analysis was considered at this stage due to the cost, level of effort, and resources required. Parametric studies were directly coupled with the envelope of conditions considered experimentally.

Initial simulations were performed to illustrate the potentially inhomogeneous nature of in-cylinder scalar mixing processes in HCCI engines. Turbulent, unsteady, fully three-dimensional fluid dynamic and heat transfer processes were considered over one intake and compression stroke. The intake temperature and initial gas temperature in the cylinder was 423 K. The wall temperature was fixed at 373 K. Representative results are given in Figs. 2.3.5 and 2.3.6, which shows the temporal evolution of the temperature field as a function of crank angle. In a manner consistent with the previous results shown, the intake stroke is defined over the interval  $-360 < \theta < -180$  (Fig. 2.3.5) and the compression stroke is defined over the interval  $-180 < \theta < 0$  (Fig. 2.3.6).

Qualitative analysis of Figs. 2.3.5 and 2.3.6 highlight the complex nature of the flow. At  $\theta = -360^\circ$  the piston begins to draw air in from the intake manifold. The fluid moves across the annular gap between the central valve and the cylinder head. This generates a high speed jet that impinges on the side wall and eventually separates due to viscous effects. The toroidal vortex is cooled in the vicinity of the wall and the cooler fluid is then transported back into the core region away from the wall. At  $\theta = -250^\circ$ , the piston reaches its highest velocity, which induces a corresponding peak in the velocity of the intake jet. From mass conservation, the intake jet approaches flow speeds on the order of 10 times greater than the piston speed. At crank angles greater than  $-250^\circ$ , the flow is dominated by a toroidal vortex that grows in size as the piston moves down.

The interaction of the intake jet with the horizontal and vertical walls generates a variety of smaller structures that become markedly visible at  $\theta = -270^\circ$ . Later, as the piston speed decreases, the jet does not have enough momentum to penetrate the flow and begins to generate structures that remain localized in the vicinity of the valve. Large and small scale vortex interactions produce complex flow and scalar mixing throughout the cylinder. The flow structures present at the end of the intake stroke at a crank angle of  $\theta = -180^\circ$  are shown in Fig. 2.3.7. Here the dimensionless components of vorticity are given. Comparison of the structures in Figs. 2.3.5 and 2.3.6 with those in Fig. 2.3.7 provide a qualitative description of the dominant near-wall mixing processes.

When the piston begins the compression stroke, the annular gap between the central valve and the cylinder head is closed to simulate a shut valve. As the piston starts moving up, the flow structures are compressed and inhomogeneous compression-heating begins to occur. A secondary flow is induced due to the piston sliding action against the wall. As heating occurs, the major flow structures become smaller and begin to interact with the smaller secondary structures. These interactions serve to produce a more homogeneous temperature distribution. Beyond a crank angle of  $\theta = -45^\circ$ , further mixing is induced due to the radial flow processes facilitated by the presence of the bowl. The combined heating, compression, and small-scale mixing as the piston approaches TDC are critical from the standpoint of conditioning a premixed charge for combustion.

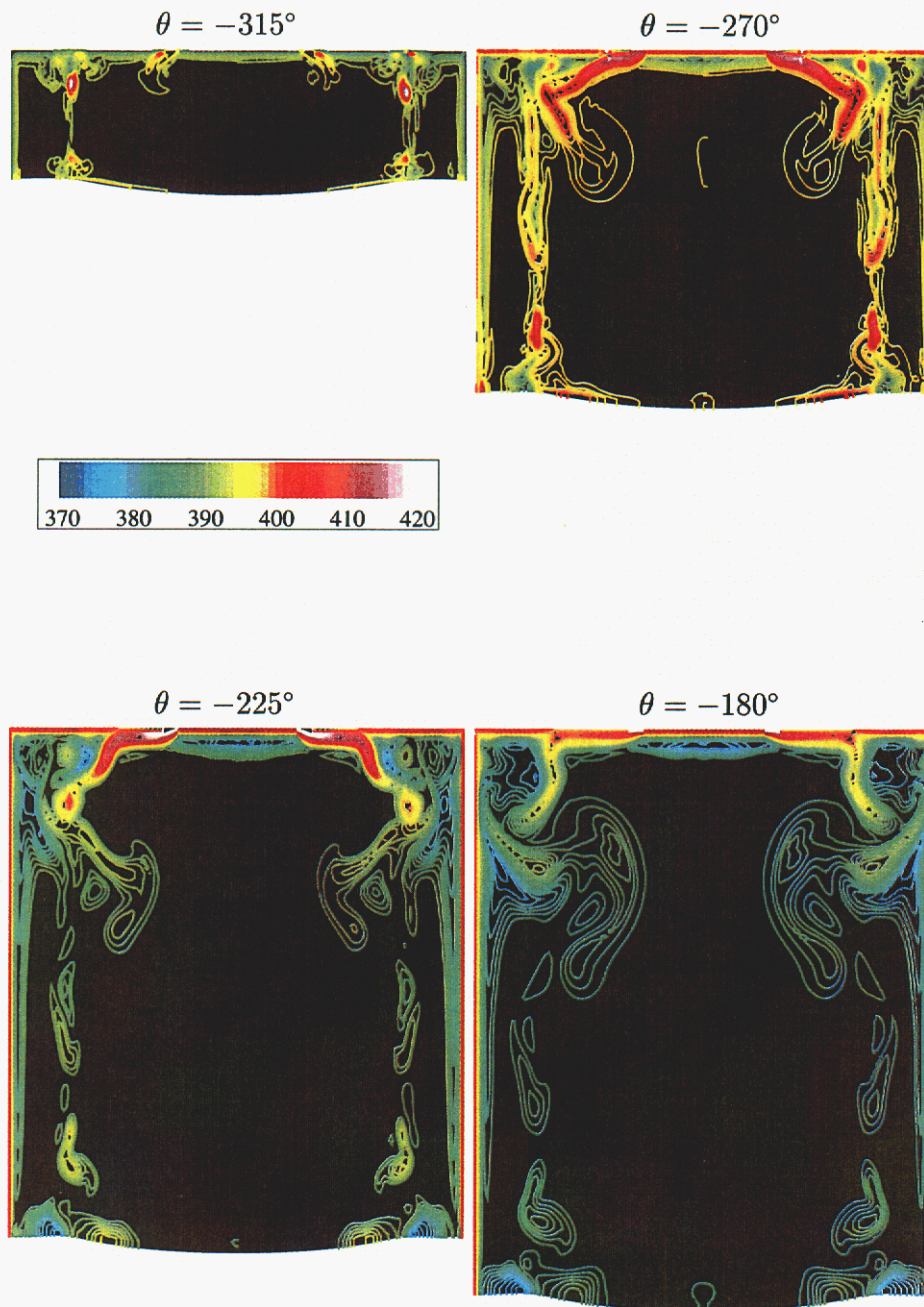


Figure 2.3.5: Temporal evolution of the temperature field as a function of crank angle during the intake stroke. The initial and boundary conditions correspond to those given in Table 2.3.2.



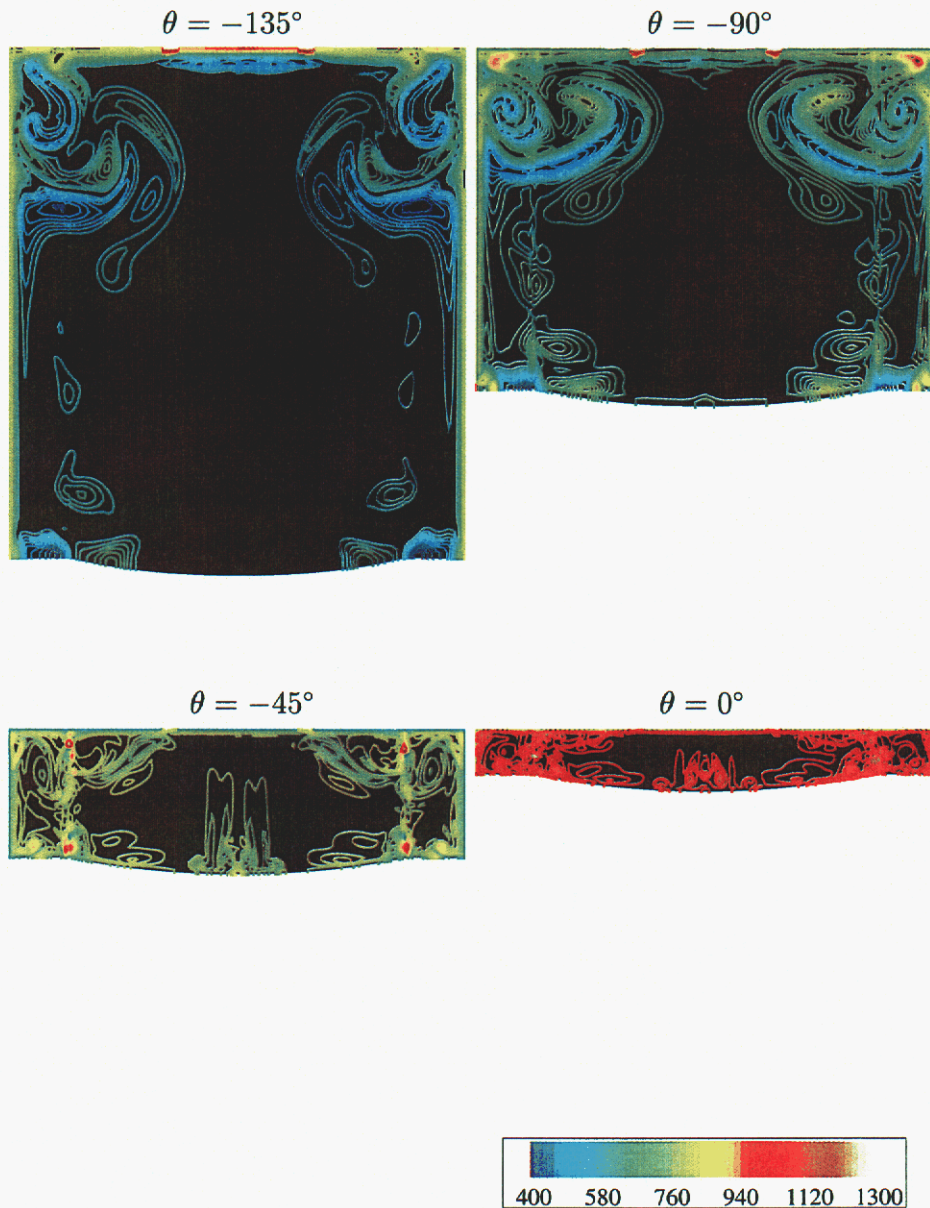


Figure 2.3.6: Temporal evolution of the temperature field as a function of crank angle during the compression stroke. The initial and boundary conditions correspond to those given in Table 2.3.2.



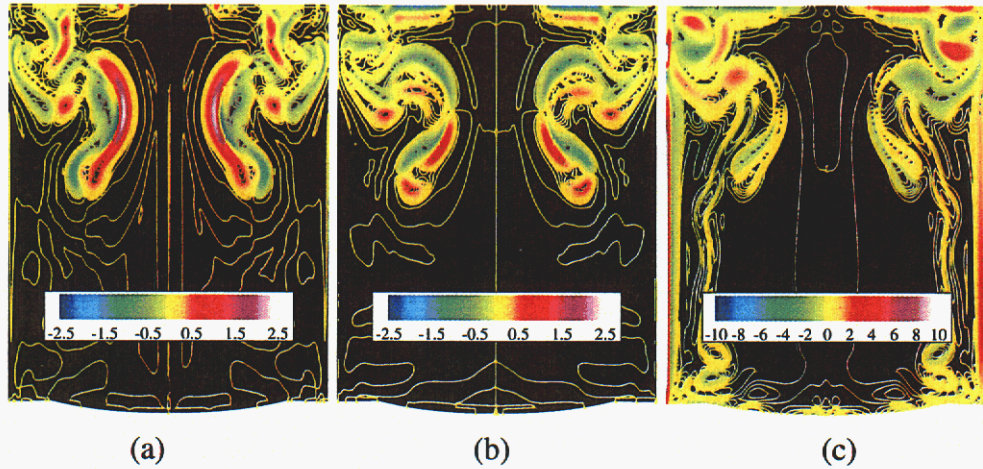


Figure 2.3.7: Dimensionless (a) axial, (b) radial, and (c) azimuthal components of vorticity at a crank angle of  $\theta = -180^\circ$ . The initial and boundary conditions correspond to those given in Table 2.3.2.

Results shown here are representative and intended to demonstrate an initial baseline capability that is directly linked to the established experimental effort. Ongoing efforts will systematically refine the calculations to increase the spatial and temporal fidelity and validated confidence levels. Sequential modifications will include consideration of flow through the piston crevice and the incorporation of a realistic valve and port configuration.

### 2.3.5 Summary

A formal effort in the area of LES has been established with focus on the CRF HCCI Experimental Research Engine. Initial calculations were conducted using an idealized port, valve and cylinder configuration with the same bore, stroke, piston contours and operating conditions specified for the experimental engine. Studies focused first on synchronizing the physics packages employed in the LES framework with the DNS framework. A series of compression-heating studies were conducted concurrently with both LES and DNS to validate respective tools using identical target cases and to gain further insight with respect to the sensitivity of the target cases to various treatments of thermodynamic and transport properties. Both ideal- and real-gas effects were considered. The compression-heating studies were followed by a companion series of compression-ignition studies to further synchronize and validate the numerical tools under reacting flow conditions.

After the initial synchronization and validation exercise was complete, attention was focused on the unique complimentary capabilities of each tool. The LES was employed to analyze the larger resolved-scale multi-dimensional processes inherently missing from the DNS and ODT analysis. The DNS and ODT capabilities were employed to study the small-unresolved subgrid-scales which must be modeled in the LES. A massively parallel case was initiated using LES to study large-scale flow features over a full engine cycle.

Only cold flow analysis was considered at this stage due to the cost, level of effort, and resources required. Results have provided preliminary insights associated with wall heat transfer processes and have facilitated the initiation of a unique interdisciplinary approach that is strongly coupled to key experimental programs at CRF and elsewhere.

## References

1. J. E. Dec. HCCI experimental research engine, In Progress. Combustion Research Facility, Sandia National Laboratories, Livermore, California.
2. J. E. Dec and Magnus Sjöberg. A parametric study of HCCI combustion – the sources of emissions at low loads and the effects of GDI fuel injection. *SAE 2003 World Congress, Paper 2003-01-0752*, March 3-6 2003. Detroit, Michigan.
3. J. C. Oefelein. General numerical framework for reacting multiphase flow with complex thermochemistry, thermodynamics and transport. Copyright 1992-2003 by J. C. Oefelein, All Rights Reserved, 2003.
4. J. C. Oefelein. General package for evaluation of multicomponent gas-liquid mixture states at all pressures. Copyright 1992-2003 by J. C. Oefelein, All Rights Reserved, 2003.
5. G. Erlebacher, M. Y. Hussaini, C. G. Speziale, and T. A. Zang. Toward the large eddy simulation of compressible turbulent flows. *Journal of Fluid Mechanics*, 238:155–185, 1992.
6. C. G. Speziale. Galilean invariance of subgrid-scale stress models in the large eddy simulation of turbulence. *Journal of Fluid Mechanics*, 156:55–62, 1985.
7. M. Germano, U. Piomelli, P. Moin, and W. H. Cabot. A dynamic subgrid-scale eddy viscosity model. *Physics of Fluids*, 3(7):1760–1765, 1991.
8. P. Moin, K. Squires, W. Cabot, and S. Lee. A dynamic subgrid-scale model for compressible turbulence and scalar transport. *Physics of Fluids*, 3(11):2746–2757, 1991.
9. D. K. Lilly. A proposed modification of the germano subgrid-scale closure method. *Physics of Fluids*, 3(11):633–635, 1992.
10. Y. Zang, R. L. Street, and J. R. Koseff. A dynamic mixed subgrid-scale model and its application to turbulent recirculating flows. *Physics of Fluids*, 5(12):3186–3195, 1993.
11. B. Vreman, B. Geurts, and H. Kuerten. On the formulation of the dynamic mixed subgrid-scale model. *Physics of Fluids*, 6(12):4057–4059, 1994.
12. J. Smagorinsky. General circulation experiments with the primitive equations. I. The basic experiment. *Monthly Weather Review*, 91:99–164, 1963.



13. T. W. Leland and P. S. Chappellear. The corresponding states principle. A review of current theory and practice. *Industrial and Engineering Chemistry Fundamentals*, 60(7):15–43, 1968.
14. J. S. Rowlinson and I. D. Watson. The prediction of the thermodynamic properties of fluids and fluid mixtures—I. The principle of corresponding states and its extensions. *Chemical Engineering Science*, 24(8):1565–1574, 1969.
15. J. C. Oefelein. *Simulation and Analysis of Turbulent Multiphase Combustion Processes at High Pressures*. PhD thesis, The Pennsylvania State University, University Park, Pennsylvania, May 1997.
16. J. C. Oefelein and V. Yang. Modeling high-pressure mixing and combustion processes in liquid rocket engines. *Journal of Propulsion and Power*, 14(5):843–857, 1998.
17. R. C. Reid, J. M. Prausnitz, and B. E. Polling. *The Properties of Liquids and Gases*. McGraw-Hill, New York, New York, 4th edition, 1987.
18. G. J. VanWylen and R. E. Sonntag. *Fundamentals of Classical Thermodynamics*. John Wiley and Sons, Incorporated, New York, New York, 3rd edition, 1986.
19. S. Gordon and B. J. McBride. Computer program for calculation of complex chemical equilibrium compositions, rocket performance, incident and reflected shocks and Chapman-Jouguet detonations. Technical Report NASA SP-273, National Aeronautics and Space Administration, 1971.
20. R. J. Kee, F. M. Rupley, and J. A. Miller. Chemkin thermodynamic data base. Technical Report SAND87-8215B, Sandia National Laboratories, 1990. Supersedes SAND87-8215 dated April 1987.
21. J. F. Ely and H. J. M. Hanley. Prediction of transport properties. 1. Viscosity of fluids and mixtures. *Industrial and Engineering Chemistry Fundamentals*, 20(4):323–332, 1981.
22. J. F. Ely and H. J. M. Hanley. Prediction of transport properties. 2. Thermal conductivity of pure fluids and mixtures. *Industrial and Engineering Chemistry Fundamentals*, 22(1):90–97, 1981.
23. R. B. Bird, W. E. Stewart, and E. N. Lightfoot. *Transport Phenomena*. John Wiley and Sons, Incorporated, New York, New York, 1960.
24. J. O. Hirschfelder, C. F. Curtiss, and R. B. Bird. *Molecular Theory of Gases and Liquids*. John Wiley and Sons, Incorporated, New York, New York, 2nd edition, 1964.
25. S. Takahashi. Preparation of a generalized chart for the diffusion coefficients of gases at high pressures. *Journal of Chemical Engineering of Japan*, 7(6):417–420, 1974.



26. C. K. Westbrook and F. L. Dryer. Chemical kinetics modeling of hydrocarbon combustion. *Progress in Energy and Combustion Science*, 10(1):1–57, 1984.
27. R. A. Yetter, F. L. Dryer, and H. Rabitz. A comprehensive reaction mechanism for carbon monoxide/hydrogen/oxygen kinetics. *Combustion Science and Technology*, 79: 97–128, 1991.
28. J. B. Heywood. *Internal Combustion Engine Fundamentals*. McGraw-Hill, New York, New York, 1988.
29. R. J. Kee, F. M. Rupley, E. Meeks, and J. A. Miller. Chemkin-III: A fortran chemical kinetics package for the analysis of gas-phase chemical and plasma kinetics. Technical Report SAND96-8216, Sandia National Laboratories, 1996.
30. R. J. Kee, F. M. Rupley, J. A. Miller, M. E. Coltrin, J. F. Grcar, E. Meeks, H. K. Moffat, A. E. Lutz, G. Dixon-Lewis, M. D. Smooke, J. Warnatz, G. H. Evans, R. S. Larson, R. E. Mitchell, L. R. Petzold, W. C. Reynolds, M. Caracotsios, W. E. Stewart, P. Glarborg, C. Wang, and O. Adigun. Chemkin collection, release 3.6. Reaction Design Incorporated, San Diego, California, 2000.

## A Additive Runge-Kutta Schemes for Convection - Diffusion - Reaction Equations

### A.1 Introduction

It is oftentimes useful to consider the compressible Navier-Stokes equations (NSE) as evolution equations with several driving forces, each having somewhat different characteristics. Typically, one distinguishes among terms such as convection, diffusion, and reaction. As such, one often considers the more tractable convection-diffusion-reaction (CDR) equations as a prologue to the full compressible NSE.[34] In the search for ever more efficient integrators, it is intuitively appealing to seek individual integration methods that are ideally suited for specific parts of the governing equations. The individual methods are then rolled into a single composite method that, ideally, would be more efficient than any individual method applied to the full computation. To accomplish this, one may consider partitioned methods. Schemes constructed to take advantage of termwise partitioning of the CDR for integration purposes may be called additive methods.[49] Partitioning of the discretized form of the equations may also be performed on an equationwise or pointwise basis.[24] There are many different partitioning strategies.[72] Runge-Kutta methods, with their extensive theoretical foundation, allow for straightforward design and construction of stable, high-order, partitioned methods composed of arbitrary numbers of elemental Runge-Kutta schemes. In addition, they also allow for the direct control of partitioning (splitting or coupling) errors.[48] Direct numerical simulation (DNS) and large-eddy simulation (LES) of fluid phenomena, with their relatively strict error tolerances, are prime candidates for such methods. The need for these strategies is by no means limited to Navier-Stokes applications.[7, 19, 55, 69]

From a termwise point of view, a linearization of one-dimensional CDR equations can provide insight into the distinguishing characteristics of each term. Upon method-of-lines discretization using high-order, finite-difference techniques, the CDR equations may be written as a system of ordinary differential equations (ODEs) and analyzed with

$$\frac{dU}{dt} = \lambda^C U + \lambda^D U + \lambda^R U, \quad (\text{A1})$$

where  $z^C = \lambda^C(\Delta t)$ ,  $z^D = \lambda^D(\Delta t)$ ,  $z^R = \lambda^R(\Delta t)$ , and  $(\Delta t)$  is the time step. The discretized convection term contributes scaled eigenvalues,  $z^C$ , that are predominately imaginary while the diffusion terms have predominately real scaled eigenvalues,  $z^D$ . Reaction rate eigenvalues,  $\lambda^R$ , are mostly real and may give rise to relatively large scaled eigenvalues,  $z^R$ . Based on this knowledge, one might seek to construct a new method based on two separate methods: one optimized to smaller eigenvalues of the convection and diffusion terms and one that is capable of dealing with very large reaction-rate eigenvalues. It should be remarked that because of the high sound speeds introduced by the compressible equations,  $|z^C|$  is generally larger than  $|z^D|$ , even in the DNS of a hypersonic boundary

layer resolved down to  $y^+ = 1$ . Discretized incompressible flows, governed by index-2 differential algebraic equations, generally have  $|z^D| > |z^C|$ .

If the stability domain of the integrator contains all values of  $z^C$ ,  $z^D$ , and  $z^R$ , then stable integration can be done. For accuracy purposes, the integration must proceed no faster than the fastest relevant physical processes contained within the governing equations. A situation may arise, however, where stable integration of the discretized governing equations can only proceed at a time scale substantially faster than any physically relevant time scale of the continuum-based compressible equations. This may render a numerical method unacceptably inefficient. It may occur in regions of intense grid clustering or while using stiff chemistry, but may be caused by other issues like interface boundary conditions within a multidomain formulation. There are two possible strategies to obtaining a solution at a reasonable cost when this occurs: change the governing equations and hence their characteristic time scales or change the numerical method. We choose the latter.

As an example of the disparate time scales involved in chemically reacting flow-fields, figure A.1 shows the fastest time scale of the reaction rate as a function of time during the 0D ignition of a gas mixture. Convective and diffusive time scales for the fully spatial problem would be of order tens of nanoseconds. The utility of a partitioned or additive IMEX method would then be to suppress the reactive time scales faster than the convective and diffusive scales. It may be seen from the figure that chemical mechanisms involving larger hydrocarbons can include extremely fast times scale and hence exhibit extreme stiffness.

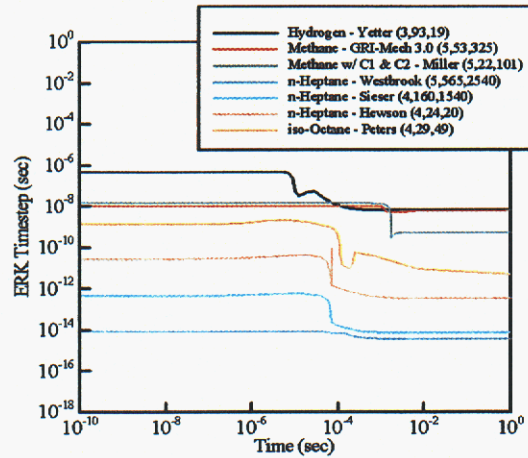


Figure A.1: Fastest time scales associated with ignition of gas mixtures.

Partitioned Runge-Kutta methods may be designed to allow for the partitioning of equations by term, gridpoint, or equation. Implicit-explicit (IMEX) partitioned methods developed to date for first order ODEs have usually considered a partitioning based on terms. They have combined explicit Runge-Kutta (ERK) schemes with variations on either the diagonally implicit Runge-Kutta (DIRK)[5, 10, 16, 18, 21, 31, 52, 62, 76–79] or Rosenbrock



family of methods.[12–14, 39, 53, 58, 62, 76–79] In this paper, methods are derived using stiffly-accurate, explicit, singly diagonally implicit Runge-Kutta (ESDIRK) schemes for their stability properties and higher stage-order. Although the word explicit appears in the name of ESDIRKs, they are implicit methods. Of the partitioned IMEX Runge-Kutta methods currently available in the literature, some exhibit lower-order coupling errors, coupling stability problems, no error control, and poor ERK or DIRK/Rosenbrock stability properties. The new schemes endeavor to address all of these shortcomings without falling prey to new ones.

A multistep[4, 17, 35] approach to IMEX schemes is also possible. Higher-order SBDF methods given by Ascher et al.,[4] based on BDF methods for the implicit portion, are of the form

$$U^{(n+1)} = -\sum_{j=0}^{k-1} \alpha_j U^{(n-j)} + (\Delta t) \beta_k \sum_{j=0}^{k-1} \left( \frac{(-1)^j k!}{(k-j-1)!(j+1)!} \right) F_{\text{explicit}}^{(n-j)} + (\Delta t) \beta_k F_{\text{implicit}}^{(n+1)},$$

where  $\alpha_j$  and  $\beta_k$  are the values for the k-step, order-k, BDF methods.[47] These methods may be quite effective for equations whose stiff terms give rise to predominately real eigenvalues. At third-order and above the BDF methods are only  $L(\alpha)$ -stable; they lack A-stability but still have a vanishing stability function for extremely stiff eigenvalues. Strongly transient events like chemical ignition may be less appropriate for SBDF methods because they lack stepsize adjustment.

This chapter contains excerpts from the journal article *Additive Runge-Kutta schemes for convection-diffusion-reaction equations*. [43] The goal of this article is to provide complete methods for solving CDR equations using additive Runge-Kutta methods. By this, it is meant that beyond having good accuracy and stability properties, there are high quality embedded methods, error controllers, dense output, stage-value predictors, and implementation guidance. This is done in a two-fold manner. First, a general overview is given of the coupling of N different Runge-Kutta methods for first-order ODEs whose right hand side is the summation of N terms: N-additive Runge-Kutta methods (ARK<sub>N</sub>). Second, matters are then specialized to the case of  $N = 2$ : additive Runge-Kutta (ARK<sub>2</sub>) methods using an implicit method that allows accurate and stable integration of the stiff terms while either integrating the nonstiff terms at the linear stability of the explicit method or integrating the entire method at some chosen error tolerance.

We do not consider the topics of storage reduction, contractivity, dispersion, and dissipation, regularity, or boundary error. The first two sections will provide an introduction to ARK<sub>N</sub> methods. Specialization of additive methods to ERK-ESDIRK combinations will be reviewed in following section. Actual third-, fourth-, and fifth-order methods along with details of testing an comparison to other methods is contained in the journal article.[43]

## A.2 N-Additive Runge-Kutta Methods

### General

Following Araújo et al.,[3]  $ARK_N$  methods are used to solve equations of the form

$$\frac{dU}{dt} = F(U) = \sum_{\nu=1}^N F^{[\nu]}(U), \quad (A2)$$

where  $F(U)$  has been additively composed of  $N$  terms. They are applied as

$$U^{(i)} = U^{(n)} + (\Delta t) \sum_{\nu=1}^N \sum_{j=1}^s a_{ij}^{[\nu]} F^{[\nu]}(U^{(j)}), \quad (A3)$$

$$U^{(n+1)} = U^{(n)} + (\Delta t) \sum_{\nu=1}^N \sum_{i=1}^s b_i^{[\nu]} F^{[\nu]}(U^{(i)}), \quad (A4)$$

$$\hat{U}^{(n+1)} = U^{(n)} + (\Delta t) \sum_{\nu=1}^N \sum_{i=1}^s \hat{b}_i^{[\nu]} F^{[\nu]}(U^{(i)}), \quad (A5)$$

where each of the  $N$  terms are integrated by its own  $s$ -stage Runge-Kutta method. Also,  $U^{(n)} \simeq U(t^{(n)})$ ,  $U^{(i)} \simeq U(t^{(n)} + c_i \Delta t)$  is the value of the  $U$ -vector on the  $i^{\text{th}}$ -stage, and  $U^{(n+1)} \simeq U(t^{(n)} + \Delta t)$ . Both  $U^{(n)}$  and  $U^{(n+1)}$  are of classical order  $q$ . The  $U$ -vector associated with the embedded scheme,  $\hat{U}^{(n+1)}$ , is of order  $p$ . Each of the respective Butcher coefficients  $a_{ij}^{[\nu]}$ ,  $b_i^{[\nu]}$ ,  $\hat{b}_i^{[\nu]}$ , and  $c_i^{[\nu]}$ ,  $\nu = 1, 2, \dots, N$  are constrained, at a minimum, by certain order of accuracy and stability considerations.

### Order Conditions

Order-of-accuracy conditions for  $ARK_N$  methods may be derived via N-trees.[3] These N-trees resemble the traditional Butcher 1-trees[8, 26, 27] but each node may be any one of  $N$  varieties or colors. Expressions for the equations of condition associated with the  $q^{\text{th}}$ -order N-trees are of the form

$$\tau_{k[n]}^{(q)} = \frac{1}{\sigma} \Phi_{k[n]}^{(q)} - \frac{\alpha}{q!} = \frac{1}{\sigma} \left( \Phi_{k[n]}^{(q)} - \frac{1}{\gamma} \right), \quad \text{where} \quad \Phi_{k[n]}^{(q)} = \sum_i^s b_i \Phi_{i,k[n]}^{(q)}, \quad (A6)$$

where  $\Phi_{k[n]}^{(q)}$  and  $\Phi_{i,k[n]}^{(q)}$  are scalar sums of Butcher coefficient products and  $1 \leq n \leq N^q$  is used to distinguish between the many possible color variations of the  $k^{\text{th}}$  1-tree of order  $q$ . Both  $\alpha$  and  $\sigma$  are color dependent; i.e., for any given 1-tree, the many corresponding N-trees may have different values of  $\alpha$  and  $\sigma$  depending on the details of the node colorings. Tree

density,  $\gamma$ , is color independent and consequently so is the product of  $\alpha$  and  $\sigma$ ,  $\sigma\alpha = q!/\gamma$ . Order conditions  $\tau_2^{(3)}$ ,  $\tau_{2,4}^{(4)}$ , and  $\tau_{6,7,9}^{(5)}$  given in the journal article,[43] never exhibit color dependence. When an equation of condition,  $\tau_{k[n]}^{(q)}$ , is made to vanish, color dependence is immaterial because  $\Phi_{k[n]}^{(q)} = 1/\gamma$ . For equations of condition that are not made to vanish, color dependence must be taken into consideration to accurately assess the leading order error terms. Order conditions for partitioned Runge-Kutta methods have also been derived by Jackiewicz and Vermiglio[37] following an approach of Albrecht.

## Coupling Conditions

Aside from satisfying the order conditions specific to each of the elemental methods of the  $\text{ARK}_N$ , one must also satisfy various coupling conditions. One may write the total number of order conditions for a general  $\text{ARK}_N$  associated with each particular root node coloring,  $\alpha_i^{[N]}$ , using the expression[24, 26, 63]

$$\sum_{i=1}^{\infty} \alpha_i^{[N]} x^{(i-1)} = \prod_{i=1}^{\infty} (1 - x^i)^{-N\alpha_i^{[N]}}. \quad (\text{A7})$$

At order  $i = \{1, 2, 3, 4, 5, 6, \dots\}$ , a general  $\text{ARK}_N$  method has a total of  $N\alpha_i^{[N]}$  order conditions, where  $\alpha_i^{[1]} = \{1, 1, 2, 4, 9, 20, \dots\}$ ,  $\alpha_i^{[2]} = \{1, 2, 7, 26, 107, 458, \dots\}$ ,  $\alpha_i^{[3]} = \{1, 3, 15, 82, 495, 3144, \dots\}$ ,  $\alpha_i^{[4]} = \{1, 4, 26, 188, 1499, 12628, \dots\}$ , and  $\alpha_i^{[5]} = \{1, 5, 40, 360, 3570, 37476, \dots\}$ . Some of these,  $N\alpha_i^{[1]}$ , are order conditions of the elemental methods which compose the  $\text{ARK}_N$ . This implies that  $N(\alpha_i^{[N]} - \alpha_i^{[1]})$  of the order conditions are composed of portions of different elemental methods. These are coupling conditions. As both order of accuracy and  $N$  increase, their numbers grow explosively. Table 1 shows their numbers for orders up to five and for each 1-tree listed in the journal article[43] with which the coupling conditions are associated and also depending on whether the simplifying assumptions  $b_i^{[\nu]} = b_i^{[\mu]}$  or  $c_i^{[\nu]} = c_i^{[\mu]}$  are imposed. To satisfy all of these order conditions, there are no more than  $N*s(s+1)$  independent Butcher coefficients.

It may also be seen from this that as long as  $b_i^{[\nu]} = b_i^{[\mu]}$  (identical root nodes) and  $c_i^{[\nu]} = c_i^{[\mu]}$  (identical canopy nodes), an arbitrary number of independent third-order methods having the same number of stages may be coupled together with no associated coupling error. Selecting  $b_i^{[\nu]} = b_i^{[\mu]}$  or  $c_i^{[\nu]} = c_i^{[\mu]}$  allows second-order error-free coupling of an arbitrary number of schemes. Choosing neither of these assumptions reduces error-free coupling, as seen from table 1, to first-order. Further, if  $c_i^{[\nu]} = c_i^{[\mu]}$  is invoked, only autonomous-problem order conditions need be considered.

## Error

Error in an elemental  $q^{\text{th}}$ -order Runge-Kutta scheme contained within an  $\text{ARK}_N$  method may be quantified in a general way by taking the  $L_2$  principal error norm,[41]  $A^{(q+1)} = \|\tau^{(q+1)}\|_2$



Eqn. of cond.	$b_i^{[\nu]} \neq b_i^{[\mu]}$ $c_i^{[\nu]} \neq c_i^{[\mu]}$	$b_i^{[\nu]} = b_i^{[\mu]}$ $c_i^{[\nu]} \neq c_i^{[\mu]}$	$b_i^{[\nu]} \neq b_i^{[\mu]}$ $c_i^{[\nu]} = c_i^{[\mu]}$	$b_i^{[\nu]} = b_i^{[\mu]}$ $c_i^{[\nu]} = c_i^{[\mu]}$
$\tau_1^{(1)}$	0	0	0	0
$\tau_1^{(2)}$	$N(N-1)$	0	0	0
$\tau_1^{(3)}$ $\tau_2^{(3)}$	$N^2(N+1)/2! - N$ $N^3 - N$	$N(N+1)/2! - N$ $N(N-1)$	0 $N(N-1)$	0 0
$q = 3$	$N(N-1)(3N+4)/2!$	$3N(N-1)/2!$	$N(N-1)$	0
$q \leq 3$	$N(N-1)(3N+6)/2!$	$3N(N-1)/2!$	$N(N-1)$	0
$\tau_1^{(4)}$ $\tau_2^{(4)}$ $\tau_3^{(4)}$ $\tau_4^{(4)}$	$N^2(N+1)(N+2)/3! - N$ $N^4 - N$ $N^3(N+1)/2! - N$ $N^4 - N$	$N(N+1)(N+2)/3! - N$ $N^3 - N$ $N^2(N+1)/2! - N$ $N^3 - N$	0 $N(N-1)$ $N(N-1)$ $N^3 - N$	0 0 0 $N(N-1)$
$q = 4$	$N(N-1)(16N^2 + 22N + 24)/3!$	$N(N-1)(16N + 22)/3!$	$N(N-1)(N+3)$	$N(N-1)$
$q \leq 4$	$N(N-1)(16N^2 + 31N + 42)/3!$	$N(N-1)(16N + 31)/3!$	$N(N-1)(N+4)$	$N(N-1)$
$\tau_1^{(5)}$ $\tau_2^{(5)}$ $\tau_3^{(5)}$ $\tau_4^{(5)}$ $\tau_5^{(5)}$ $\tau_6^{(5)}$ $\tau_7^{(5)}$ $\tau_8^{(5)}$ $\tau_9^{(5)}$	$N^2(N+1)(N+2)(N+3)/4! - N$ $N^4(N+1)/2! - N$ $N^3(N^2+1)/2! - N$ $N^4(N+1)/2! - N$ $N^3(N+1)(N+2)/3! - N$ $N^5 - N$ $N^5 - N$ $N^4(N+1)/2! - N$ $N^5 - N$	$N(N+1)(N+2)(N+3)/4! - N$ $N^3(N+1)/2! - N$ $N^2(N^2+1)/2! - N$ $N^3(N+1)/2! - N$ $N^2(N+1)(N+2)/3! - N$ $N^4 - N$ $N^4 - N$ $N^3(N+1)/2! - N$ $N^4 - N$	0 $N(N-1)$ $N^2(N+1)/2! - N$ $N(N-1)$ $N(N-1)$ $N^3 - N$ $N^3 - N$ $N^3 - N$ $N^4 - N$	0 0 $N(N-1)/2!$ 0 0 $N(N-1)$ $N(N-1)$ $N(N-1)$ $N^3 - N$
$q = 5$	$N(N-1)(125N^3 + 179N^2 + 210N + 216)/4!$	$N(N-1)(125N^2 + 179N + 210)/4!$	$N(N-1)(2N^2 + 9N + 16)/2!$	$N(N-1) \times (2N+9)/2!$
$q \leq 5$	$N(N-1)(125N^3 + 243N^2 + 334N + 384)/4!$	$N(N-1)(125N^2 + 243N + 334)/4!$	$N(N-1)(2N^2 + 11N + 24)/2!$	$N(N-1) \times (2N+11)/2!$

Table A.1: Number of  $\text{ARK}_N$  Coupling Conditions

where  $\tau_j^{(q+1)}$  are the  $\alpha_{q+1}^{[1]}$  error coefficients associated with order of accuracy  $q + 1$ . For embedded schemes where  $p = q - 1$ , additional definitions are useful such as

$$\hat{\tau}_k^{(p)} = \frac{1}{\sigma} \sum_i^s \hat{b}_i \Phi_{i,k}^{(p)} - \frac{\alpha}{p!}, \quad \hat{A}^{(p+1)} = \|\hat{\tau}^{(p+1)}\|_2, \quad D = \text{Max}\{|a_{ij}^{[\nu]}|, |b_i^{[\nu]}|, |\hat{b}_i^{[\nu]}|, |c_i^{[\nu]}|\}, \quad (\text{A8})$$

$$B^{(p+2)} = \frac{\hat{A}^{(p+2)}}{\hat{A}^{(p+1)}}, \quad C^{(p+2)} = \frac{\|\hat{\tau}^{(p+2)} - \tau^{(p+2)}\|_2}{\hat{A}^{(p+1)}}, \quad E^{(p+2)} = \frac{A^{(p+2)}}{\hat{A}^{(p+1)}}, \quad (\text{A9})$$

where the superscript circumflex denotes the values with respect to the embedded method. In the case of ARK<sub>N</sub> methods, there is generally no reason to assume any particular order condition is more important than another, therefore we generalize the traditional expression for  $A^{(q+1)}$  to

$$A^{(q+1)} = \|\tau^{(q+1)}\|_2 = \sqrt{\sum_{k=1}^{\alpha_{q+1}^{[1]}} \sum_{n=1}^{n_{N,k,(q+1)}} \left(\tau_{k[n]}^{(q+1)}\right)^2}, \quad (\text{A10})$$

where we have used  $n_{N,k,(q+1)}$  to denote the total number of ARK<sub>N</sub> order conditions arising from all variations of the  $k^{\text{th}}$  1-tree at order  $(q+1)$ . In certain special cases one may be able to rule out extended subquadrature, or nonlinear order conditions based on the structure of the ODE at hand.[70] To evaluate the value of the error estimate, one may evaluate the quality parameters  $B^{(p+2)}$ ,  $C^{(p+2)}$ , and  $E^{(p+2)}$  using each  $\tau_k^{(q+1)}$  from each elemental method or using every  $\tau_{k[n]}^{(q+1)}$ . All embedded schemes considered here are applied in local extrapolation mode. For a given order of accuracy, one strives to minimize  $A^{(q+1)}$ . Based on experience with  $q = p + 1$  ERK pairs,  $B^{(p+2)}$ ,  $C^{(p+2)}$ , and  $E^{(p+2)}$  are ideally kept of order unity while  $D$  is usually kept less than 20.

## Simplifying Assumptions

Butcher[8, 27] row and column simplifying assumptions will be helpful in designing methods because they can reduce and simplify the order conditions. By surveying table 1, one quickly surmises that higher-order methods effectively require the use of the assumptions  $b_i^{[\nu]} = b_i^{[\mu]} = b_i$  and  $c_i^{[\nu]} = c_i^{[\mu]} = c_i$ . Also, without identical root or canopy nodes, application of Butcher simplifying assumptions would become very awkward; therefore, simplifying assumptions are considered in the form

$$C^{[\nu]}(\eta, i) : \quad \sum_{j=1}^s a_{ij}^{[\nu]} c_j^{q-1} = \frac{c_i^q}{q}, \quad i = 1, \dots, s, \quad q = 1, \dots, \eta, \quad (\text{A11})$$

$$D^{[\nu]}(\zeta, j) : \quad \sum_{i=1}^s b_i c_i^{q-1} a_{ij}^{[\nu]} = \frac{b_j}{q} (1 - c_j^q), \quad j = 1, \dots, s, \quad q = 1, \dots, \zeta. \quad (\text{A12})$$

The notation  $C^{[\nu]}(\eta, i \neq 2)$  should be interpreted as  $C^{[\nu]}(\eta, i)$  for all  $i$  except 2.

## Stability

The linear stability function for N-additive methods is considered using the equation

$$F(U) = \sum_{\nu=1}^N \lambda^{[\nu]} U, \quad (\text{A13})$$

from which it is determined that the stability function is[10]

$$R(z^{[1]}, z^{[2]}, \dots, z^{[N]}) = \frac{P(z^{[1]}, z^{[2]}, \dots, z^{[N]})}{Q(z^{[1]}, z^{[2]}, \dots, z^{[N]})}, \quad (\text{A14})$$

$$= \frac{\text{Det} \left[ \mathbf{I} - \sum_{\nu=1}^N (z^{[\nu]} \mathbf{A}^{[\nu]}) + \sum_{\nu=1}^N (z^{[\nu]} \mathbf{e} \otimes \mathbf{b}^{[\nu]T}) \right]}{\text{Det} \left[ \mathbf{I} - \sum_{\nu=1}^N (z^{[\nu]} \mathbf{A}^{[\nu]}) \right]}, \quad (\text{A15})$$

where  $\mathbf{A}^{[\nu]} = a_{ij}^{[\nu]}$ ,  $\mathbf{b}^{[\nu]} = b_i^{[\nu]}$ ,  $\mathbf{I} = \delta_{ij}$ ,  $z^{[\nu]} = \lambda^{[\nu]} \Delta t$ , and  $\mathbf{e} = \{1, 1, \dots, 1\}$ . Stability for the embedded method is evaluated using the expression above with  $\hat{\mathbf{b}}^{[\nu]}$  replacing  $\mathbf{b}^{[\nu]}$ . We remark that this form of  $F(U)$  is a more severe simplification than the traditional one ( $N = 1$ ) because one cannot, in general, simultaneously diagonalize all  $N$  jacobians.

## Conservation

Conservation of certain integrals or invariants may also be of interest in additive Runge-Kutta methods.[3, 28] Similar to the algebraic stability matrix, one may define

$$M_{ij}^{[\nu, \mu]} = b_i^{[\nu]} a_{ij}^{[\mu]} + b_j^{[\mu]} a_{ji}^{[\nu]} - b_i^{[\nu]} b_j^{[\mu]}. \quad (\text{A16})$$

ARK<sub>N</sub> methods conserve linear first integrals, in general, only if  $b_i^{[\nu]} - b_i^{[\mu]} = 0$ , and conserve certain quadratic first integrals, in general, only if  $b_i^{[\nu]} - b_i^{[\mu]} = 0$  and  $M_{ij}^{[\nu, \mu]} = 0$ , where  $i, j = 1, 2, \dots, s$ ,  $\nu, \mu = 1, 2, \dots, N, \nu \neq \mu$ . Conservation of cubic invariants with Runge-Kutta methods is not possible.[9, 28, 36]

## Dense Output

The purpose of dense output[26, 51] has traditionally been to allow high-order interpolation of the integration variables at any point,  $t^{(n)} + \theta \Delta t$ , inside the current integration step where  $0 \leq \theta \leq 1$ . It may also be used, albeit more cautiously, for extrapolating integration variable values to enable better stage value guesses when one or more of the elemental methods is implicit.[50, 56] For an ARK<sub>N</sub> method, it is accomplished as

$$U(t^{(n)} + \theta \Delta t) = U^{(n)} + (\Delta t) \sum_{\nu=1}^N \sum_{i=1}^s b_i^{*[\nu]}(\theta) F^{[\nu]}(U^{(i)}), \quad (\text{A17})$$

$$b_i^{*[\nu]}(\theta) = \sum_{j=1}^{p^*} b_{ij}^{*[\nu]} \theta^j, \quad b_i^{*[\nu]}(\theta = 1) = b_i^{[\nu]}, \quad (\text{A18})$$



where  $p^*$  is the lowest order of the interpolant on the interval  $0 \leq \theta \leq 1$ . By construction,  $b_i^{*[\nu]}(\theta = 0) = 0$ . Order conditions, at order  $m$ , for the dense output method are given by

$$\tau_{k[n]}^{*(m)} = \frac{1}{\sigma} \sum_i^s b_i^* \Phi_{i,k[n]}^{(m)} - \frac{\alpha \theta^m}{m!}. \quad (\text{A19})$$

Setting  $m = q$  and  $\theta = 1$ , we retrieve (A6). As with the main and embedded formulae, one may write terms like  $A^{*(p^*+1)} = A^{*(p^*+1)}(\theta)$  to access the accuracy of the dense output method. When used as an extrapolation device ( $\theta > 1$ ), the stability function  $R^*(z^{[1]}, z^{[2]}, \dots, z^{[N]}, \theta)$  must be considered.[6, 20] It is derived by replacing  $\mathbf{b}^{[\nu]}$  in the traditional stability function with  $\mathbf{b}^{*[\nu]}(\theta)$ . Throughout this paper, we will assume  $b_{ij}^{*[\nu]} = b_{ij}^{*[\mu]} = b_{ij}^*$ .

### A.3 Implicit-Explicit ARK<sub>2</sub> Methods

Given that the CDR equations have three terms, a natural question is whether an IMEX ARK<sub>2</sub> or an ARK<sub>3</sub> (one implicit and two explicit) method is more appropriate. Stability of the method should include L-stability of the overall method as well as good stability from explicit portions for vanishing values of the stiff scaled eigenvalue. L-stability imposes three conditions for  $N=2$  and five for  $N=3$ . The total number of free tall trees associated with the explicit methods is  $(s - q)$  for  $N=2$  and  $(s - q)^2$  for  $N=3$ . In terms of accuracy, the difference in accumulated number of coupling conditions at orders  $\{1, 2, 3, 4, 5, 6\}$  is  $\{0, 0, 0, 4, 36, 231\}$ . Also, as  $N$  increases, the total number of principal error terms increases yielding relatively higher values of  $A^{(q+1)}$ . As we ultimately seek methods of orders four or five, it would seem prudent to limit further discussion to ARK<sub>2</sub> schemes. The equations are therefore cast in the form

$$\frac{dU}{dt} = F_{\text{ns}} + F_{\text{s}}, \quad (\text{A20})$$

where  $F_{\text{ns}}$  represents the non-stiff terms and  $F_{\text{s}}$  represents the stiff terms, and we then consider implicit-explicit ARK<sub>2</sub> methods. ERK methods are used to integrate the non-stiff terms. Stiff terms are treated with ESDIRK methods.[2, 32, 44, 45] Coefficients for the ERK and ESDIRK methods will be distinguished by  $a_{ij}^{[E]}$  and  $a_{ij}^{[I]}$ , respectively. ESDIRKs offer the advantages of allowing L-stability, stiff accuracy, and a stage-order of two. They differ from the more traditional SDIRK[1, 27] methods by having an explicit first stage. A consequence of allowing a stage-order of two is that algebraic stability becomes impossible.[66] As we will always invoke  $b_i^{[E]} = b_i^{[I]} = b_i$ ,  $\hat{b}_i^{[E]} = \hat{b}_i^{[I]} = b_i$  and  $c_i^{[E]} = c_i^{[I]} = c_i$  in this paper, their superscripts are henceforth superfluous. In general, an ERK method has  $s(s+1)/2$  degrees of freedom (DOF) available to satisfy all order and any other conditions, where  $s$  is the number of stages. An ESDIRK has  $(s^2+s+2)/2$  available DOF. Combining the two into an ARK<sub>2</sub> scheme, if each  $b_i$  and each  $c_i$  are made equal,  $(2s-1)$  DOF are lost, leaving  $(s^2 - s + 2)$  DOF. A further assumption of  $a_{sj}^{[I]} = b_j$ , the stiffly-accurate assumption, reduces this to  $(s^2 - 2s + 2)$  and facilitates L-stability as well as forces the stiff part of  $U^{(n+1)}$  to be computed implicitly. It is particularly useful in cases of singular-perturbation type problems and, when combined with L-stability, generally tolerates stiffness better than non-stiffly accurate L-stable methods. Incorporating stiff accuracy and a stage-order of 2 into all of the ESDIRKs, the IMEX

ARK<sub>2</sub> methods then take the form

0	0	0	0	0	...	0	0	0	0	...	0
2γ	2γ	0	0	0	...	0	2γ	γ	γ	0	0
c <sub>3</sub>	a <sub>31</sub> <sup>[E]</sup>	a <sub>32</sub> <sup>[E]</sup>	0	0	...	0	c <sub>3</sub>	a <sub>31</sub> <sup>[I]</sup>	a <sub>32</sub> <sup>[I]</sup>	γ	0
⋮	⋮	⋮	⋮	⋮	⋮	0	⋮	⋮	⋮	⋮	0
c <sub>s-1</sub>	a <sub>s-1,1</sub> <sup>[E]</sup>	a <sub>s-1,2</sub> <sup>[E]</sup>	a <sub>s-1,3</sub> <sup>[E]</sup>	⋮	0	0	c <sub>s-1</sub>	a <sub>s-1,1</sub> <sup>[I]</sup>	a <sub>s-1,2</sub> <sup>[I]</sup>	a <sub>s-1,3</sub> <sup>[I]</sup>	⋮
1	a <sub>s,1</sub> <sup>[E]</sup>	a <sub>s,2</sub> <sup>[E]</sup>	a <sub>s,3</sub> <sup>[E]</sup>	...	a <sub>s,s-1</sub> <sup>[E]</sup>	0	1	b <sub>1</sub>	b <sub>2</sub>	b <sub>3</sub>	...
	b <sub>1</sub>	b <sub>2</sub>	b <sub>3</sub>	...	b <sub>s-1</sub>	γ		b <sub>1</sub>	b <sub>2</sub>	b <sub>3</sub>	...
	b <sub>1</sub>	b <sub>2</sub>	b <sub>3</sub>	...	b <sub>s-1</sub>	b <sub>s</sub>		b <sub>1</sub>	b <sub>2</sub>	b <sub>3</sub>	...

where  $\gamma = a_{ii}^{[I]}$ ,  $i = 2, 3, \dots, s$  and should not be confused with the density of an N-tree,  $\gamma$ , discussed in section 2.1.1.

To identify the schemes derived in this paper, a nomenclature similar to that originally devised by Dormand and Prince is followed.[41] Schemes will be named ARKq(p)sS[ $q_{so}$ ]X, where  $q$  is the order of the main method,  $p$  is the order of the embedded method,  $s$  is the number of stages,  $S$  is some stability characterization of the method,  $q_{so}$  is the stage order of the implicit method, and  $X$  is used for any other important characteristic of the method. For  $S$ , we use  $L$  to denote an  $L$ -stable ARK<sub>2</sub>. Distinguishing between  $L$ -stable methods that are or are not stiffly accurate is important; hence, we use  $X$  as  $SA$  to denote stiffly accurate.

## Design

## Accuracy

Both ERK and ESDIRK methods are subject to the  $\{1, 1, 2, 4, 9, 20\}$  order conditions for orders  $\{1, 2, 3, 4, 5, 6\}$ . These order conditions are listed up to fifth-order for 1-trees in the journal article[43] and to fifth-order for general 2-trees in the extended paper.[42] With the assumptions  $b_i^{[I]} = b_i^{[E]} = b_i$  and  $c_i^{[I]} = c_i^{[E]} = c_i$ , there are  $\{0, 0, 0, 2, 13, 63\}$  coupling conditions at the same orders (see section II.15[26]). At fourth- and fifth-order, these coupling order conditions are shown as bicolored trees in figure A.2.

Further reduction of the number and complexity of order conditions is possible by using Butcher simplifying assumptions. Unfortunately, they may conflict with one another. For instance, applying assumptions  $D^{[E]}(1, j)$  and  $D^{[I]}(1, j)$  gives rise to two inconsistent equations at  $j = s$ ,

$$b_s \gamma = b_s(1 - c_s), \quad 0 = b_s(1 - c_s). \quad (A21)$$

The first implies  $c_s = 1 - \gamma$  while the second implies either  $b_s = 0$  or  $c_s = 1$ . Hence, no value of  $c_s$  can satisfy both equations and consequently the column simplifying assumption can only be applied to one of the methods. In conjunction with the stiffly accurate assumption which forces  $c_s = 1$ , it may only be used on the ERK. We avoid the option of setting both  $a_{11}^{[I]}$  and  $a_{ss}^{[I]}$  to zero because of the complication that will arise in enforcing  $L$ -stability and the possibility of explicitly computed stage values. Additional interscheme conflict occurs upon imposition of

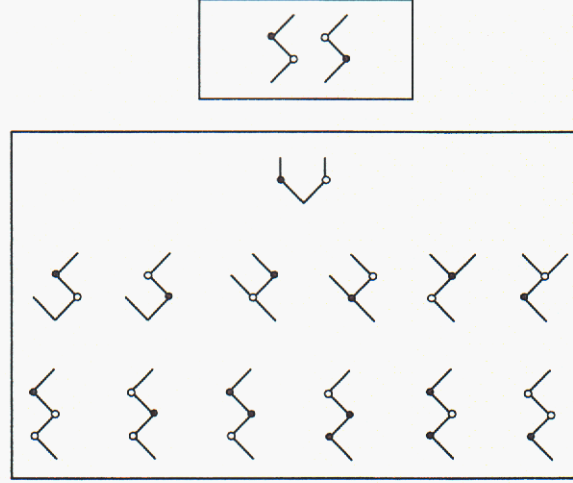


Figure A.2: Fourth- and fifth-order bicolored coupling conditions for  $b_i^{[I]} = b_i^{[E]}$  and  $c_i^{[I]} = c_i^{[E]}$ .

$C^{[E]}(3, i \neq 2)$  and  $C^{[I]}(3, i)$ . A stage order of two on the stiffly accurate ESDIRK is imposed by enforcing  $C^{[I]}(2, i) = 0$  for  $i = 2, \dots, (s-1)$ . A stage order of three is impossible because of the second stage where  $\sum_{j=1}^s a_{2j}^{[I]} c_j^2 - c_2^3/3 = 4\gamma^3/3 \neq 0$ . Reducing the truncation error of the second stage is clearly facilitated by smaller values of  $\gamma$ .

## Stability

Linear stability for an ERK-ESDIRK  $\text{ARK}_2$  method with  $b_i^{[I]} = b_i^{[E]} = \mathbf{b}$  is analyzed using the stability function[10]

$$R(z^{[E]}, z^{[I]}) = \frac{\text{Det} [\mathbf{I} - z^{[E]} \mathbf{A}^{[E]} - z^{[I]} \mathbf{A}^{[I]} + (z^{[E]} + z^{[I]}) \mathbf{e} \otimes \mathbf{b}^T]}{\text{Det} [\mathbf{I} - z^{[I]} \mathbf{A}^{[I]}]} = \frac{P(z^{[E]}, z^{[I]})}{Q(z^{[I]})} \quad (\text{A22})$$

where

$$P(z^{[E]}, z^{[I]}) = \sum_{i=0}^s \left\{ \sum_{j=0}^{s-i} p_{ij} (z^{[E]})^j \right\} (z^{[I]})^i, \quad (\text{A23})$$

$$Q(z^{[I]}) = 1 + \sum_{i=1}^{s-1} q_i (z^{[I]})^i = (1 - \gamma z^{[I]})^{s-1}. \quad (\text{A24})$$

To recover the ERK stability function only,  $p_{ij} = p_{0j}$  or  $z^{[I]} = 0$  and  $q_i = 0$ . The ESDIRK is retrieved with  $p_{ij} = p_{i0}$  or  $z^{[E]} = 0$ . Both the  $\text{ARK}_2$  and ESDIRK methods share the same  $q_i$  coefficients. In all cases  $p_{00} = 1$ . A total of  $(s-1)(s-2)/2$  of the  $p_{ij}$  coefficients are coupling stability terms where  $i, j \neq 0$ . For an ESDIRK to be L-stable, it is required that  $\gamma > 0$  so that the stability function remains analytic in the complex left-half-plane, the method must be I-stable, and



$p_{s,0} = p_{s-1,0} = 0$  so that the stability function vanishes as  $z^{[I]}$  tends toward infinity. I-stability of the ESDIRK method is determined using the E-polynomial[27] given by

$$E(y) = Q(+iy)Q(-iy) - P(0, +iy)P(0, -iy) = \sum_{j=0}^s E_{2j} y^{2j}, \quad (\text{A25})$$

where  $i = \sqrt{-1}$ . Imaginary axis (I-)stability requires that  $E(y) \geq 0$  for all real values of  $y$ . It is sufficient but not necessary to have all  $E_{2j} \geq 0$ . An L-stable ESDIRK will have  $E_{2s} = 0$ . An order  $q$  ESDIRK will have  $E_{2j} = 0$  for  $2j \leq q$ .

Above and beyond L-stability of the ESDIRK method, it may be useful to control the damping of the large scaled eigenvalues,  $z^{[I]}$ , at intermediate stages.[71] The internal stability function at the  $n^{\text{th}}$ -stage may be constructed for DIRK-type methods by using portions of the  $a_{ij}^{[I]}$  matrix. Denoting  $a_{ij}^{[I]}, i, j = 1, 2, \dots, n$  as  $\mathcal{A}$  and  $a_{nj}^{[I]}, j = 1, 2, \dots, n$  as  $\mathcal{B}_j$ , the internal stability function is given by

$$R_{\text{int}}^{(n)}(z^{[I]}) = \frac{\text{Det} [\mathcal{I} - z^{[I]} \mathcal{A}^{[I]} + z^{[I]} \mathcal{E} \otimes \mathcal{B}^T]}{\text{Det} [\mathcal{I} - z^{[I]} \mathcal{A}^{[I]}]} = \frac{P_{\text{int}}^{(n)}(z^{[I]})}{Q_{\text{int}}^{(n)}(z^{[I]})}, \quad (\text{A26})$$

where  $\mathcal{I}$  is the  $(n \times n)$  identity matrix, and  $\mathcal{E}$  is the one-vector of length  $n$ . Our concern will be the value of  $R_{\text{int}}^{(n)}(-\infty)$ .  $P_{\text{int}}^{(n)}$  is, in general, a polynomial of degree  $n - 1$  in  $z^{[I]}$  because  $\mathcal{A}_{nj} = \mathcal{B}_j$  while  $Q_{\text{int}}^{(n)}$  is, in general, of degree  $n$ . Consequently, SDIRKs have  $R_{\text{int}}^{(n)}(-\infty) = 0$ . ESDIRKs, with  $Q_{\text{int}}^{(n)}$  reduced to degree  $n - 1$  because  $a_{11}^{[I]} = 0$ , do not generally satisfy  $R_{\text{int}}^{(n)}(-\infty) = 0$ .

In terms of step-wise stability, choosing the stiffly accurate assumption forces  $p_{s,0} = 0$ . Placing  $a_{i1}^{[I]} = 0$  forces  $p_{s-1,0} = 0$  but sacrifices  $(s - 1)$  DOF and the possibility of higher stage-order. A consequence of setting  $a_{11}^{[I]} = 0$ , what effectively distinguishes the ESDIRK from the SDIRK, is that it forces  $q_s = 0$ . Achieving an L-acceptable stability function for the ARK<sub>2</sub>,

$$R(z^{[E]}, z^{[I]}) = \frac{1 + \dots + \{p_{s-1,1} z^{[E]} + p_{s-1,0}\} (z^{[I]})^{s-1} + p_{s,0} (z^{[I]})^s}{1 + \dots + (-\gamma)^{s-1} (z^{[I]})^{s-1}}, \quad (\text{A27})$$

and not just the ESDIRK, is now more complicated because of  $p_{s-1,1}$ . In both the ESDIRK and IMEX ARK<sub>2</sub> cases,  $p_{s,0}$  and  $p_{s-1,0}$  must vanish for L-stability, but the IMEX scheme must also satisfy  $p_{s-1,1} = 0$ . Several of the methods given by Ascher et al.[5] and Griepentrog[21] do not account for this and consequently have  $R(z^{[E]}, -\infty)$  depending linearly on  $z^{[E]}$ . Similar comments apply to  $\hat{p}_{ij}$  and  $p_{ij}^* = \sum_{k=1}^{p^*} p_{ijk}^* \theta^k$ , the coefficients of the P-polynomials for the embedded and dense-output formulae. A benefit of a zero-column in  $a_{ij}^{[I]}$ ,  $j = 1$ , for an additive method is that on problems such as Kreiss's problem,[15, 27] which may act like an index-2 differential algebraic equation, the initial value of the algebraic variable is not propagated along with the solution.[38] Ascher et al.[5] and Calvo et al.[10] both choose  $a_{sj}^{[I]} = b_j$  as well as zero-padded SDIRKs ( $a_{i1}^{[I]} = 0$ ) and consequently their methods perform relatively well on Kreiss's problem.

## Conservation

As the scheme weights,  $b_i$ , for the current ERK and ESDIRK methods are the same, linear first integrals will be conserved. Certain quadratic first integrals will, however, only be conserved if linear first integrals are conserved and  $M_{ij}^{[E,I]} = 0$  vanishes. We will adopt the point of view that although none of the methods will make this vanish, minimizing the magnitude of this matrix,

$$\|M_{ij}^{[E,I]}\| = \sqrt{\sum_{i,j=1}^s M_{ij}^{[E,I]} M_{ji}^{[E,I]}}, \quad (\text{A28})$$

should enhance conservation characteristics.

## A.4 Implementation

### Stage Values

Using the definitions  $F_{\text{ns}}^{(j)} \simeq F_{\text{ns}}(U^{(j)}, t^{(n)} + c_j \Delta t)$  and  $F_s^{(j)} \simeq F_s(U^{(j)}, t^{(n)} + c_j \Delta t)$ , one must solve

$$U^{(i)} = U^{(n)} + X^{(i)} + (\Delta t) \gamma F_s^{(i)}, \quad i \geq 2, \quad X^{(i)} = (\Delta t) \sum_{j=1}^{i-1} (a_{ij}^{[E]} F_{\text{ns}}^{(j)} + a_{ij}^{[I]} F_s^{(j)}) \quad (\text{A29})$$

where  $X^{(i)}$  is explicitly computed from existing data. Combining this with an appropriate starting guess, a modified[23, 33, 59, 61] Newton iteration provides  $U^{(i)}$  and  $F_s^{(i)}$ . In cases where direct methods are appropriate, this is accomplished by solving

$$\left( I - (\Delta t) \gamma \frac{\partial F_s}{\partial U} \Big|_k \right) (U^{(i)} - U_k^{(i)}) = - (U_k^{(i)} - U^{(n)}) + X^{(i)} + (\Delta t) \gamma F_s(U_k^{(i)}), \quad (\text{A30})$$

where the subscript  $k$  denotes the value on the  $k^{\text{th}}$  iteration,  $M = [I - \gamma(\Delta t)(\partial F_s / \partial U)|_k]$  is the iteration matrix, and  $d_k^{(i)} = (U^{(i)} - U_k^{(i)})$  is the displacement. On the  $k^{\text{th}}$  iteration one has

$$M d_k^{(i)} = r_k^{(i)}, \quad U_{k+1}^{(i)} = U_k^{(i)} + M^{-1} r_k^{(i)}, \quad (\text{A31})$$

where  $r_k^{(i)}$  is the residual. The iteration is terminated when either  $d_k^{(i)}$  (displacement test) or  $r_k^{(i)}$  (residual test) are sufficiently small,[33, 67]

$$\tau_{\text{residual}} = c\epsilon \leq r_k^{(i)}, \quad \text{or}, \quad \tau_{\text{displacement}} = c\epsilon \leq d_k^{(i)}, \quad c \approx 0.005,$$

where  $\epsilon$  is the integration error tolerance and  $c$  is the tolerance ratio.  $F_{\text{ns}}^{(i)}$  may then be computed using  $U^{(i)}$ . Inexact[30, 40, 54] Newton methods may be more appropriate for larger systems of coupled equations.

## Stage-Value Predictors

Stage-value iteration convergence rates may be substantially improved and convergence failures may be minimized by choosing a good starting guess. The most primitive approach to obtaining a guess for the integration variables at the next stage is to use the most recent stage values; the trivial guess. An oftentimes better way to obtain stage-value starting guesses is by using a dense output formula.[27, 32, 50, 56] Second and later steps may use the function evaluations from the previous step to extrapolate into the current step. Stage-value guesses for the  $i^{\text{th}}$  stage of the step  $n + 1$  are obtained using function evaluations from step  $n$  as

$$U^{(i)}(t^n + \theta_i \Delta t) = U^{(n)} + (\Delta t) \sum_{j=1}^s b_j^*(\theta_i) \left( F_{\text{ns}}^{(j)} + F_s^{(j)} \right), \theta_i = 1 + r c_i, r = \frac{(\Delta t)^{(n+1)}}{(\Delta t)^{(n)}} \quad (\text{A32})$$

Shortcomings of this approach include order-of-accuracy reduction when an interpolation formula is used in extrapolation mode and the introduction of instabilities into the extrapolated guess. As is sometimes done with the implicit error control estimate when substantial stiffness is present, one may wish to smooth the predicted stage value by multiplying it by the iteration matrix.[32, 60] More sophisticated predictors have been derived relevant to DIRK methods.[20, 29, 46, 57] We do not consider these, in part, because computer memory management may become a problem. To conserve memory usage during extrapolation, all  $s$ -stages may be estimated at the beginning of the step and function values might then be overwritten by stage-value guesses, one equation at a time. For large  $r$ , the trivial guess may be more prudent.

## Error and Step-Size Control

Step-size control is a means by which accuracy, iteration, and to a lesser extent stability are controlled. The choice of the  $(\Delta t)$  may be chosen from many criteria, among those are the  $(\Delta t)$  from the accuracy based step controller, the  $(\Delta t)_{\text{inviscid}}$  and  $(\Delta t)_{\text{viscous}}$  associated with the inviscid and viscous stability limits of the ERK, and the  $(\Delta t)_{\text{iter}}$  associated with iteration convergence.[23] If error control reliability is sufficient, CFL numbers may be removed as their function would be superfluous. For  $q = p + 1$  pairs, one could consider timestep control of the IMEX schemes using I-, PI-, and PC-controllers[27] or a PID-controller[22, 64, 65]

$$(\Delta t)_{\text{PID}}^{(n+1)} = \kappa (\Delta t)^{(n)} \left\{ \frac{\epsilon}{\|\delta^{(n+1)}\|_{\infty}} \right\}^{\alpha} \left\{ \frac{\|\delta^{(n)}\|_{\infty}}{\epsilon} \right\}^{\beta} \left\{ \frac{\epsilon}{\|\delta^{(n-1)}\|_{\infty}} \right\}^{\gamma}, \quad (\text{A33})$$

with error estimate  $\delta^{(n+1)} = U^{(n+1)} - \hat{U}^{(n+1)}$ ,  $\kappa \approx 0.9$ ,  $\epsilon$  is a user specified tolerance, and  $p$  is the order-of-accuracy of the embedded method. The I-, PI-, and PID-controllers are appropriate to explicit methods. Implicit methods use either I- or PC-controllers. A PID-controller is considered because many stability optimized ERK methods are SC-unstable with a PI-controller for eigenvalues on the real axis.[41] Its characteristic roots are those of the equation  $\zeta^3 + (p\alpha - 1)\zeta^2 - p\beta\zeta + p\gamma = 0$ . Individual controller gains are obtained via  $k_I = p(\alpha - \beta + \gamma)$ ,  $k_P = p(\beta - 2\gamma)$ , and  $k_D = p\gamma$ .



One may wish to keep controller gains fixed, independent of stepsize changes. This may be done by preselecting gains, then using  $\omega^{(n)} = \frac{(\Delta t)^{(n)}}{(\Delta t)^{(n-1)}}$  and

$$p\alpha = \left[ k_I + k_P + \left( \frac{2\omega^{(n)}}{1 + \omega^{(n)}} \right) k_D \right], \quad p\beta = \left[ k_P + 2\omega^{(n)} k_D \right], \quad p\gamma = \left( \frac{2\omega^{2(n)}}{1 + \omega^{(n)}} \right) k_D. \quad (\text{A34})$$

In the present context, we have selected  $k_I = 0.25$ ,  $k_P = 0.14$ ,  $k_D = 0.10$ , or  $\alpha = 0.49/p$ ,  $\beta = 0.34/p$ ,  $\gamma = 0.10/p$  when  $\omega^{(n)} = 1$ , giving characteristic roots of  $\{-0.518, 0.247, 0.781\}$ . The controller is SC-stable at all stability boundary points of the ERK in the complex left-half-plane for each of the three proposed methods. Inclusion of second-derivative gain, a PIDD<sup>2</sup>-controller, was not found to enhance control. This strategy may not behave well if substantial order-reduction occurs due to extreme stiffness because, at a minimum,  $p$  no longer reflects the actual order of the embedded method. Stability based time step limits involving the inviscid and viscous CFL numbers,  $(\lambda, \lambda_v)$ , are given by  $(\Delta t)_{\text{inviscid}} \approx \lambda(\Delta x)/(u + a)$  and  $(\Delta t)_{\text{viscous}} \approx \lambda_v(\Delta x)^2/\nu$  where  $a$  is the local speed of sound,  $u$  is the magnitude of local fluid convection speed, and  $\nu$  is an appropriate diffusivity of either mass, momentum, or energy.[41] For implicit-explicit methods, we select

$$(\Delta t)^{(n+1)} = \text{Min} \left\{ (\Delta t)_{\text{error}}^{(n+1)}, (\Delta t)_{\text{inviscid}}, (\Delta t)_{\text{viscous}}, (\Delta t)_{\text{iteration}} \right\}. \quad (\text{A35})$$

It remains to be determined which controller(s) are best suited to IMEX methods.

## A.5 Conclusions

Additive Runge-Kutta (ARK) methods are investigated for application to the spatially discretized one-dimensional convection-diffusion-reaction (CDR) equations.[43] First, accuracy, stability, conservation, and dense-output are considered for the general case when  $N$  different Runge-Kutta methods are grouped into a single composite method. Comparing the  $N = 3$  and  $N = 2$  cases for CDR applications,  $N = 2$  methods are chosen. Then, implicit-explicit,  $N = 2$ , additive Runge-Kutta (ARK<sub>2</sub>) methods from third- to fifth-order are presented. Each allows for integration of stiff reactive terms by an L-stable, stiffly-accurate ESDIRK method while the nonstiff convection and diffusion terms are integrated with a traditional ERK method. Coupling error terms are minimized by selecting identical abscissae and scheme weights for each method and are of equal order to those of the elemental methods. Both ARK<sub>2</sub> and ESDIRK methods have vanishing stability functions for very large values of the stiff scaled eigenvalue,  $z^{[I]} \rightarrow -\infty$ , and retain high stability efficiency in the absence of stiffness,  $z^{[I]} \rightarrow 0$ . Extrapolation-type stage-value predictors are provided based on dense-output formulae. Dense output stability functions have minimized values for  $\theta > 1$  and  $z^{[I]} \rightarrow -\infty$ . Optimized methods minimize both leading order ARK<sub>2</sub> error terms and Butcher coefficient magnitudes as well as maximize conservation properties. Numerical tests of the new schemes on a CDR problem show negligible stiffness leakage and near classical order convergence rates. Third- and fourth-order SBDF methods are slightly more efficient than the IMEX ARK<sub>2</sub> schemes but do not include error estimation and stepsize control. Tests on three simple singular perturbation problems reveal similar and predictable order reduction for the Runge-Kutta methods but no order reduction for the SBDF methods. Order reduction of ARK<sub>2</sub> schemes is worst at intermediate stiffness levels. Estimated convergence rates for differential and algebraic variables generally

coincide with that predicted by theory. A reinspection of differential and algebraic variables on the CDR problem shows similar behavior. Error control is best managed with a PID-controller, indicating that ERK stability is the overriding issue in controlling time steps and error. Dense output is useful both in interpolation and extrapolation. While results for the fifth-order method are disappointing, both the new third- and fourth-order methods are at least as efficient as existing ARK<sub>2</sub> methods.

## References

1. R. Alexander, Diagonally implicit Runge-Kutta methods for stiff O.D.E.s, *SIAM J. Num. Anal.*, 14(6) (1977) 1006-1021.
2. R. Alexander and J.J. Coyle, Runge-Kutta methods and differential-algebraic systems, *SIAM J. Num. Anal.*, 27(3) (1990) 736-752.
3. A.L. Araújo, A. Murua, and J.M. Sanz-Serna, Symplectic methods based on decompositions, *SIAM J. Num. Anal.*, 34(5) (1997) 1926-1947.
4. U.M. Ascher, S.J. Ruuth, and B.T.R. Wetton, Implicit-explicit methods for time-dependent partial differential equations, *SIAM J. Num. Anal.* 32(3) (1995) 797-823.
5. U.M. Ascher, S.J. Ruuth, and R.J. Spiteri, Implicit-explicit Runge-Kutta methods for time-dependent partial differential equations, *Appl. Num. Math.*, 25(2-3) (1997) 151-167.
6. A. Bellen and M. Zennaro, Stability properties of interpolants for Runge-Kutta methods, *SIAM J. Num. Anal.*, 25(2) (1988) 411-432.
7. T. Belytschko, A review of recent developments in time integration, In: A.K. Noor and J.T. Oden, eds., *State-of-the-art surveys on computational mechanics*, American Society of Mechanical Engineers, New York (1989) pp. 185-199.
8. J.C. Butcher, *The Numerical Analysis of Ordinary Differential Equations: Runge-Kutta and General Linear Methods*, John Wiley & Sons, Chichester, 1987.
9. M.P. Calvo, A. Iserles, and A. Zanna, Numerical solution of isospectral flows, *Math. Comp.*, 66(220), (1997) 1461-1486.
10. M.P. Calvo, J. de Frutos, and J. Novo, Linearly implicit Runge-Kutta methods for advection-reaction-diffusion equations, *Appl. Num. Math.*, 37(4) (2001) 535-549.
11. J.H. Chen and H.G. Im, Correlation of the flame speed with stretch in turbulent premixed Methane/Air flames, in: *Twenty-Seventh Symposium (International) on Combustion*, The Combustion Institute, Pittsburg, PA. (1998) pp. 819-826.
12. L.R. Chen and D.G. Liu, Combined RK-Rosenbrock methods and their stability, *Math. Numer. Sin.*, 22(3) (2000) 319-332. [In Chinese, ISSN 0254-7791]

13. L.R. Chen and D.G. Liu, Parallel compound methods for solving partitioned stiff systems, *J. Comp. Math.*, 19(6) (2001) 639-650.
14. G.J. Cooper and A.M.S. Sayfy, Additive Runge-Kutta methods for stiff ordinary differential equations, *Math. Comp.*, 40(161), (1983) 207-218.
15. K. Dekker and J.G. Verwer, *Stability of Runge-Kutta Methods for Stiff Nonlinear Differential Equations*, North-Holland, Amsterdam, Netherlands, 1984.
16. T.A. Driscoll, A composite Runge-Kutta method for the spectral solution of semilinear PDE, *Unpublished* (2001). See (<http://www.math.udel.edu/~driscoll/research/>)
17. J. Frank, W. Hundsdorfer, and J.G. Verwer, Stability of implicit-explicit linear multstep methods, *Appl. Num. Math.*, 25(2-3) (1997) 193-205.
18. P. Fritzen and J. Wittekindt, Numerical solution of viscoplastic constitutive equations with internal state variables, Part I: Algorithms and implementation, *Math. Meth. Appl. Sci.*, 20(16) (1997) 1411-1425.
19. A. Gerische and Verwer, J.G., Operator splitting and approximate factorization for taxis-diffusion-reaction models, CWI Report MAS-R0026, Centrum voor Wiskunde en Informatica, Amsterdam, 2000.
20. S. González-Pinto, J.I. Montijano and S. Pérez-Rodríguez, On starting algorithms for implicit RK methods, *BIT*, 40(4) (2000) 685-714
21. E. Griepentrog, Gemischte Runge-Kutta-Verfahren für steife system [Mixed Runge-Kutta methods for stiff systems], In: Seminarberichte Nr. 11, 19-29, Sektion Mathematik, Humboldt Universitat. Berlin, 1978. [In German]
22. K. Gustafsson, M. Lundh, and G. Söderlind, A PI-stepsize control for the numerical solution of ordinary differential equations, *BIT*, 28(2) (1988) 270-287.
23. K. Gustafsson and G. Söderlind, Control theoretic techniques for the iterative solution of non-linear equation in ODE solvers, *SIAM J. Sci. Comp.*, 18(1) (1997) 23-40.
24. E. Hairer, Order conditions for numerical methods for partitioned ordinary differential equations, *Numer. Math.*, 36(4) (1981) 431-445.
25. E. Hairer, Ch. Lubich, and M. Roche, Error of Runge-Kutta methods for stiff problems studied via differential algebraic equations, *BIT*, 28(3) (1988) 678-700.
26. E. Hairer, S.P. Nørsett, and G. Wanner, *Solving Ordinary Differential Equations I, Nonstiff Problems*, 2ed., Springer-Verlag, Berlin, 1993.
27. E. Hairer and G. Wanner, *Solving Ordinary Differential Equations II, Stiff and Differential-Algebraic Problems*, 2ed., Springer-Verlag, Berlin, 1996.
28. E. Hairer, *Numerical Geometric Integration*, Unpublished Notes, Section de Mathématiques, Université de Genève, Genève, 1999.



29. I. Higuera and T. Roldán, Starting algorithms for some DIRK methods, *Numer. Alg.*, 23(4) (2000) 357-369.
30. A.C. Hindmarsh and S.P. Nørsett, KRYSI, An ODE Solver combining a semi-implicit Runge-Kutta method with a preconditioned Krylov method, UCID-21422, Lawrence Livermore National Laboratories, Livermore, 1988.
31. E. Hofer, A partially implicit method for large stiff systems of ODEs with only few equations introducing small time-constants, *SIAM J. Num. Anal.*, 13(5) (1976) 645-663.
32. M.E. Hosea and L.F. Shampine, Analysis and implementation of TR-BDF2, *Appl. Num. Math.*, 20(1) (1996) 21-37.
33. N. Houbak, S.P. Norsett, and P.G. Thomsen, Displacement or residual test in the application of implicit methods for stiff problems, *IMA J. Num. Anal.*, 5(3) (1985) 297-305.
34. W.H. Hundsdorfer, Numerical solution of advection-diffusion-reaction equations, CWI Report NM-N9603, Centrum voor Wiskunde en Informatica, Amsterdam, 1996.
35. K.J. in 't Hout, On the contractivity of implicit-explicit linear multistep methods. Accepted *Appl. Numer. Math.* (2001).
36. A. Iserles and A. Zanna, Preserving algebraic invariants with Runge-Kutta methods, *J. Comp. & Appl. Math.*, 125(1) (2000), 69-81.
37. Z. Jackiewicz and R. Vermiglio, Order conditions for partitioned Runge-Kutta methods, *Appl. Math.*, 45(4) (2000) 301-316.
38. L. Jay, Convergence of a class of Runge-Kutta methods for differential-algebraic systems of index-2, *BIT*, 33(1) (1993) 137-150.
39. J.C. Jorge, J.I. Montijano, and L. Randez, [A pair 4(3) of additive Runge-Kutta methods for the integration of stiff differential equations], In: *Actas del XI C.E.D.Y.A. (Congreso de Ecuaciones Diferenciales y Aplicaciones) : I Congreso de Matematica Aplicada*, 1989, pp. 295-299. [In Spanish]
40. C.T. Kelley, *Iterative Methods for Linear and Nonlinear Equations*, Society for Industrial and Applied Mathematics, Philadelphia, PA., 1995.
41. C.A. Kennedy, M.H. Carpenter, and R.H. Lewis, Low-storage, explicit Runge-Kutta schemes for the compressible Navier-Stokes equations, *Appl. Num. Math.*, 35(3) (2000) 177-219.
42. C.A. Kennedy and M.H. Carpenter, Additive Runge-Kutta schemes for convection-diffusion-reaction equations, NASA Technical Memorandum, NASA/TM-2001-211038, Langley Research Center, Hampton, VA (2001).
43. C.A. Kennedy and M.H. Carpenter, Additive Runge-Kutta schemes for convection-diffusion-reaction equations, *Appl. Num. Math.*, 44(1-2) (2003) 139-181.

44. A. Kværnø, More, and to be hoped for, better DIRK methods for the solution of stiff ODEs, Technical Report, Mathematical Sciences Division, Norwegian Institute of Technology, Trondheim, Norway, 1992.
45. A. Kværnø, S.P. Nørsett, and B. Owren, Runge-Kutta research in Trondheim, *Appl. Num. Math.*, 22(1-3) (1996) 263-277.
46. M.P. Laburta, Starting algorithms for IRK methods, *J. Comp. & Appl. Math.*, 83(2) (1997) 269-288.
47. J.D. Lambert, *Numerical Methods for Ordinary Differential Systems. The Initial Value Problem*, John Wiley & Sons, Chichester, 1991.
48. D. Lanser and J.G. Verwer, Analysis of operator splitting for advection-diffusion-reaction problems from air pollution modelling, *J. Comp. & Appl. Math.*, 111(1) (1999) 201-216.
49. A. Murua, Formal series and numerical integrators, Part I: Systems of ODEs and symplectic integrators, *Appl. Num. Math.*, 29(2) (1999) 221-251.
50. S.P. Nørsett and P.G. Thomsen, Local error control in SDIRK-methods, *BIT*, 26(1) (1986) 100-113.
51. B. Owren and M. Zennaro, Order barriers for continuous explicit Runge-Kutta methods, *Math. Comp.*, 56(194) (1991) 645-661.
52. L. Pareschi and G. Russo, Implicit-explicit Runge-Kutta schemes for stiff systems of differential equations, In: L. Brugnano and D. Trigiante, eds, *Recent Trends in Numerical Analysis*, Vol. 3, Nova Science Pub., Huntington, NY (2000) pp. 269-289.
53. P. Rentrop, Partitioned Runge-Kutta methods with stiffness detection and stepsize control, *Numer. Math.*, 47(4) (1985) 545-564.
54. W.C. Rheinboldt, *Methods for Solving Nonlinear Equations*, 2nd Ed., Society for Industrial and Applied Mathematics, Philadelphia, PA., 1998.
55. S.J. Ruuth, Implicit-explicit methods for reaction-diffusion problems in pattern formation, *J. Math. Biology*, 34(2) (1995) 148-176.
56. J. Sand, RK-predictors: Extrapolation methods for implicit Runge-Kutta formulae, DIKU Report Nr. 88/18, Datalogisk Institut, Københavns Universitet, Copenhagen, 1988.
57. J. Sand, Methods for starting iteration schemes for implicit Runge-Kutta formulae, In: J.R. Cash and I. Gladwell, eds., *Computational Ordinary Differential Equations*, Clarendon Press, New York, 1992, pp. 115-126.
58. A.M.S. Sayfy,  $A[\alpha]$ -stable additive Runge-Kutta methods for stiff I.V.P.'s, *J. Info. & Opt. Sci.*, 16(3) (1995) 471-480.
59. L.F. Shampine, Implementation of implicit formulas for the solution of ODEs, *SIAM J. Sci. Comp.*, 1(1) (1980) 103-118.

60. L.F. Shampine and L.S. Baca, Error estimators for stiff differential equations, *J. Comp. & Appl. Math.*, 11(2) (1984) 197-207.
61. L.F. Shampine, *Numerical Solution of Ordinary Differential Equations*, Chapman & Hall, New York, 1994.
62. J.W. Shen and X. Zhong, Semi-implicit Runge-Kutta schemes for non-autonomous differential equations in reactive flow computations, AIAA Paper 96-1969, AIAA, Fluid Dynamics Conference, 27th, New Orleans, LA, June 17-20, 1996.
63. N.J.A. Sloane and S. Plouffe, *The Encyclopedia of Integer Sequences*, Academic Press, San Diego, 1995. Also, see <http://www.research.att.com/~njas/sequences/index.html>
64. G. Söderlind, The automatic control of numerical integration, *CWI Quarterly*, 11, 1, (1998) 55-74.
65. G. Söderlind, Digital filters in adaptive time-stepping Part I: PID control, *Submitted for Publication* (2001).
66. M.N. Spijker, Feasibility and contractivity in implicit Runge-Kutta methods, *J. Comp. & Appl. Math.*, 12/13, (1985) 563-578.
67. M.N. Spijker, On the error committed by stopping the Newton iteration in implicit Runge-Kutta methods, *Annals Num. Math.*, 1, (1994) 199-212.
68. Ch. Tsitouras and S.N. Papakostas, Cheap error estimation for Runge-Kutta methods, *SIAM J. Sci. Comp.*, 20(6) (1999) 2067-2088.
69. V. Van, A hybrid Implicit-explicit FDTD scheme for nonlinear optical waveguide modeling, *IEEE. Trans. Microwave Theory & Tech.*, 47(5) (1999) 540-545.
70. J.H. Verner, High-order explicit Runge-Kutta pairs with low stage order, *Appl. Num. Math.*, 22(1-3) (1996) 345-357.
71. J.G. Verwer, An analysis of Rosenbrock methods for nonlinear stiff initial value problems, *SIAM. J. Num. Anal.*, 19(1) (1981) 155-170.
72. R. Weiner, M. Arnold, P. Rentrop, and K. Strehmel, Partitioning strategies in Runge-Kutta type methods, *IMA J. Num. Anal.*, 13(2) (1993) 303-319.
73. S. Wolfram, *The Mathematica Book*, Fourth Edition, Cambridge University Press, Cambridge (1999).
74. Wolfram Research, *Mathematica 4.0 Standard Add-On Packages*, Cambridge University Press, Cambridge (1999).
75. A. Xiao and S. Li, Error of partitioned Runge-Kutta methods for multiple stiff singular perturbation problems, *Computing*, 64(2) (2000) 183-189.



76. J.J.-I. Yoh and X. Zhong, Semi-implicit Runge-Kutta schemes for stiff multi-dimensional reacting flows, AIAA Paper 97-0803, AIAA, Aerospace Sciences Meeting & Exhibit, 35th, Reno, NV, Jan. 6-9, 1997.
77. J.J.-I. Yoh and X. Zhong, Low-storage semi-implicit Runge-Kutta methods for reactive flow computations, AIAA Paper 98-0130, AIAA, Aerospace Sciences Meeting & Exhibit, 36th, Reno, NV, Jan. 12-15, 1998.
78. X. Zhong, New high-order semi-implicit Runge-Kutta schemes for computing transient nonequilibrium hypersonic flows, AIAA Paper 95-2007, AIAA, Thermophysics Conference, 30th, San Diego, CA, June 19-22, 1995.
79. X. Zhong, Additive semi-implicit Runge-Kutta methods for computing high-speed nonequilibrium reactive flows, J. Comp. Phys., 128(1) (1996) 19-31.

## **Distribution**

### **Internal Distribution:**

10	MS9051	Jacqueline Chen, 8351
1	MS9051	Alan Kerstein, 8351
1	MS9051	Joseph Oefelein, 8351
1	MS1135	John Hewson, 9132
1	MS9053	John Dec, 8362
1	MS9053	Magnus Sjoberg, 8362
1	MS9053	Jay Keller, 8362
1	MS9054	Robert Carling, 8350
1	MS9054	William McLean, 8300
1	MS9053	Charles Mueller, 8362
3	MS9018	Central Technical Files, 8945-1
1	MS0899	Technical Library, 9616
1	MS9021	Classification Office, 8511 Technical Library, MS 0899, 9616 DOE/OSTI via URL
1	MS 0188	D. Chavez, LDRD Office, 1030